



저작자표시-비영리-변경금지 2.0 대한민국

이용자는 아래의 조건을 따르는 경우에 한하여 자유롭게

- 이 저작물을 복제, 배포, 전송, 전시, 공연 및 방송할 수 있습니다.

다음과 같은 조건을 따라야 합니다:



저작자표시. 귀하는 원저작자를 표시하여야 합니다.



비영리. 귀하는 이 저작물을 영리 목적으로 이용할 수 없습니다.



변경금지. 귀하는 이 저작물을 개작, 변형 또는 가공할 수 없습니다.

- 귀하는, 이 저작물의 재이용이나 배포의 경우, 이 저작물에 적용된 이용허락조건을 명확하게 나타내어야 합니다.
- 저작권자로부터 별도의 허가를 받으면 이러한 조건들은 적용되지 않습니다.

저작권법에 따른 이용자의 권리는 위의 내용에 의하여 영향을 받지 않습니다.

이것은 [이용허락규약\(Legal Code\)](#)을 이해하기 쉽게 요약한 것입니다.

[Disclaimer](#)

Doctoral Thesis

Monitoring and Characterization of Arctic Sea Ice
using Radar Altimetry

Sanggyun Lee

Department of Urban and Environmental Engineering
(Environmental Science and Engineering)

Graduate School of UNIST

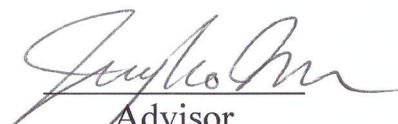
2018

Monitoring and Characterization of Arctic Sea Ice using Radar Altimetry

A dissertation
submitted to the Graduate School of UNIST
in partial fulfillment of the
requirements for the degree of
Doctor of Philosophy

Sanggyun Lee

21. 12. 2017
Approved by



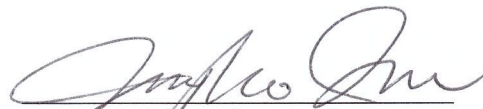
Advisor
Jungho Im

Monitoring and Characterization of Arctic Sea Ice using Radar Altimetry

Sanggyun Lee

This certifies that the dissertation of Sanggyun Lee is
approved.

21. 12. 2017



Advisor: Jungho Im

Thesis Committee Member: Myong-In Lee

Thesis Committee Member: Kyung Hwa Cho

Thesis Committee Member: Hyun-choel Kim

Thesis Committee Member: Hyangsun Han

Abstract

Launching CryoSat-2, which is a current radar altimeter mission for the monitoring of polar region enables to produce monthly based sea ice thickness since April 2010. The Sea ice thickness cannot be measured directly by satellite. Sea ice freeboard that is an elevation above sea level can be converted in to sea ice thickness by assuming hydrostatic equilibrium. Sea ice leads (e.g., linear cracks in sea ices) are regarded as sea surface tie points for the estimation of sea ice freeboard. Identifying the sea ice leads is one of the core factors to retrieve sea ice thickness. The surface elevation is estimated by the use of Threshold First maxima Retracker Algorithm (TFMRA) for a 40% threshold using CryoSat-2 L1b data and the leads are detected by machine learning approaches such as decision trees and random forest. The machine learning produces better accuracy for the sea ice thickness than previous simple thresholding approach, validating EM-31, airborne sea ice thickness observations. A novel method to overcome previous threshold based lead detection methods for identifying leads is developed, which is waveform mixture algorithm that linear mixture analysis is applied in terms of waveforms. The waveform mixture algorithm can distinguish leads without beam behavior parameters and backscatter σ_0 but just use waveforms, which is less affected by updating baseline for CryoSat-2. In addition to the development of the algorithms, a scientific research is carried out. Causes for sea ice anomaly phenomenon in November 2016 is investigated. Eventually, sea ice the volume derived by thickness is used for the analysis of sea ice extent minimum in November 2016 and suggest a new insight of sea ice minimum phenomenon. Unlike sea ice extent, the sea ice volume is not a minimum in November 2016. However, since the base period for sea ice volume is short, it is hard to mention climatology of sea ice volume.

CONTENTS

Abstract.....	i
Contents	iii
List of Figures.....	vi
List of Tables	ix
List of Arcronyms.....	x

Chapter 1	
1. Introduction	1
1.1 The role of sea ice in the Earth climate system	1
1.2 Arctic amplification	3
1.3 Remote sensing of sea ice	4
1.4 Sea ice altimetry	6
1.4.1 Basic principle of radar altimetry	7
1.4.2 Concept of SAR altimetry and CryoSat-2	7
1.5 Overview of papers.....	11
1.6 Research questions and hypotheses.....	12
Chapter 2	
2. Arctic sea ice thickness estimation from CryoSat-2 satellite data using machine learning-based lead detection.....	14
2.1 Introduction.....	14
2.2 Data.....	15
2.2.1 MODIS.....	15
2.2.2 Sea ice type.....	16
2.2.3 Airborne Electromagnetics data	16
2.3 Sea ice thickness estimation and machine learning algorithms for lead detection.....	16
2.3.1. Sea ice thickness estimation	16
2.3.2. Machine learning algorithms for lead detection.....	21
2.4 Results and Discussion.....	25
2.4.1 Characteristics of five parameters based on CryoSat-2 waveform	25
2.4.2 Comparison of lead detection performance.....	26
2.4.3 Spatial distribution of Arctic sea ice freeboard and thickness.....	35
2.5 Conclusions.....	39
Chapter 3	
3. Arctic lead detection using a waveform mixture algorithm from CryoSat-2 data.....	41
3.1 Introduction.....	41
3.2 Data.....	43

3.2.1 Sea ice edge data	43
3.2.2 Monthly lead fraction maps.....	43
3.3 Methods.....	44
3.3.1 Waveform mixture analysis.....	44
3.3.2 Endmember selection.....	45
3.3.3 Calculation of sensitivity in a 10x10 km grid.....	47
3.4 Results	49
3.4.1 Performance of lead classification	49
3.4.2 Spatiotemporal distribution of lead fraction maps	52
3.4.3 Grid sensitive analysis in 10x10 km	56
3.5 Discussion	58
3.5.1 Comparison of lead classification methods	58
3.5.2 Comparison to other lead fraction maps	58
3.5.3 Lead dynamics	61
3.5.4 Novelty and limitations.....	63
3.6 Conclusions.....	64
Chapter 4	
4. Anomalous slow sea ice recovery in fall and winter 2016 by extreme warming event in mid-latitudes.....	65
4.1 Introduction.....	65
4.2 Data and Methods.....	66
4.2.1 Sea ice concentration and thickness	66
4.2.2 MERRA-2 reanalysis and SST data.....	66
4.3 Results	67
4.3.1 Anomalous warming event in mid-latitudes and Arctic	67
4.3.2 Sea ice minimum extent in November 2016.....	69
4.4 Discussion	73
4.4.1 Comparison of previous anomaly phenomena	73
4.4.2 Sea ice thickness in November 2016	73
4.5 Conclusions.....	76
Chapter 5	
5. Conclusions.....	77

Chapter 6

6. Outlook and Future works.....78

Chapter 7

7. References.....79

List of Figures

FIGURE 1. 1 GLOBAL THERMOHALINE CIRCULATION MAP. IMAGE FROM NASA EARTH OBSERVATORY.....	2
FIGURE 1. 2 ANNUAL SURFACE AIR TEMPERATURE ANOMALY FOR THE PERIOD 1960-2009 (50 YEARS). THE LINEAR TREND SHOWS THAT AVERAGE TEMPERATURES IN NORTHERN HIGH LATITUDES IS HIGHER THAN OTHER LATITUDES (SERREZE AND BARRY, 2011).....	3
FIGURE 1. 3 TYPICAL NORMALIZED ECHO POWER WAVEFORM OF CRYOSAT-2 SAR MODE DATA OVER (A) SEA ICE, (B) OCEAN, AND (C) LEADS.	8
FIGURE 2. 1 SCHEMATIC DIAGRAM OF THE FREEBOARD AND THICKNESS PROCESSING FROM CRYOSAT-2.....	17
FIGURE 2. 2 THE SEA ICE FREEBOARD PROCESSING PROCEDURE USING CRYOSAT-2 DATA.	18
FIGURE 2. 3 A TYPICAL WAVEFORM OF SEA ICE FROM CRYOSAT-2 DATA. THE DOTTED LINE DENOTES THE THRESHOLD LEVEL ESTIMATED BY THE THRESHOLD RETRACKING METHOD (A = 40 %). THE OPEN SQUARE INDICATES THE RANGE POINT OF THE FIRST MAXIMUM POWER PEAK DETERMINED BY THE PEAK DETECTION ALGORITHM. THE OPEN CIRCLE INDICATES THE RANGE POINT OF THE LEADING EDGE.....	20
FIGURE 2. 4 OVERLAY OF A CRYOSAT-2 PATH ON A NEAR-REAL-TIME MODIS IMAGE. THE CRYOSAT-2 PATH (RED LINE) WAS GEOLOCATED ON THE MODIS IMAGE IN THE NORTH OF SVALBARD ON 6 APRIL 2011. THE TIME DIFFERENCE BETWEEN THE TWO WAS 30 MINUTES. BASED ON VISUAL INTERPRETATION, FIVE PARAMETERS WERE EXTRACTED FOR TARGET FEATURES (I.E., LEADS, SEA ICE, AND OCEAN).	22
FIGURE 2. 5 BOX PLOTS OF 5 PARAMETERS (I.E., SSD, STACK SKEWNESS, STACK KURTOSIS, PP, AND BACKSCATTER SIGMA-0) OVER LEADS, SEA ICE, AND OCEAN USING THE MARCH AND APRIL SAMPLES FROM 2011 TO 2014. THE VERTICAL HEIGHT OF THE BOXES INDICATES THE INTERQUARTILE RANGE OF THE SAMPLES. WHILE A PARALLEL LINE INSIDE THE BOXES MEANS A MEDIAN VALUE OF THE SAMPLES FOR EACH PARAMETER, THE DOTS REPRESENT THE OUTLIERS.	26
FIGURE 2. 6 EXAMPLES OF LEAD DETECTION RESULTS AROUND EAST FRANZ JOSEF LAND ON 11 APRIL 2014 (A-D) AND BEAUFORT SEA ON 11 APRIL 2011(E-H) USING FOUR METHODS: (A/E) ROSE (2013), (B/F) LAXON ET AL. (2013), (C/G) SEE5.0 IN THE PRESENT STUDY, AND (D/H) RANDOM FOREST IN THE PRESENT STUDY. RED AND BLUE DOTS REPRESENT LEADS AND SEA ICE, RESPECTIVELY	30
FIGURE 2. 7 SSHA AND FREEBOARD EXTRACTED BY EACH METHOD USING CRYOSAT-2 DATA FROM UTC 03:47 TO 03:57, 09 APRIL 2012 BASED ON IC: (A) – (D) ARE THE INTERPOLATED AND SMOOTHED SSHA; (E) – (H) ARE THE SMOOTHED FREEBOARD.....	34
FIGURE 2. 8 ARCTIC SEA ICE FREEBOARD FROM CRYOSAT-2 FOR MARCH AND APRIL BETWEEN 2011 AND 2014 BASED ON IC SCHEME. NON-SEA ICE AREAS WERE MASKED OUT USING THE EUMETSAT OSI SAF SEA ICE TYPE DATA.	36
FIGURE 2. 9 ARCTIC SEA ICE THICKNESS FROM CRYOSAT-2 FOR MARCH AND APRIL BETWEEN 2011 AND 2014 BASED ON THE IC SCHEME. NON-SEA ICE AREAS WERE MASKED OUT USING THE	

EUMETSAT OSI SAF SEA ICE TYPE DATA.....	37
FIGURE 2. 10 SCATTERPLOTS BETWEEN THE CRYOSAT-2-DERIVED SEA ICE THICKNESS AND THE AVERAGED AEM-BIRD ICE THICKNESS FOR VALIDATION.	38
FIGURE 3. 1 LEAD AND ICE ABUNDANCE DERIVED BY WAVEFORM MIXTURE ANALYSIS ON 10 OCT. 2015. (A) LEAD ABUNDANCE, (B) ICE ABUNDANCE. THE COLOUR BAR EXPRESSES ABUNDANCES FROM 0 TO 1.....	46
FIGURE 3. 2 REPRESENTATIVE WAVEFORMS OF (A) LEADS AND (B) SEA ICE OVER THE ARCTIC OCEAN SELECTED BY N-FINDR ALGORITHM DURING JANUARY TO MAY AND OCTOBER TO DECEMBER BETWEEN 2011 AND 2016. REFER TO THE METHODS SECTION FOR N-FINDR ALGORITHM.	49
FIGURE 3. 3 VISUAL COMPARISON OF LEAD CLASSIFICATIONS: (A) – (D) LEAD CLASSIFICATIONS BASED ON ROSE (2013), (E) – (H) LEAD CLASSIFICATIONS BASED ON LAXON ET AL. (2013), (I) – (L) LEAD CLASSIFICATIONS BASED ON DECISION TREES FROM LEE ET AL. (2016), AND (M) – (P) LEAD CLASSIFICATIONS BASED ON THE PROPOSED WAVEFORM MIXTURE ANALYSIS. THE MODIS DATA WERE COLLECTED IN MARCH (A, E, I, AND M), APRIL (B, F, J, AND N), MAY (C, G, K, AND O), AND OCTOBER (D, H, L, AND P).....	51
FIGURE 3. 4 ACCURACY ASSESSMENT RESULTS FOR LEAD DETECTION BY METHOD—THREE EXISTING METHODS AND THE PROPOSED WAVEFORM MIXTURE ALGORITHM (WMA).	52
FIGURE 3. 5 MONTHLY LEAD FRACTION MAPS BASED ON WAVEFORM MIXTURE ANALYSIS IN JANUARY TO MAY, OCTOBER TO DECEMBER BETWEEN 2011 AND 2013. THE RANGE OF THE COLOUR BAR WAS SET FROM 0 TO 0.5 TO EMPHASIZE LOWER VALUES.	54
FIGURE 3. 6 MONTHLY LEAD FRACTION MAPS BASED ON WAVEFORM MIXTURE ANALYSIS IN JANUARY TO MAY, OCTOBER TO DECEMBER BETWEEN 2014 AND 2016. THE RANGE OF THE COLOUR BAR WAS SET FROM 0 TO 0.5 TO EMPHASIZE LOWER VALUES.	55
FIGURE 3. 7 (A-D) THE NUMBER OF LEAD OBSERVATIONS, (E-H) THE NUMBER OF ICE OBSERVATIONS, (I-L) THE STANDARD DEVIATION OF THE RESULTS BASED ON THE SENSITIVITY ANALYSIS OF LEAD FRACTION FROM JANUARY TO APRIL 2011.	57
FIGURE 3. 8 COMPARISON TO OTHER LEAD FRACTION MAPS IN JANUARY TO MARCH 2011. (A-C) MONTHLY MEAN THIN ICE CONCENTRATION MAPS USING AMSR-E FROM RÖHRS AND KALESCHKE (2011). (D-F) MONTHLY MEAN LEAD FRACTION MAPS USING MODIS FROM WILLMES AND HEINEMANN (2015). (G-I) MONTHLY LEAD FRACTION MAPS USING CRYOSAT-2 FROM WERNECKE AND KALESCHKE (2015). (J-L) MONTHLY LEAD FRACTION MAPS BASED ON WAVEFORM MIXTURE ANALYSIS USING CRYOSAT-2 IN THIS STUDY.	60
FIGURE 3. 9 AVERAGED SEASONAL LEAD FRACTION IN SPRING (MAM), FALL (ON), AND WINTER (DJF) BETWEEN 2011 AND 2016. THE LEAD FRACTION FROM JUNE TO SEPTEMBER WAS NOT AVAILABLE BECAUSE LEADS WERE HARD TO DISTINGUISH FROM MELT PONDS USING CRYOSAT-2 IN THE SUMMER SEASON.	62
FIGURE 4. 1 2-M AIR TEMPERATURE ANOMALY FROM 1980 TO 2016 IN AUGUST TO NOVEMBER IN DIFFERENT AREA: (A) MID-LATITUDES, (B) ARCTIC REGION. (C) SEA ICE EXTENT ANOMALY IN NOVEMBER FROM 1979 TO 2016.....	68

FIGURE 4. 2 (A-D) SEA ICE CONCENTRATION ANOMALY IN AUGUST TO NOVEMBER FROM 2007 TO 2016. (E-H) SEA ICE CONCENTRATION IN AUGUST TO NOVEMBER 2016..... 70

FIGURE 4. 3 (A-D) SPATIAL DISTRIBUTION OF 2-M AIR TEMPERATURE, SEA LEVEL PRESSURE AND 10-M WIND ANOMALY IN AUGUST TO NOVEMBER FROM 1982 TO 2016..... 71

FIGURE 4. 4 SPATIAL DISTRIBUTION OF SST ANOMALY (A) AUGUST, (B) SEPTEMBER, (C) OCTOBER, AND (D) NOVEMBER 2016..... 72

FIGURE 4. 5 SST ANOMALY IN DIFFERENT SECTOR IN AUGUST TO NOVEMBER 1982 – 2016. 72

FIGURE 4. 6 (A) SEA ICE CONCENTRATION ANOMALY IN NOVEMBER 2016 FROM 2007 AND 2016. (B) SEA ICE THICKNESS DERIVED BY CRYOSAT-2 ANOMALY IN NOVEMBER FROM 2011 – 2016. (C) SEA ICE THICKNESS IN NOVEMBER 2016 DERIVED BY CRYOSAT-2. (D) SEA ICE DRIFT IN NOVEMBER 2016. (E) SEA ICE EMISSIVITY IN NOVEMBER 2016. 74

FIGURE 4. 7 SEA ICE EXTENT AND VOLUME IN NOVEMBER FROM 2011 TO 2016..... 75

List of Tables

TABLE 1. 1 THE SPECIFICATIONS OF CRYOSAT-2 (SIRAL).....	9
TABLE 1. 2 THE EQUATIONS TO RETRIEVE SSD, STACK SKEWNESS AND KURTOSIS, AND PP.....	10
TABLE 2. 1 REFERENCE DATA USED IN THE MACHINE LEARNING MODELS BY SCHEME AND TARGET FEATURE.....	23
TABLE 2. 2 ACCURACY ASSESSMENT RESULTS OF SEE5.0 AND RANDOM FOREST BY SCHEME THROUGH 10-FOLD CROSS VALIDATION. THE OVERALL ACCURACY IN PERCENTAGE AVERAGED FOR 10 FOLDS IS PROVIDED.	27
TABLE 2. 3 RELATIVE VARIABLE IMPORTANCE (I.E., CONTRIBUTION) TO LEAD DETECTION USING SEE5.0 AND RANDOM FOREST BY IC.....	28
TABLE 2. 4 AN EXAMPLE OF THRESHOLD-BASED RULES PRODUCED BY SEE5.0 USING IC TO CLASSIFY LEADS, SEA ICE, AND OCEAN.	28
TABLE 2. 5 THE ERROR MATRIX BASED ON THE SEE5.0-BASED LEAD DETECTION RESULTS FOR IC.	31
TABLE 2. 6 THE ERROR MATRIX BASED ON THE RANDOM FOREST-BASED LEAD DETECTION RESULTS FOR IC.	31
TABLE 2. 7 THE ERROR MATRIX BASED ON THE LEAD DETECTION RESULTS BY THE APPROACH OF ROSE (2013).....	32
TABLE 2. 8 THE ERROR MATRIX BASED ON THE LEAD DETECTION RESULTS BY THE APPROACH OF LAXON ET AL. (2013).	32
TABLE 3. 1 ERROR MATRIX FOR CALCULATION OF USER’S, PRODUCER’S AND OVERALL ACCURACY IN TERMS OF LEAD AND ICE CLASSIFICATION.	47

List of Acronym

AO	Arctic Oscillation
AMSR	Advanced Microwave Scanning Radiometer
ASCAT	Advanced Scatterometer
ASIRAS	Air-borne Synthetic Aperture and Interferometric Radar Altimeter System
AVHRR	Advanced Very High Resolution Radiometer
CART	Classification And Regression Trees
DMSP	Defense Meteorological Satellite Program
DT	Decision Tree
DTU10	Technical University of Denmark 10
ERS	European Remote Sensing Satellite
ESA	European Space Agency
EUMETSAT	European Organization for the Exploitation of Meteorological Satellites
FYI	First-Year Ice
GR	Gradient Ratio
ICESat	Ice, Cloud, and land Elevation Satellite
IST	Ice Surface Temperature
LRM	Low Resolution Mode
LSSH	Local Sea Surface Height
MERRA	Modern-Era Retrospective Analysis for Research Applications version 2
MODIS	MODerate Imaging Spectroradiometer
MYI	Multi-Year Ice
NAO	North Atlantic Oscillation

NOAA	National Oceanic and Atmospheric Administration
OSI SAF	Ocean & Sea Ice Satellite Application Facility
PP	Pulse Peakiness
PR	Polarization Ratio
SAR	Synthetic Aperture Radar
SIN	SAR interferometry
SIRAL	Synthetic Aperture Interferometric Radar Altimeter
SSD	Stack Standard Deviation
SSH	Sea Surface Height
SSHA	Sea Surface Height Anomaly
SSMIS	Special Sensor Microwave Imager/Sounder
SST	Sea Surface Temperature
TFMRA	Threshold First maxima Retracker Algorithm
TIR	Thermal infrared

Monitoring and Characterization of Arctic Sea Ice using Radar Altimetry

Chapter 1

1. Introduction

1.1 The role of sea ice in the Earth climate system

Arctic sea ice is significant component in the Earth climate system. While sea ice occupies a small part of the Earth, sea ice greatly influences on the Earth climate. Since sea ice is sensitive to climate forcing, it is considered as a major indicator of climate change (Doscher et al., 2014). Sea ice plays a significant role in controlling thermal feedback process because of high reflectivity for solar radiation. The albedo of ice and snow is about 0.7 to 0.9, which is much larger than the albedo of ocean (< 0.1). The sea ice prevents the Earth from warming by the solar radiation. As the Arctic sea ice melts, the Arctic Ocean absorbs more sunlight. The warmed water melts sea ice again. It is called as ice-albedo feedback. This process known as ice albedo accelerates decline of sea ice (Curry et al., 1995; Perovich et al., 2002; Flanner et al., 2011). Taylor et al. (2013) suggested that ice albedo feedback is most contributing to the Arctic amplification. The ice albedo feedback also influences on the non-linear behavior of climate change (Winton, 2013). Eventually, recent study revealed that ice albedo feedback shifted seasonal ice zone model results and remote sensing data (Kashiwase et al., 2017). Sea ice extent and thickness will gradually decrease and ice albedo feedback will be expected to have a bigger effect on Arctic amplification and climate change.

Arctic Ocean is closely associated with ocean circulation, developing cold and salty water mass. Sea ices in the Arctic Ocean is repetitively freezing and thawing. Brines in the sea water are rejected to the underlying water by freezing sea ice (Schumacher et al., 1983). Sea ices also are melting by releasing freshwater during summer season. The water in the Arctic becomes denser and colder and leads deep water formation. This process begins to initiate thermohaline circulation, which is the global scale pattern of sea water movement driven by vertical density gradient (Fig. 1.1) (Aagaard and Carmack, 1989; Barry et al., 1993; Mauritzen and Hakkinen, 1997). Since the saltier water under the forming sea ice that deep water, the saltier water sinks at the formation of ice, triggering global circulation of sea water (Shokr and Sinha, 2015). The change in the freezing and melting sea ice clearly influence on thermohaline circulation. Forming less sea ice might induces slow thermohaline circulation, not making enough denser water. The

reduction of sea ice in the Arctic brings the change in the structure of thermohaline in the Arctic Ocean, which impacts on convection in the North Atlantic Ocean (McPhee et al., 2009).

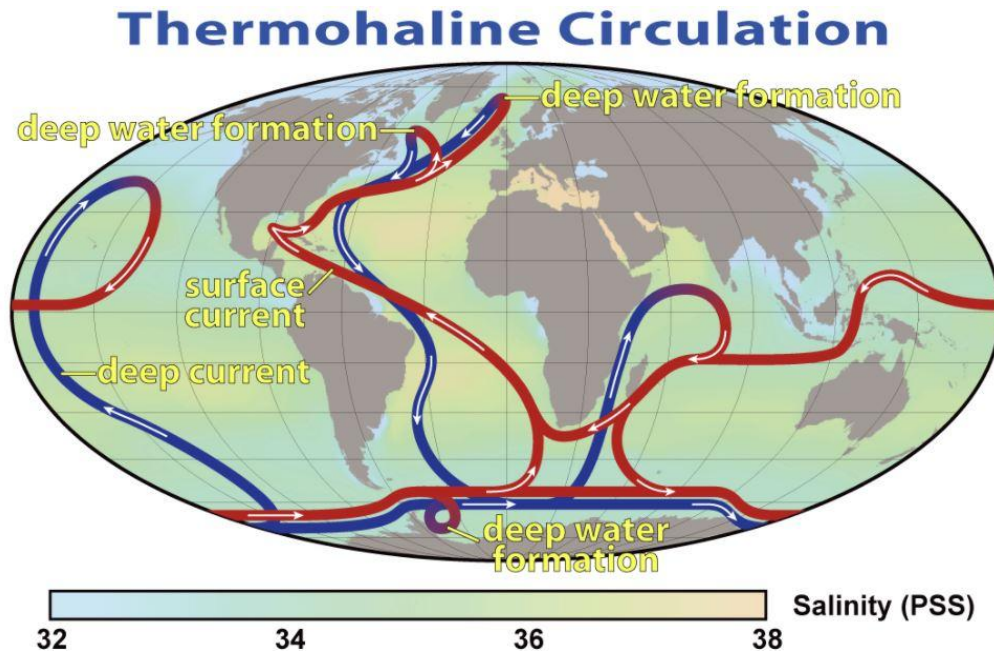


Figure 1. 1 Global thermohaline circulation map. Image from NASA Earth Observatory.

Heat exchanges are active between Arctic Ocean and atmosphere due to their temperature differences. The thermal conductivity of sea ice (2.25 W/mK) is lower than other metal materials such as aluminum (205 W/mK) and copper (401 W/mK). The thermal conductivity of sea ice is even lower when snow is on the sea ice (0.1 to 0.25 W/mK) (Shokr and Sinha, 2015). Sea ice can minimize heat exchanges between Ocean and atmosphere due to low thermal conductivity of sea ice (Maykut, 1978, 1982). Therefore, sea ice acts as an insulator between ocean and atmosphere, which prevent the ocean from losing heat.

Sea ice provides habitat, shelter, and breeding for plants such as algae and animals, including penguins, seals and polar bears as well. There is a concern that the loss of sea ice likely lead to the decrease of animal population (Shokr and Sinha, 2015).

In addition to the scientific importance of sea ice, the sea ice plays role in economic purposes such as marine navigation. Northern sea route is recently highlighted as Arctic sea ice melts, reducing navigation

coast for shipping. Records of recent shrinking sea ice concentration and thickness from remote sensing data help find seaway opening. The monitoring and prediction for sea ice will continue for identifying opening Arctic Ocean for the routes (Shokr and Sinha, 2015).

1.2 Arctic amplification

Over the past few decades, the Arctic sea ice has greatly diminished due to global warming and Arctic amplification (Parkinson and Cavalieri, 2008; Parkinson and Comiso, 2013). The Arctic amplification is that the increase of averages near-surface temperatures in the Arctic is more than twice than that of global average (Fig. 1.2) (Screen and Simmonds, 2010). Manabe and Wetherald. (1975) first suggested the amplified Arctic with climate model simulation. It is now considered as a natural feature in the global climate system (Serreze and Barry, 2011).

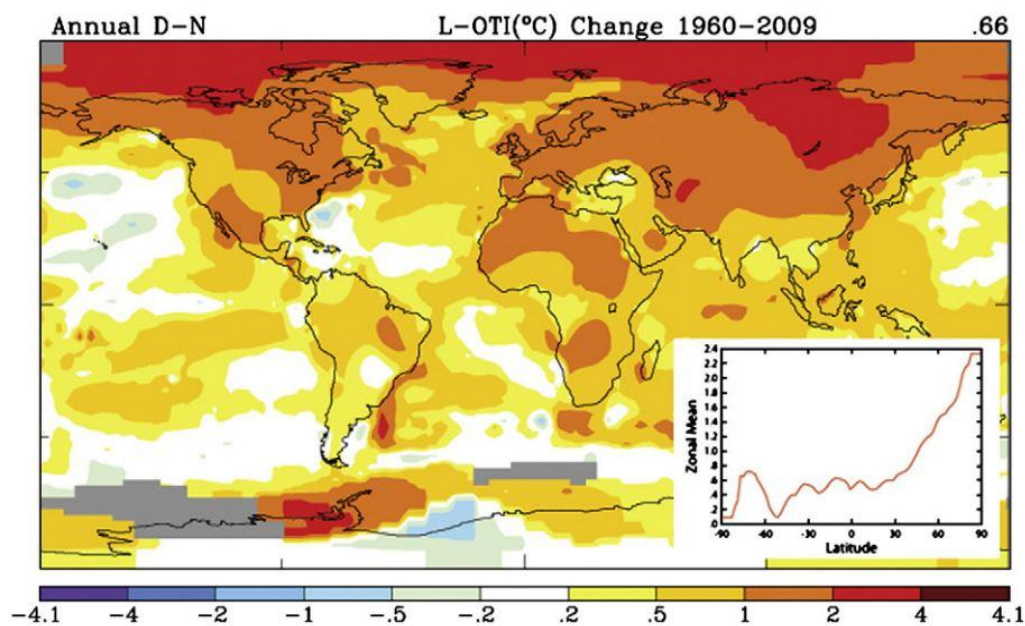


Figure 1. 2 Annual surface air temperature anomaly for the period 1960-2009 (50 years). The linear trend shows that average temperatures in Northern high latitudes is higher than other latitudes (Serreze and Barry, 2011).

Polyakov et al. (2002) suggested that there is no Arctic amplification using temperatures at land

stations and ice camps in 125 years. The temperature even decreased for 1940 to 1960. However, there was no study to support above research results. Serreze and Barry. (2011) assisted land stations around coast have limitation to represent over the ocean and needed gridded fields based on satellite retrievals or atmospheric reanalysis. Screen and Simmonds. (2010) certainly proved temperature over the Arctic Ocean is increasing trends using ERA-Interim data.

The Arctic amplification resulted in some changes over the Arctic Ocean. First, the Arctic amplification deepened ice albedo feedback, reducing snow on the land and ice on the ocean. Second, heat flux is converged into the Arctic, which makes change temperature in the Arctic. Third, a cloud cover and water vapor in the Arctic is increased. Francis and Hunter. (2006) document that the increase in the cloud cover and water vapor contribute to augment longwave flux to the surface, which is the attribution of northward sea ice retreat.

In response to Arctic amplification, melting sea ice is intensified and prolonged. As the sea ice melts, dark open water is exposed to the solar radiation, rising sensible heat contents in the mixed layer (Serreze and Barry, 2011). Since modern satellite era, 1979, it is observed that sea ice is continuously decreasing with negative trend (11.5 % per decade to 2010) in September. The historical minimum extent of sea ice in September was recorded in 2002, 2005, 2007 and 2012. The Arctic has transformed toward a ‘new Arctic’ by the increase in first year sea ice, a warmed ocean, and the increase in near surface air temperature (Maslanik et al., 2011). The ice albedo feedback is anticipated to strengthen due to massive loss of sea ice, lessening the cohesiveness of sea ice. The sea ice is becoming more vulnerable to atmospheric and oceanic forcing.

Accurate monitoring of sea ice parameters such as extent, concentration, thickness, volume, and snow depth on the sea ice is essentially needed to better understand polar and global climate system.

1.3 Remote sensing of sea ice

Since Polar region is basically located on remote area with extreme climate, it is hard to access. The in-situ measurements of sea ice are difficult. An ice breaker is commonly operated to measure various features of sea ice surface as well as ocean. However, it is limited in summer season and cannot cover a large scale. Sea ice has been measured with various techniques. Although upward looking sonar (Rothrock et al. 1999; Wadham. 1997), electromagnetic system (e.g., EM-31) (Eicken et al., 2011; Hass et al., 2006), and mass balance buoys (Perovich et al., 2006; Perovich et al., 2014) can measure accurate thickness and snow information on the sea ice, these techniques measure sea ice features within a limited

spatiotemporal resolution. Satellite remote sensing techniques can observe and monitor sea ices in a basin scale with a relatively high spatiotemporal resolution.

Three main sensors have been used for remote sensing of sea ice: 1) optical sensors, 2) thermal infrared sensors, and 3) microwave sensors.

Applications of optical remote sensing for sea ice is relatively inefficient due to the interruption of clouds and cannot be used without sun light while it provides much higher spatial resolution under the clear sky and easy to interpret. The albedo of sea ice measured using Advanced Very High Resolution Radiometer (AVHRR), providing seasonal albedo for Arctic sea ice over the vast area (Lindsay and Rothrock, 1994).

Thermal infrared (TIR) remote sensing can provide data regardless of sun light. However, it is also affected by the presence of clouds because the clouds emit the amount of radiation in the spectral band 10-12 μm wavelength. A representative TIR-based sea ice parameter is ice surface temperature (IST). Yu et al. (1995) retrieved IST using radiance 11.0 μm from AVHRR since polar atmosphere is almost transparent under clear sky condition. IST products is being produced by MODerate Imaging Spectroradiometer (MODIS) 31 and 32th band with an advanced equation for retrieval of IST using a split window technique, which is for the consideration of water vapor content in the atmosphere using the difference between 11.0 and 12.0 μm (Hall et al., 2004).

Passive and active microwave remote sensing have been widely used to observe polar region because microwave penetrates through cloud, dust, and rainfall owing to their relatively long wavelengths (> 10mm) as well as it can observe during both day and night. While passive microwave sensors measure emitted radiation from objects, active microwave sensors transmit signals and measure backscatter after reflecting surface. Passive sensors on the satellite can observe sea ice with a synoptic scale and high temporal resolution because of their wide swath. Active sensors (i.e., Synthetic Aperture RADAR, SAR) on the satellite have been used for the small scale process of sea ice and ship navigation (up to a few meters).

In contrast to TIR radiation affected by the physical temperature, passive microwave (PM) radiation is mainly affected by the emissivity of radiating layer. The emissivity in the wavelength of microwave is dominantly influenced by the properties and physical composition of medium, including surface roughness, salinity, crystalline structure, and moisture contents. Sea ice have higher emissivity, emitting high energy than open water in the microwave region. This is the fundamental principle for discriminating between sea ice and open water using PM remote sensing. Sea ice concentration describes how much

occupies ice fraction in a specific grid resolution, which is one of the longest climate satellite based parameters since late 1978. There are various algorithms to retrieve the sea ice concentration using different channels and satellites such as Special Sensor Microwave Imager/Sounder (SSMIS) and Advanced Microwave Scanning Radiometer (AMSR)-E and 2 (Andersen et al., 2007; Ivanova et al., 2014). Sea ice extent defines a region where is covered with ice, calculating the number of cells that sea ice concentration over 15%. A thicker sea ice has lower salinity content than thin sea ice because brine is rejected by growing sea ice. Thus, the emissivity of thin sea ice is higher than that of thick sea ice, differentiating sea ice type.

Active microwave sensors (i.e., SAR) also can be used for the observations of sea ice. While the SAR provides much higher spatial resolution than passive microwave, pre-process for SAR data is difficult and it is hard to interpret. The SAR is useful for fine scale sea ice process such as deformation, polynya, and sea ice leads. It is also can be used for the validation of passive microwave data.

1.4 Sea ice altimetry

Sea ice thickness is significant parameter in a climate system as well. Additionally, climate models need accurate and detailed sea ice thickness information for the successful projection of future climate because sea ice thickness plays important role in controlling heat flux between atmosphere and ocean. Laser and radar satellite based altimeter are commonly used sensors to measure sea ice thickness. Laxon et al. (2003) firstly retrieved sea ice thickness using European Remote Sensing Satellite-1 (ERS-1) and ERS-2 satellite data based on radar altimeter but observational latitude was just up to 80°N. Ice, Cloud, and land Elevation Satellite-1 (ICESat-1) was launched to observe elevation change in polar region by NASA in 2003, carrying a laser altimetry. After the launch of ICESat-1, the retrieval of sea ice thickness was possible with a basin scale. ICESat-1 measured Arctic and Antarctic sea ice thickness using various methods, revealing declining sea ice thickness (Kwok et al., 2007; Zwally et al., 2008; Farrell et al., 2009). Unfortunately, it stopped due to the failure of its main instrument in 2009. CryoSat-2 has been operating to observe sea ice thickness by radar altimetry since 2010. The CryoSat-2 can provide temporally continuous monthly sea ice thickness (Laxon et al., 2013; Ricker et al., 2014; Kurtz et al., 2014; Lee et al., 2016). The major difference between ICESat and CryoSat-2 is that the wavelength bands is different. While the wavelength of ICESat main sensor, Geoscience Laser Altimeter System (GLAS) is 1064, 532 nanometer (infrared, visible green light), the wavelength of CryoSat-2 main sensor, SIRAL is 13.575 GHz. CryoSat-2 radar signal can penetrate snow depth but ICESat-2 cannot penetrate snow depth due to short wavelength, which possibly estimate snow depth using the elevation difference. The size of footprint is

also different. ICESat's footprint is ~ 70m, enabling more specific observation than CryoSat-2. However, it takes about two months to cover pan-Arctic using ICESat and is easily affected by clouds. CryoSat-2 needs a one month to cover pan-Arctic because the footprint of CryoSat-2 is ~500 m. However, there are some uncertainty factors that interferes successful estimation of sea ice thickness. Snow depth is vitally needed for estimation of sea ice thickness using hydrostatic assumption equation. Zygmuntowska et al. (2014) assessed that snow depth is the most contributing variable in terms of uncertainty. Snow depth from Warren et al. (1999) is currently used, which cannot capture year-to-year variability. For radar altimeter, radar signal can penetrate snow depth but the penetration depth cannot be readily quantified since it depends on snow conditions such as wet or dry. Finally, the density of sea ice, snow, and sea water in hydrostatic assumption is used as fixed value. In order to retrieve more accurate and precise sea ice thickness, above uncertainty factors should be resolved.

1.4.1 Basic principle of radar altimetry

Satellite radar altimeters basically measure the distance between satellite and surface on the Earth (i.e., ocean, sea ice, and ice sheet). The radar altimeter transmits signals to the Earth and receives reflected echoes from the surface. The range (R) (i.e., elevation between satellite and Earth surface) can be measured by multiplying the time that takes transmitted electromagnetic pulse to arrive Earth surface at nadir point and receive to the altimeter and the speed of light. The time is the two-way of travel time (t). The electromagnetic wave in vacuum propagates with the speed of light (c). The range can be written as

$$R = \frac{ct}{2} \quad (1)$$

However, the electromagnetic waves can be decelerated and refracted through the atmosphere by water vapor and ionization.

1.4.2 Concept of SAR altimetry and CryoSat-2

Traditional beam-limited radar altimeters such as ERS 1/2 and Envisat have relatively coarse spatial resolution (i.e., 2-10 km). In order to improve lateral resolution, the aperture of radar need to be extended but the extension of aperture is practically impossible on satellite. The extended aperture can be achieved by transmitting coherent signal with an along track direction.

CryoSat-2 (i.e., SAR altimeter, so called delay/Doppler altimeter) transmits burst of radar pulses (i.e., 64) with high Pulse Repetition Frequency (PRF, 18.181kHz), which forms Doppler beams because of the along-track movement of the satellite (Wingham et al., 2006). In this process, the footprint is divided into subsections. With the help of the high PRF, each Doppler beam is coherently correlated and pointed at the same location on the Earth surface. This is called beam stacking. Multi-looking is conducting by

averaging the stacking beams to reduce speckles and thermal noises (Salvatore. 2013). This process enables CryoSat-2 to reach high resolution of $\sim 300\text{m}$ along track and $\sim 1500\text{ m}$ across track, which can identify small leads between sea ices for the retrieval of sea ice thickness.

Radar signals of each of the three target features have different characteristics because of the impact of several factors, especially surface roughness, on the signals. In particular, flat surfaces produce strong signals, and rough surfaces produce weak signals. The temporal distribution of power when signal radar signal reaches the surface is called waveform. The shape of the typical waveform of ice floes is similar to that of ocean (Figs. 1.3a and 1.3b). The sea ice waveform has large variation as it contains both diffuse (e.g., from ice floes and ridges) and specular (e.g., from lead and new ice) signals. In particular, since the surface of MYI is rougher than that of FYI, more diffuse reflection occurs on MYI. Leads have a typical specular reflection and symmetric waveform because they are relatively flat and there is little surface wave in leads (Fig. 1.3c).

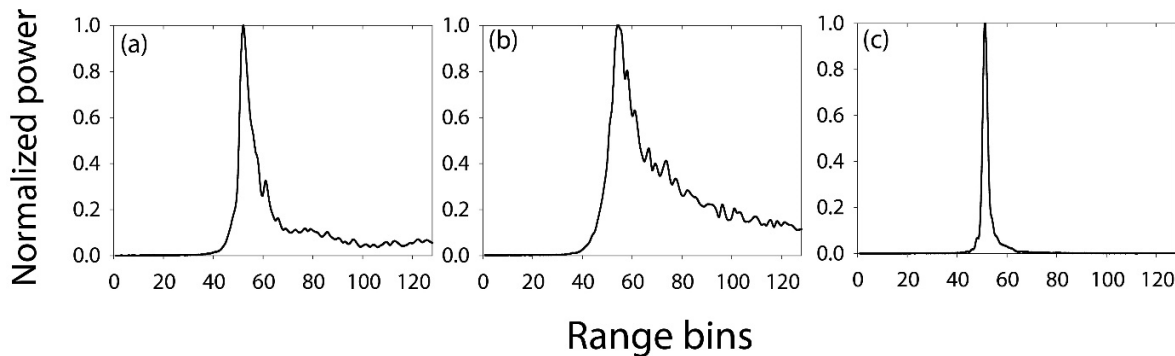


Figure 1. 3 Typical normalized echo power waveform of CryoSat-2 SAR mode data over (a) sea ice, (b) ocean, and (c) leads.

In order to determine surface elevation, a retracking algorithm should be applied to waveforms. Various retracking algorithms have been developed depends on type and it tracks main scattering horizon at the leading edge. The TFRMA algorithm one of the retracking algorithms is explained in detail in the section 2.3.1.

CryoSat-2, carrying SIRAL was launched in September 2010 by the European Space Agency (ESA). CryoSat-2 is a satellite dedicated to Polar research. SIRAL is a radar altimeter with a central frequency of 13.575 GHz (K_u -band) and a bandwidth of 320 MHz. CryoSat-2 takes an advantage of SIRAL to detect

smaller leads (e.g., ~ 300 m) with an efficient use of the instrument's energy compared to the previous radar altimeter missions such as GeoSat and Jason (Wingham et al., 2006). In this study, we used SAR mode, mainly operating on sea ice regions and SIN mode, mainly operating on steep regions such as margin of ice shelf and ice sheet of level 1b baseline C data, which has 256 and 1024 range bins, respectively (Scagliola, 2014). CryoSat-2 data is updated from baseline B to baseline C to improve quality of Level 1b products as well as Level 2. The main changes are as follows: 1) the number of range bin is restored. For example, the number of range bin of SAR mode changed from 128 to 256 and the number of range bin of SARIn mode changed from 512 to 1024. 2) the peak power of Level 1b waveforms for SAR and SARIn mode is reduced. 3) beam behaviour parameters such as stack standard deviation, stack skewness, and stack kurtosis are changed as peak power changed. It has three operation modes: Low Resolution Mode (LRM), Synthetic Aperture Radar (SAR), and SAR interferometry (SIN). ESA explains that data collected in SAR and SIN modes are optimized to estimate sea ice thickness because the sensor in the operation modes can measure sea ice characteristics with high spatial resolution comparable to the size of leads (ESA 2013). In the CryoSat-2 waveform data, the power of the received microwave signal is recorded in 256 range bins in SAR mode and 1024 range bins in SIN mode. The interval of each range bin is almost 1.563 ns (~ 0.234 m). Detailed specifications of CryoSat-2 are presented in Tab. 1.1.

Table 1. 1 The specifications of CryoSat-2 (SIRAL)

CryoSat-2	
Center frequency	13.575 GHz
Bandwidth	320 MHz
Pulse Repetition Frequency (PRF)	1.97 kHz (LRM) / 18.181 kHz (SAR and SIN)
Pulse duration	44.8 microsec.
Samples in echo	128 (LRM and SAR) / 512 (SIN)
Antenna footprint	0.29 km
Range bin sample	0.4684 (LRM) / 0.2342 m (SAR and SIN)

Five parameters (i.e., SSD, stack skewness, stack kurtosis, PP, and backscatter sigma-0) were used to distinguish leads from ice floes and ocean as they can represent surface characteristics such as surface roughness and dielectric property. SSD was available from L1B data; stack skewness and stack kurtosis

were available from Level 2I (L2I) data, which are provided by ESA. SSD is the variation of stacked power distribution with an incidence angle (Wingham et al., 2006). Stack skewness and stack kurtosis measure asymmetry and peakedness of the range stacked power distribution, respectively (Wingham et al., 2006). PP is commonly used to identify leads and ice floes (Laxon et al., 2013; Peacock and Laxon, 2004; Ricker et al., 2014; Rose et al., 2013). The equations to calculate SSD, stack skewness and kurtosis, and PP are summarized in Tab. 1.2.

Table 1. 2 The equations to retrieve SSD, stack skewness and kurtosis, and PP.

Parameter	Equation
SSD	$\frac{1}{2} \frac{\sum_{i=1}^N SP^2(i) \sum_{i=1}^N SP^2(i)}{\sum_{i=1}^N SP^4(i)}$
Stack skewness	$\frac{\frac{1}{N} \sum_{i=1}^N (SP(i) - \mu)^3}{[\frac{1}{N-1} \sum_{i=1}^N (SP(i) - \mu)^2]^{2/3}}, \mu = \frac{1}{N} \sum_{i=1}^N SP(i)$
Stack kurtosis	$\frac{\frac{1}{N} \sum_{i=1}^N (SP(i) - \mu)^4}{[\frac{1}{N-1} \sum_{i=1}^N (SP(i) - \mu)^2]^3} - 3, \mu = \frac{1}{N} \sum_{i=1}^N SP(i)$
Pulse peakiness	$\frac{k \times P_{\max}}{\sum_{i=1}^n p_i} \quad n = 128 \text{ (SAR) and } 512 \text{ (SIN)}$

where, SP stands for integrated stacked power that is not obtainable in the L1b data. The integrated stacked power is the summation of each single look echo power. p_{\max} is the maximum power of the waveform from L1b data and p_i is the power of i^{th} range bin. k is a multiplying factor based on the assumption that the waveform is almost centered in the range bins. A k value of 1 was used in this study following (Armitage and Davidson, 2014).

The radar backscatter sigma-0 (i.e., backscatter coefficient) from Level 2 (L2) data, documenting the observed surface, is a function of dielectric properties, the radar frequency, incidence angle, the target surface roughness, geometric shape and volume scattering (Wingham et al., 2006). The SAR L1b waveforms can be converted into watts using power scaling parameters that are available in the L1b product. The radar equation is solved using transmit power, range, and instrument gain and bias correction to retrieve backscatter sigma-0. A bias correction value is then applied to remove any residual bias (Salvatore 2014). Since these parameters are sensitive to change in surface condition, they can be used to discriminate leads from ice floes.

1.5 Overview of papers

Lead detection is crucial for estimating sea ice thickness using altimeters. Currently, simple threshold based lead detection methods were widely used. However, these methods could misidentify ices as leads because sea ice surface is very heterogeneous, which might underestimate sea ice freeboard. I proposed machine learning based lead detection methods such as decision trees and random forest, which is superior to thresholds based lead detection methods. Finally, machine learning approaches produced more accurate sea ice thickness than threshold based lead detection method compared to EM-bird (i.e., in-situ sea ice thickness data).

Sanggyun Lee, Jungho Im, Jinwoo Kim, Miae Kim, Minso Shin, Hyun-Cheol Kim, and Lindi J. Quackenbush. (2016): **Arctic Sea Ice Thickness Estimation from CryoSat-2 Satellite Data Using Machine Learning-Based Lead Detection**, *Remote Sensing*, 8(9), 698. doi: 10.3390/rs8090698.

Since threshold based lead detection methods, including machine learning methods mainly use beam behavior parameters and backscatter sigma-0, it is vulnerable to the updating CryoSat-2 baseline. For example, the beam behavior parameters and backscatter sigma-0 should be scaled to apply a newly updated baseline data. I developed an alternative lead detection method using waveform mixture algorithm, which can stably detect leads. A linear spectral analysis was applied to waveforms. The waveforms were regarded as endmembers. The waveform mixture algorithm is less influenced on the updating CryoSat-2 baseline and produced comparable results to decision tree method but better than previous threshold based methods.

Sanggyun Lee, Hyun-Cheol Kim, and Jungho Im. (2017): **Arctic Lead Detection Using a Waveform Mixture Algorithm from CryoSat-2 Data**, *The Cryosphere Discussion* (in revision), 10, 1-21. doi: <https://doi.org/10.5194/tc-2017-170>.

A significant drop of sea ice extent was occurred in November 2016. It is closely related to the extreme warm air temperature in mid-latitudes in August to September, which was record breaking temperature since 1980. After that an average temperature in October and November in the Arctic was also the highest since 1980. I investigated this sea ice anomaly phenomenon using sea ice concentration, sea ice thickness, and atmospheric reanalysis data. However, sea ice concentration and thickness in November 2016 have a different aspect. Preconditioned sea ice, extreme warming in mid-latitudes, warm southerly winds with strong cyclonic storm, and high SST were the major reasons for sea ice extent minimum in November 2016.

Sanggyun Lee, Daehyun Kang, Jungho Im, and Myong-In Lee. (2017): **Anomalous slow sea ice**

recovery in fall and winter 2016 by extreme waring event in mid-latitudes, *Geophysical Research Letter or Nature Geosciences*, to be submitted.

This dissertation can be divided into two parts. First, I have developed novel lead detection methods is essentially needed for the retrieval sea ice thickness as well as estimated sea ice thickness and lead fraction. Second, sea ice anomaly phenomenon in November 2016 was investigated using the sea ice thickness and volume is derived by waveform mixture analysis. The ultimate goals of this dissertation are as follows: 1) increasing the utilization of sea ice thickness data with novel lead detection methods, 2) analyzing sea ice anomaly phenomenon using estimated sea ice thickness and volume with a different perspective.

1.6 Research questions and hypotheses

Research question 1. Can improved lead detection method enhance the accuracy of satellite altimeter based sea ice thickness?

Research hypothesis 1.1: Machine learning approaches based lead detection method better discriminate lead, sea ice and ocean than existing methods.

Research hypothesis 1.2: The improved lead detection method produces more accurate sea ice freeboard and thickness.

Research question 2. Can waveform mixture algorithm detect leads accurately than traditional methods?

Research hypothesis 2.1: Waveform mixture algorithm can replace the traditional threshold based lead detection methods

Research hypothesis 2.2: Monthly lead fraction derived by waveform mixture algorithm shows seasonal cycle of lead fraction.

Research question 3. What factors contribute to slow recovery of sea ice in November 2016?

Research hypothesis 3.1: Anomalous high air temperature in mid-latitudes in August to September, preconditioned sea ice, warm southerly winds, and high SST may contribute sea ice anomaly in November 2016.

Research hypothesis 3.2: Sea ice volume derived by thickness provides a new insight for the analysis of sea ice minimum.

Chapter 2

2. Arctic sea ice thickness estimation from CryoSat-2 satellite data using machine learning-based lead detection

2.1 Introduction

Sea ice impacts the Earth's radiation balance because thermal feedback between the Sun and the Earth is highly sensitive to sea ice reflectivity. Thus Arctic sea ice is considered an important factor in understanding the global climate change process (Screen and Simmonds. 2010). The reflectivity of sea ice strongly depends on the spatial distribution and extent of the ice (Lindsay 2001; Laine 2004), which have rapidly changed due to global warming over the past two decade (Parkinson and Cavalieri. 2008; Kang et al., 2014). Boe et al (2009) used various climate model simulations to predict that the Arctic Ocean would probably be ice-free by the end of the 21st century. Furthermore, several studies have shown that the decline of sea ice is occurring faster than model predictions (Stroeve et al., 2007; Wang and Overland, 2012). Thus, there is an increasing need for accurate monitoring of sea ice concentration and thickness to better understand polar and global climate systems and processes.

Sea ice thickness has been measured with various methods. While direct field measurements of sea ice thickness using a submarine upward looking sonar (Rothrock et al., 1999; Wadhams, 1997) or an electromagnetic system (e.g., EM-31) (Eicken et al., 2001; Haas et al., 2006) can provide accurate ice thickness information, such techniques can only be applied to local areas within a very limited time frame. Observation of sea ice thickness over vast areas has utilized various space-borne radar and laser altimeter sensors (Laxon et al., 2003; Kwok et al., 2007; Laxon et al., 2013; Rose 2013; Kurtz et al., 2014; Ricker et al., 2014) . Laxon et al. (2003) retrieved sea ice thickness using European Remote Sensing Satellite-1 (ERS-1) and ERS-2 satellite data based on radar altimetry. Kwok et al. (2007) also estimated sea ice thickness using Ice, Cloud, and land Elevation Satellite (ICESat) data based on laser altimetry. Unfortunately, the operation of ICESat stopped in 2009 due to failure of its main instrument. Since the launch of CryoSat-2 in 2010, researchers have developed various methods to use the radar altimetry observations to estimate sea ice thickness from CryoSat-2 data (Rose et al., 2013; Kurtz et al., 2014; Laxon et al., 2013; Ricker et al., 2014).

Sea ice thickness can be estimated from sea ice freeboard based on isostasy (Forsström et al., 2011). Derivation of sea ice freeboard is an important procedure for estimating the ice thickness by laser or radar altimeter measurements. In particular, identification of leads (i.e., fractures between sea ice floes) is crucial to estimate the freeboard. The height of leads extracted by such measurements enables calculation of the local sea surface height (LSSH), and then freeboard can be estimated using LSSH, actual sea

surface height, and the surface elevation of the ice extracted by altimetric measurements. Kwok et al. (2007) detected leads through direct comparison between the surface elevation profiles extracted by ICESat data and near-coincident Synthetic Aperture Radar (SAR) images. Zwally et al. (2008) assumed that the lowest 2% values of the surface elevation profiles from ICESat would correspond to leads. In addition to these relatively simple methods, Farrell et al. (Farrell et al., 2009) proposed a threshold-based method to distinguish leads from ice floes using various parameters extracted from ICESat level 1b data such as gain, reflectivity, radiance, and waveform characteristics. In the case of CryoSat-2, pulse peakiness (PP) and stack standard deviation (SSD) parameters are frequently used for lead detection. For example, Ricker et al. (Ricker et al., 2014) used various waveform parameters such as PP, SSD, stack kurtosis, and sea ice concentration to distinguish leads from ice floes. Although these lead detection methods have been developed in several studies, determination of ice thickness from CryoSat-2 still suffers from a lack of precise lead discrimination (Onana et al., 2013). Simple thresholding methods might not perfectly distinguish leads from ice floes because parameters such as PP, SSD, stack skewness, stack kurtosis, and backscatter σ_0 (section 2.1) typically contain aliasing between leads and ice floes, which can result in large errors and uncertainties in sea ice thickness estimates. Therefore, advanced techniques to optimize such thresholds and minimize the associated errors are needed. This study proposes decision tree and random forest machine learning approaches to identify leads and ice floes from CryoSat-2 and MODIS in order to estimate sea ice thickness.

2.2 Data

Freeboard height and ice thickness for March and April in 2011–2014 were calculated from CryoSat-2 data based on machine learning based-lead detection approaches. MODIS and sea ice type data were used as ancillary data when estimating sea ice thickness. The estimated ice thickness was validated using CryoSat Validation experiment (CryoVex) field campaign data (i.e., airborne electromagnetics data) over northwestern Greenland acquired in April 2011.

2.2.1 MODIS

MODIS onboard the Terra and Aqua satellites, which were launched in 1999 and 2002, respectively, has 36 spectral bands from 0.4–14.4 μm and plays a vital role in observing the Earth's environments such as the land, lower atmosphere, and oceans. MODIS images are an ideal way to separate leads and ice floes because of the albedo difference between the two. MOD02QKM, one of the MODIS L1B products, is a calibrated and geolocated dataset with two bands (0.645 μm and 0.858 μm) at 250 m ground sample distance. In this study, training data of leads, ice, and ocean for the machine learning models were extracted from MOD02QKM images through visual interpretation based on reflectance differences.

2.2.2 Sea ice type

European Organization for the Exploitation of Meteorological Satellites (EUMETSAT) Ocean & Sea Ice Satellite Application Facility (OSI SAF) provides sea ice type data (<http://osisaf.met.no/p/ice/>) with 10 km resolution. The sea ice type includes First-Year Ice (FYI) and Multi-Year Ice (MYI) based on differences in ice surface roughness. The sea ice type was used as an input variable to calculate sea ice thickness from ice freeboard.

2.2.3 Airborne Electromagnetics data

The CryoVex airborne and field campaign was conducted to validate the measurements of CryoSat-2. As a part of the campaign, sea ice thickness was measured with an airborne electromagnetic (AEM)-bird sensor onboard the AWI Polar-5 aircraft. AEM uses electric conductivity differences between sea water and ice to measure sea ice thickness with an accuracy of ± 0.1 m over level ice (Haas et al., 2010). From 14–17 April 2011, AEM measured four tracks of ice thickness around the Lincoln Sea. Considering the length of the tracks and sample size, two of the data tracks were used to validate the sea ice thickness estimated from CryoSat-2 in this study.

2.3 Sea ice thickness estimation and machine learning algorithms for lead detection

2.3.1. Sea ice thickness estimation

Estimation of the snow-covered Arctic sea ice thickness from CryoSat-2 measurements is based on the assumption of hydrostatic equilibrium (Forsström et al., 2011) (Fig. 2.1). If the sea ice freeboard (h_{fb}) is accurately determined from altimeter measurements, the freeboard can be directly converted into sea ice thickness by Equation 1.

$$h_{si} = \frac{\rho_{sw}}{\rho_{sw} - \rho_{si}} h_{fb} + \frac{\rho_s}{\rho_{sw} - \rho_{si}} h_s \quad (1)$$

where ρ_{sw} , ρ_{si} , and ρ_s are the density of sea water, sea ice, and snow, respectively, and h_s is the snow depth. Although the density parameters and snow depth should be observed concurrently with the altimeter measurements to best estimate the ice thickness, this is challenging due to the extreme weather conditions of the Arctic Ocean. Thus, studies have used typical values based on field measurements or numerical simulation. For example, Giles et al. (2007) and Wadhams (1997) used the density of sea water, sea ice, and snow as 1023.8 ± 3 , 915.1 ± 5 , and 319.5 ± 3 kg/m³, respectively, from field observations. In this study, 916.7 kg/m³ and 882 kg/m³ were used as the density of FYI and MYI, respectively, according to Alexandrov et al. (2010). Snow depth simulated by the W99 climatology model of Warren et al. (1999) have been widely applied. However, the original W99 data only captures seasonal variability of snow depth. Kurtz and Farrell (2011) thus applied a modification to the snow depth data to reflect the

significant decline in MYI over the last few years. Kurtz and Farrell (2011) suggested reducing the snow depth over FYI by 50%. In this study, FYI and MYI were discriminated by the ice type products derived by EUMETSAT OSI SAF and we used the typical density and snow depth values derived by Kurtz and Farrell (2011).

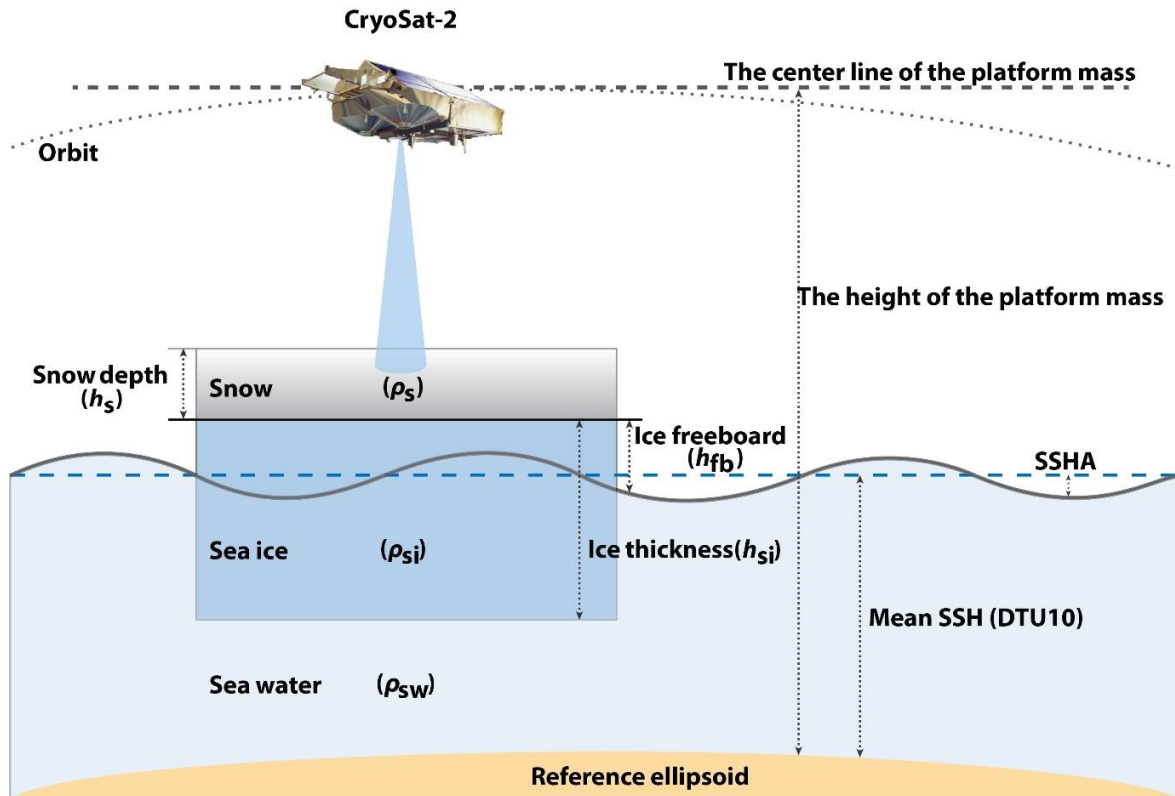


Figure 2. 1 Schematic diagram of the freeboard and thickness processing from CryoSat-2.

As mentioned above, it is important to determine the sea ice freeboard from CryoSat-2 data in order to successfully estimate the ice thickness. Fig. 2.2 shows the procedure to determine the sea ice freeboard from CryoSat-2 L1B data. Initially the surface height of the sea ice (i.e., the distance between the sea ice surface and the WGS84 ellipsoid) is estimated by Equation 2.

$$\eta_{\text{sea ice}} = H_{\text{sat}} - R_{\text{win}} - R_{\text{err}} - \Delta R \quad (2)$$

where H_{sat} is the height of the satellite platform mass above the WGS84 ellipsoid. R_{win} is the window delay field, which means the distance between the mid-point of the range bin (i.e., 64th range bin in SAR

mode and 256th range bin in SIN mode) of the waveform data and the satellite platform. R_{err} is a range correction term associated with the phase range due to geophysical properties such as atmospheric effects. These variables are given in CryoSat-2 L1B data; detailed descriptions and processing methods of the variables are well explained in Wingham et al. (2006). ΔR is another correction term derived by various retracking methods (Brown, 1977; Davis, 1997; Martin et al., 1983; Wingham et al., 1986). The aim of these terms is to determine the range offset between the mid-point of the range bin and a realistic range point of the leading edge of sea ice. The retracking method used in this study is the TFMRA (Rose 2013; Laxon et al., 2013; Ricker et al., 2014)

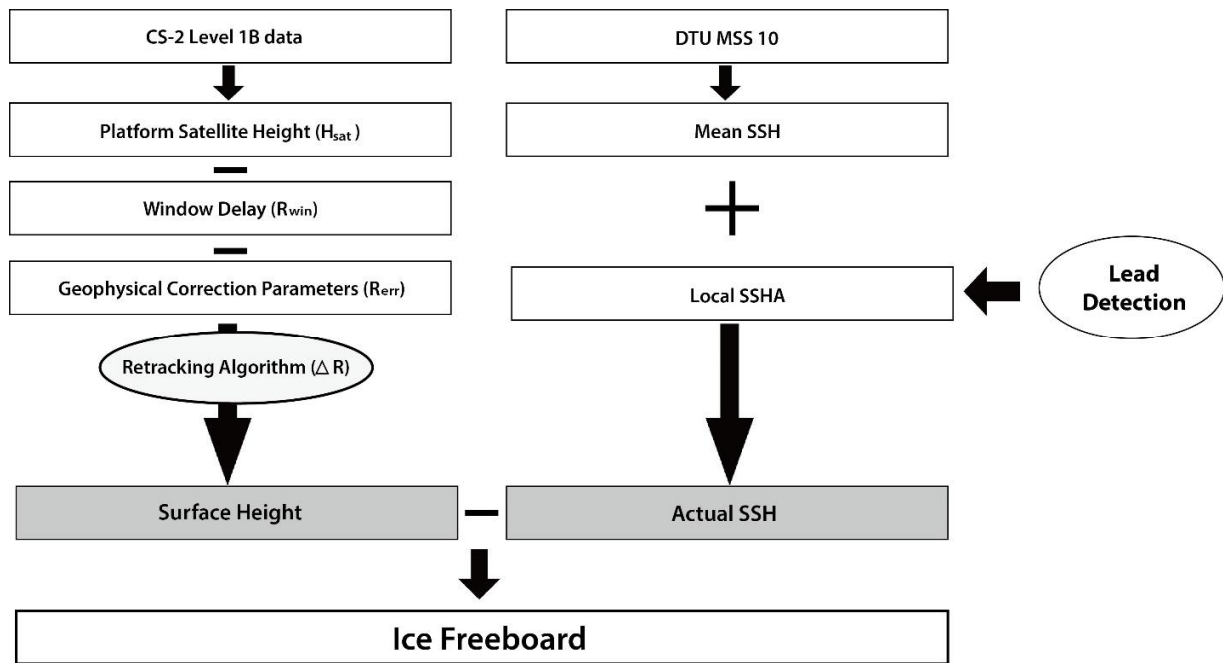


Figure 2. 2 The sea ice freeboard processing procedure using CryoSat-2 data.

Davis (1997) introduced the threshold retracking concept, which is useful for measuring the surface elevations of ice sheets or sea ice from radar altimeter data (Kurtz et al., 2014; Laxon et al., 2013; Ricker et al., 2014). The retracking method determines the range point of the leading edge between the threshold level and the range point of the first maximum power peak. The threshold level (ρ_1) is determined by

$$\rho_1 = P_n + \alpha(P_{max} - P_n) \quad \text{here, } P_n = \frac{1}{5} \sum_{i=n}^{\bar{n}+4} P_i \quad (3)$$

where P_n is the thermal noise of the CryoSat-2 system. α is the threshold value, the percentage of the maximum waveform amplitude above the thermal noise. P_{\max} is the first maximum power of the waveform. \hat{n} is the range bin of the first unaliased waveform. P_i is the power at the i^{th} range bin of the waveform. Finally, the retracking point (n_r) as the leading edge is estimated using the following equation.

$$n_r = (\hat{n} - 1) + \frac{P_1 - P_{\hat{n}-1}}{P_{\hat{n}} - P_{\hat{n}-1}} \quad (4)$$

where \hat{n} is the first range point exceeding the threshold level. It is essential to detect the first peak in the range bin. Here, Rose (2013) indicated that the maximum power peak in the range bin may not be the first peak due to time delay effects of complicating factors such as multiple scattering (i.e., in the surface) and volume scattering. Thus, the true range point (i.e., local maxima in the waveform) is detected by the peak detection algorithm, which identifies the range point using derivatives of the waveform signal (Ricker et al., 2014; Helm et al., 2014). Lastly, ΔR , the retracking correction, is calculated using Eq. 5.

$$\Delta R = C_{2m}(n_r - n_{tr}) \quad (5)$$

where n_r is the retracking point and n_{tr} is an on-board retracking point. C_{2m} is a factor to convert from range bins to meters, which is 23.24 cm/bin for CryoSat-2. Fig. 2.3 shows an example of the peak detection algorithm. This figure illustrates that the range point of the first maximum power (the open square) was found prior to the maximum power peak, and the retracking point (the open circle) was determined between the range point of the first maximum power and the threshold level (the dotted line). While various threshold values (α) have been used in the literature, several studies have found that thresholds of 40% and 50% give the best result for determining the leading edge of the ice floe (Ricker et al., 2014; Helm et al., 2014). A threshold of 40% was used in the retracking method in this study as it was frequently used in the literature (Rose 2013; Ricker et al., 2014).

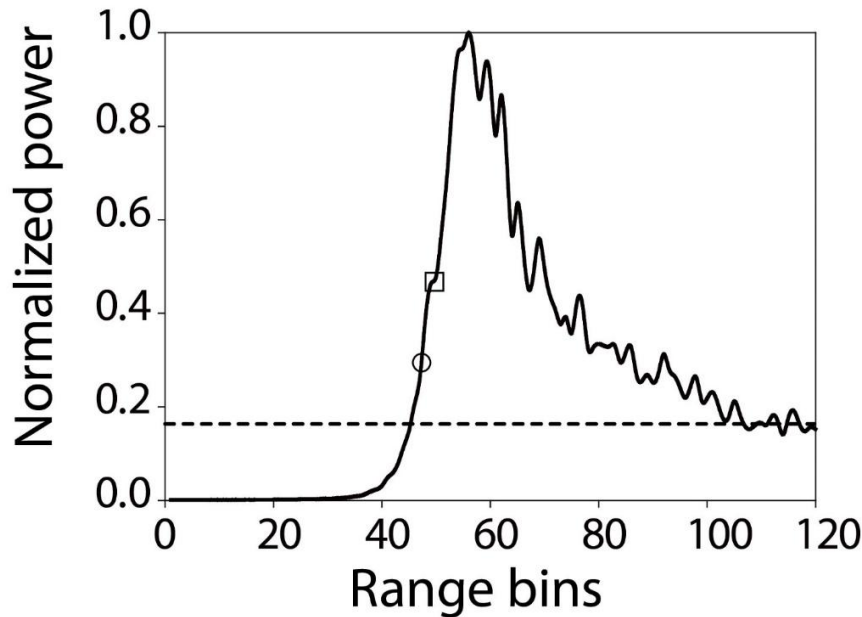


Figure 2. 3 A typical waveform of sea ice from CryoSat-2 data. The dotted line denotes the threshold level estimated by the threshold retracking method ($\alpha = 40\%$). The open square indicates the range point of the first maximum power peak determined by the peak detection algorithm. The open circle indicates the range point of the leading edge.

The next step removes the distance between the actual sea surface and the WGS84 ellipsoid from the surface height ($\eta_{\text{sea_ice}}$) in order to estimate the sea ice freeboard. In general, the actual sea surface height (SSH) is estimated from the sum of the mean SSH and local sea surface height anomaly (SSHA). Mean SSH data were obtained from the Technical University of Denmark 10 (DTU10) product (Andersen and Knudsen, 2009); local SSHA data were derived from the proposed lead detection method (section 3.2) that extracts leads from CryoSat-2 data. The SSHA observations were discontinuous because leads were detected at irregular intervals, thus linear interpolation and low-pass filtering were applied to make spatially continuous SSHA. The local SSHA was used to remove the surface height from the mean SSH at the leads. Although many studies have tried to develop effective lead detection methods, it is still very difficult to accurately identify leads due to limited reference data, irregular shape and size of leads, and characteristics leads share with ice or ocean. To overcome these challenges and correctly identify leads, this study proposed a novel lead detection method explained in section 2.3.2.

A correction to the sea ice thickness estimates from freeboard should be applied to account for the penetration of microwave radiation on snow and lower propagation speed in the snow pack. First of all, while typical microwave pulses do not penetrate the snow surface when the snow layer is wet during the melting season, it is well known that a K_u -band microwave penetrates the air/snow interface of dry and cold snow during the freezing season (Beaven et al., 1995; Connor et al., 2013). This complexity makes it difficult to determine the optimum penetration depth to correct the sea ice freeboard. Nevertheless, Laxon et al. (2013) believed that microwaves fully penetrate the snow layer. Since the speed of microwave is typically lower in the snow pack (Matzler and Wegmuller, 1987), it should also be corrected. However, given the uncertainty in these corrections, we did not apply the correction terms in order to enable consistent comparison with Laxon et al. (2013) and Ricker et al. (2014) who did not apply these corrections.

2.3.2. Machine learning algorithms for lead detection

In order to detect leads using machine learning approaches, reference samples were extracted using MODIS data. All 5-min MOD02QKM images above latitude 65°N in March and April 2011–2014 were downloaded. Cloud-free images were selected through visual interpretation. A total of 48 cloud-free March and April images were selected from MOD02QKM between 2011 and 2014 to clearly identify sea ice, leads, and ocean based on visual interpretation of the images (Fig. 2.4). However, visual interpretation with MODIS is not always reliable because the leads in the MODIS images could refreeze and new thin ice is formed. CryoSat-2 paths were geolocated over the MODIS images to extract five parameters (i.e., SSD, stack skewness, stack kurtosis, PP, and backscatter σ_0) for each class (i.e., lead, sea ice, and ocean). The time difference between CryoSat-2 paths and MODIS images was set to within 30 minutes (12 minutes on average) to minimize sampling errors as sea ice sometimes moves fast. Since there were more leads found in the Arctic in April than March, the number of samples for April was larger than that for March. It should be noted that we could not extract samples all over the Arctic Region because spatiotemporal coincidence between CryoSat-2 and MODIS was limited during the given time period. Lead reference samples were not collected when the size of leads was smaller than 250m considering the movement velocity of sea ice.

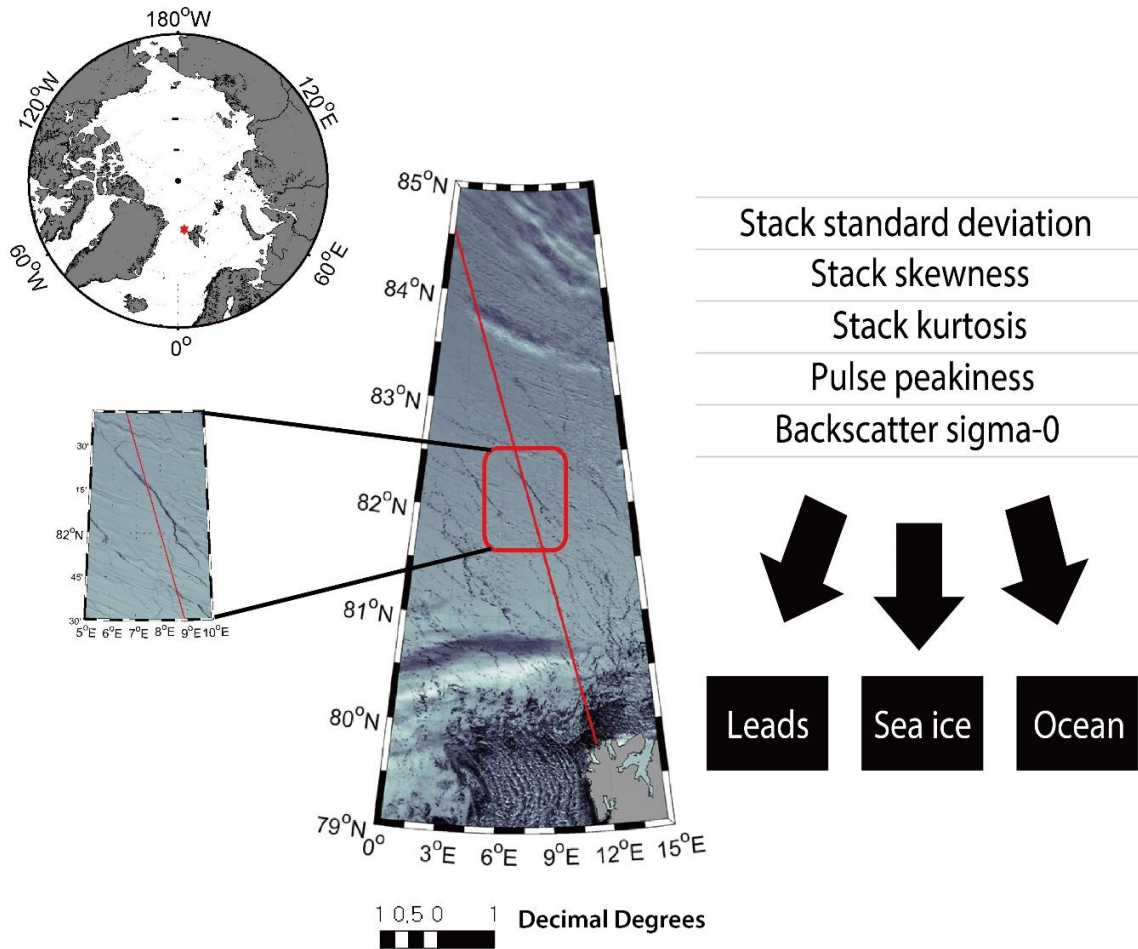


Figure 2. 4 Overlay of a CryoSat-2 path on a near-real-time MODIS image. The CryoSat-2 path (red line) was geolocated on the MODIS image in the north of Svalbard on 6 April 2011. The time difference between the two was 30 minutes. Based on visual interpretation, five parameters were extracted for target features (i.e., leads, sea ice, and ocean).

Since the characteristics of sea ice surface have monthly and annual variations, three schemes were examined to develop machine learning models in this study. The first scheme was classification of monthly data (CM), which used the reference samples by month regardless of year and developed the machine learning models for both months (i.e., March and April). The second was classification of annual data (CA), which divided the samples by year and developed the models separately for each year (i.e.,

2011, 2012, 2013, and 2014). Individual classifications (IC) used all reference data to develop the machine learning models to consider the tradeoff between transferability and accuracy.

Table 2. 1 Reference data used in the machine learning models by scheme and target feature.

Scheme	Target feature (number of observations)		
	Leads	Sea ice	Ocean
CM (March)	331	660	724
CM (April)	641	1284	1220
CA (2011)	179	357	357
CA (2012)	458	919	919
CA (2013)	209	419	420
CA (2014)	126	249	248
IC	972	1944	1944

In order to detect leads, we used two rule-based machine learning approaches: decision trees and random forest. Decision trees are one of the most widely used machine learning algorithms for inductive inference. To implement decision trees, See5.0 was used. See5.0 recursively splits training data into subdivisions based on a set of attributes defined at each node in a tree. An attribute is selected at each node and two branches that descend from that node use a value of the attribute as a threshold. Selecting an attribute (i.e., STD, stack skewness, stack kurtosis, PP, or backscatter sigma-0 in this study) at each node is crucial for successful classification. In general, statistical properties such as information gain or the Gini index are used to choose an appropriate attribute in decision trees. See5.0 uses information gain to select which candidate attribute is used at each node. See5.0 has been widely used for various remote sensing applications, including land cover/land use classification (Im et al., 2008a; Lu et al., 2014), climate region delineation (Rhee et al., 2008), vegetation species mapping (Li et al., 2013), ice mapping (Kim et al., 2015), and change detection (Im and Jensen, 2005; Im et al., 2008b). Using a See5.0 decision tree has some advantages. First, it provides a non-parametric classification, and thus it does not require

any assumptions in terms of the distribution of training data. See5.0 can also handle non-linear relationships between classes and features, even with missing values. In addition, See5.0 transforms a decision tree into a series of production rulesets, which makes it easier and more straightforward for human interpretation of results.

Random forest uses an ensemble approach that combines a boosting sampling strategy and Classification And Regression Trees (CART) (Breiman 2001) to improve the weaknesses of a single CART such as overfitting and sensitivity to training data configuration. CART uses a Gini index to measure impurity from training samples while See5.0 uses the concept of entropy. The Gini index is defined as shown in equation (6)

$$\text{Gini index}(S) = 1 - \sum_{i=1}^c p_i^2 \quad (6)$$

where c is the number of classes and p_i is the proportion of S belonging to class i . Gini gain is used to identify the most appropriate attribute at each node. Since it is similar to the information gain, it is defined by replacing the entropy with the Gini index in the equation (6). However, a single CART is often unstable and tends to overfit training data. Bagging can overcome such weaknesses by creating on independent trees and help minimize errors that can be caused from unstable classifiers. Random forest produces numerous independent trees through two bagging-based randomization processes: 1) using a random subset of training data for each tree and 2) using a random subset of input variables at each node of a tree. Breiman (2001) pointed out that it is not necessary to use a separate dataset for model validation as random forest uses out-of-bag data (i.e., training data that are not used) for internal cross validation. A majority voting strategy is used to combine the results from multiple classifiers to determine the final class for a given sample. In addition, random forest provides the relative importance of a variable using out-of-bag data when the variable is permuted. Because of these strengths, random forest has proved robust in various remote sensing applications (Ghimire et al., 2012; Long et al., 2013; Maxwell et al., 2014; Rhee et al., 2014; Kim et al., 2014)

2.4 Results and Discussion

2.4.1 Characteristics of five parameters based on CryoSat-2 waveform

Fig. 2.5 depicts the box plots of the five parameters (i.e., SSD, stack skewness, stack kurtosis, PP, and backscatter sigma-0) by feature (i.e., leads, sea ice, and ocean) using the reference samples (refer to Tab. 2.1). Among the three target features, ocean showed the narrowest distribution for all parameters except SSD. This is because the ocean surface is relatively homogeneous. Since the state of the sea ice surface varies significantly, all parameters resulted in wide distribution in the sea ice plots. Waveform over ocean generally has higher backscattered signal intensity than that over sea ice because of the higher diffuse reflection of ocean. However, the backscatter sigma-0 value of ocean was lower than that of sea ice (Fig. 2.5). This might be because the ocean samples were mostly collected around the Svalbard islands, where strong winds frequently cause high waves, which may reduce the backscattered intensity. Leads showed large variation for all parameters because the size and shape of leads were diverse with different neighboring environments such as sea ice melting and re-freeze states, combined with the samples being collected in March and April across multiple years, which undoubtedly increased the variation of the parameter values. The narrow distribution of the SSD of leads in Fig. 5 implies that the range stacked power of single look echoes of around lead have high power, making the variation of range stacked power simple. The median values of each parameter seem to distinguish lead, sea ice, and ocean. However, the distribution of the parameter values of sea ice and leads partly overlapped, possibly due to off-nadir observations of CryoSat-2. This implies that simple thresholding approaches are not suitable to clearly identify leads from sea ice.

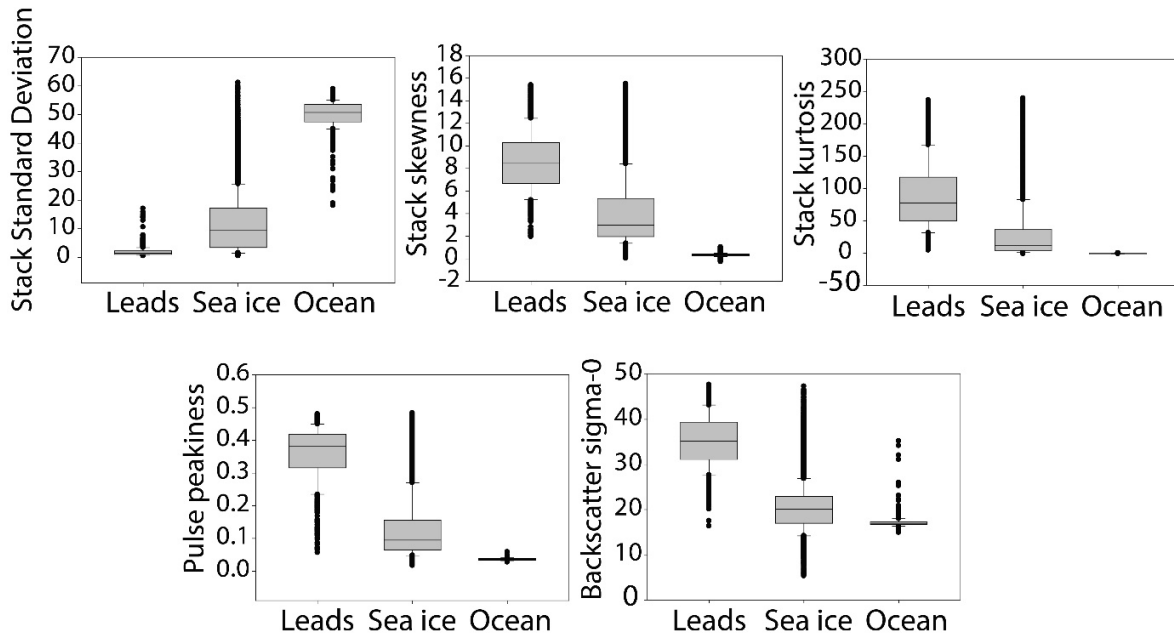


Figure 2. 5 Box plots of 5 parameters (i.e., SSD, stack skewness, stack kurtosis, PP, and backscatter sigma-0) over leads, sea ice, and ocean using the March and April samples from 2011 to 2014. The vertical height of the boxes indicates the interquartile range of the samples. While a parallel line inside the boxes means a median value of the samples for each parameter, the dots represent the outliers.

2.4.2 Comparison of lead detection performance

Both See5.0 and random forest produced similar classification results for the three features. Tab. 2.2 summarizes the overall accuracy by model and scheme through 10-fold cross validation. All of the cases produced very high overall accuracy (> 90%). The most common misclassification for both approaches was between leads and sea ice, possibly due to sampling around the boundaries between them. Since CM and CA resulted in varied accuracy patterns and did not produce significantly higher accuracy than IC, we focused the following discussion on IC. Using IC can reduce temporal variability by including all samples in the subsequent analyses including sea ice freeboard and thickness estimation.

Table 2. 2 Accuracy assessment results of See5.0 and random forest by scheme through 10-fold cross validation. The overall accuracy in percentage averaged for 10 folds is provided.

Scheme	See 5.0	Random Forest
CA (March)	99.50	99.43
CA (April)	93.47	90.40
CM (2011)	92.49	94.80
CM (2012)	94.87	96.96
CM (2013)	95.07	95.48
CM (2014)	94.40	91.60
IC	94.20	94.05

Tab. 2.3 presents relative variable importance for lead classification by model when using IC. While stack skewness and sigma-0 were used at every node in See5.0, SSD was not used at all. For the random forest analysis, sigma-0 was identified as the predominant contributing variable, followed by stack kurtosis, PP, and stack skewness. Similar to See5.0, SSD was the least contributing variable to lead detection in random forest. Stack skewness was useful because it was able to distinguish ocean from leads and sea ice with very low error. Interestingly, backscatter sigma-0 was considered a critical parameter for lead detection in both See5.0 and random forest, but it has not been used in previous studies for lead detection. Backscatter sigma-0 represents not only surface roughness but also dielectric properties, radar frequency, incidence angle, and geometric shape, while the other parameters are mainly sensitive to surface roughness. Tab. 2.4 summarizes threshold-based rules produced using See 5.0 by IC. Previous studies have used SSD, for example, Laxon et al. (2013) and Ricker et al. (2014) used $SSD < 4$ as one of the conditions to detect leads. However, SSD was not primarily used in the threshold-based rules in this study. It should be noted that the rules were an integration of multiple factors, which implies that the simple thresholding approaches might over- or under-estimate leads resulting in uncertainty in sea ice

thickness estimation.

Table 2. 3 Relative variable importance (i.e., contribution) to lead detection using See5.0 and random forest by IC.

	SSD	Stack skewness	Stack kurtosis	PP	Sigma-0
See5.0 Usage (%)	0	100	21	40	100
Random forest Mean accuracy decrease (%)	19.97	20.44	36.75	20.50	97.72

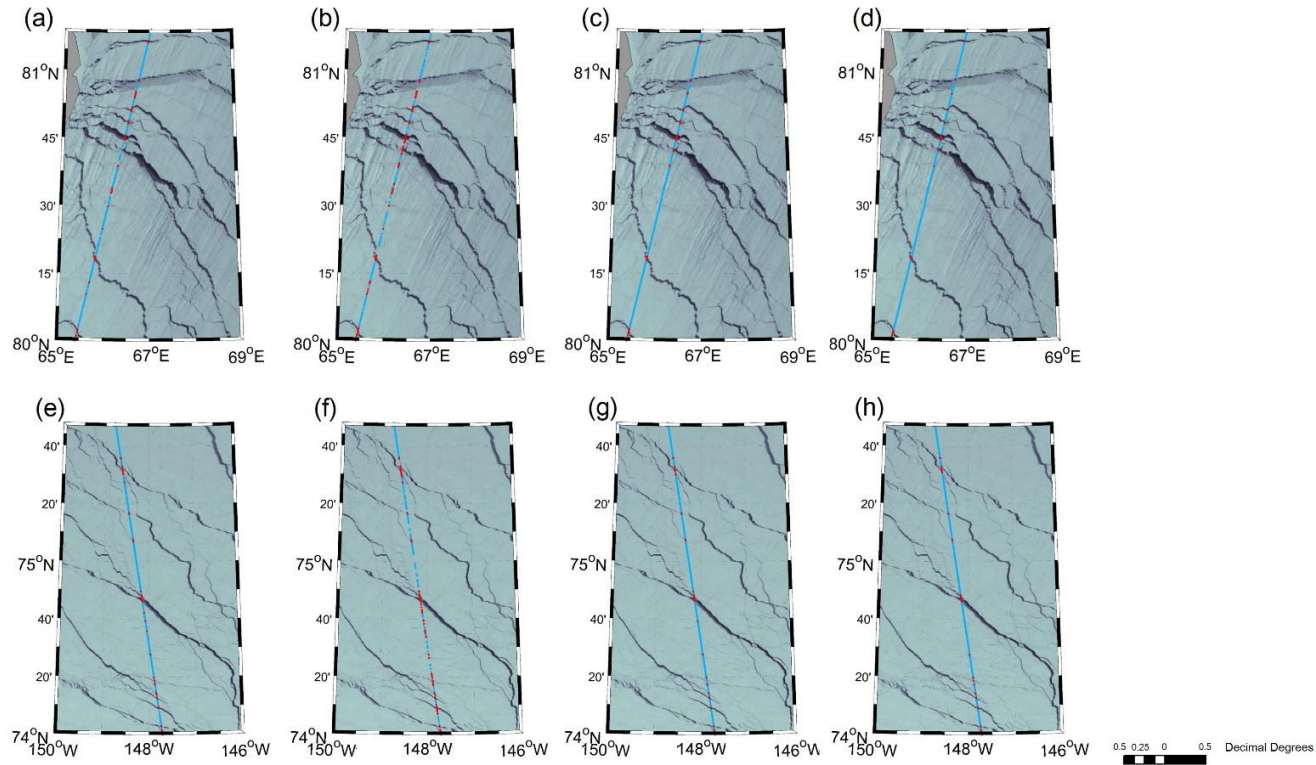
Table 2. 4 An example of threshold-based rules produced by See5.0 using IC to classify leads, sea ice, and ocean.

	SSD	Skewness	Kurtosis	PP	Sigma-0
Lead		> 0.73	> 17.53		> 27.8
	≤ 25.6	> 0.73	≤ 17.53		> 27.8
Sea ice		≤ 0.73			≤ 14.89
		≤ 0.73		> 0.043	14.89 < Sigma-0 < 16.48
		> 0.73			≤ 27.8
	≤ 25.6	> 0.73	≤ 17.53		27.8 < sigma - 0 < 31.47
Ocean		≤ 0.73		≤ 0.043	> 14.89
		≤ 0.73		> 0.043	> 14.89
	> 25.6	> 0.73	≤ 17.53		> 27.8

Fig. 2.6 shows two examples of identifying leads using four different lead detection methods. A

simple thresholding approach based on PP and SSD (i.e., $PP > 0.25$ and $SSD < 4$ for leads and $PP < 0.45$ and $SSD > 4$ for ice floes) used in Rose (2013) was adopted to identify leads (Figs. 2.6a and 2.6e). The simple thresholding method resulted in somewhat over-identification of leads; some leads were mistakenly found on the ice. Laxon et al. (2013) also used a similar thresholding approach based on PP (personal communication) and SSD (leads: $PP > 18$ and $SSD < 4$; ice floes: $PP < 9$ and $SSD > 4$), which also resulted in overestimation of leads on the ice (Figs. 2.6b and 2.6f). Although PP and SSD are considered useful parameters for lead detection, simple thresholding based on just two parameters appears insufficient for effectively distinguishing leads from ice. Since surface height on leads is considered as LSSH, if leads are identified on the ice then LSSH would be overestimated, which would result in an increased bias towards smaller freeboard and thinner sea ice estimates. On the other hand, the two machine learning approaches applied—See5.0 decision trees and random forest—resulted in improved lead detection and less overestimation of leads compared with the existing approaches (Figs. 2.6c/g and 2.6d/h, respectively). Different lead detection approaches were quantitatively assessed and compared (Tabs. 2.5–2.8) using error matrices. Since the approaches by Rose (2013) and Laxon et al. (2013) considered ice floes and leads only, i.e., excluding ocean, the accuracy assessment was conducted without ocean samples for consistent comparison between the proposed approaches and the existing literature. The machine learning approaches to lead detection resulted in higher overall accuracy and Kappa coefficients than the approaches used by Rose (2013) and Laxon et al. (2013). Both See5.0 and random forest produced high producer's accuracy for leads and sea ice. However, the user's accuracy for leads, as well as overall accuracy and kappa coefficient of random forest were slightly higher than those of See5.0. Random forest uses an ensemble approach based on numerous independent trees through randomization, which can avoid problems associated with sampling biases. On the other hand, See5.0 uses only a single tree, but provides more straightforward rules to understand the results at the cost of possible overfitting and sampling biases. Based on the lead detection results in this study, both See5.0 and random forest can be used to identify leads with minimal difference in the performance. However, in order to analyze the physical meaning among the parameters for lead detection, See5.0 would be better as it provides rulesets in simple forms, compared to the ensemble results of random forest. While all four lead detection methods have high producer's accuracy for both leads and sea ice, the existing approaches (i.e., Rose (2013) and Laxon et al. (2013)) produced much lower user's accuracy for leads than the proposed methods, implying overestimation of leads.

1



2

3 **Figure 2. 6** Examples of lead detection results around east Franz Josef Land on 11 April 2014 (a-d) and Beaufort Sea on 11 April 2011(e-h) using
 4 four methods: (a/e) Rose (2013), (b/f) Laxon et al. (2013), (c/g) See5.0 in the present study, and (d/h) random forest in the present study. Red and
 5 blue dots represent leads and sea ice, respectively

6

Table 2. 5 The error matrix based on the See5.0-based lead detection results for IC.

Reference Classified as	Lead	Sea ice	Sum	User's Accuracy (%)
Lead	36	5	41	87.8
Sea ice	6	192	198	96.7
Sum	42	197	239	
Producer's accuracy (%)	85.7	97.5		
Overall accuracy (%)			95.4	
Kappa coefficient (%)			84	

Table 2. 6 The error matrix based on the random forest-based lead detection results for IC.

Reference Classified as	Lead	Sea ice	Sum	User's Accuracy (%)
Lead	36	2	38	94.7
Sea ice	6	195	201	97.0
Sum	42	197	239	
Producer's accuracy (%)	85.7	98.9		
Overall accuracy (%)			96.2	
Kappa coefficient (%)			86.4	

Table 2. 7 The error matrix based on the lead detection results by the approach of Rose (2013).

Reference Classified as	Lead	Sea ice	Sum	User's Accuracy (%)
Lead	36	28	64	56.2
Sea ice	6	169	175	96.7
Sum	42	197	239	
Producer's accuracy (%)	85.7	85.8		
Overall accuracy (%)			85.7	
Kappa coefficient (%)			59.3	

Table 2. 8 The error matrix based on the lead detection results by the approach of Laxon et al. (2013).

Reference Classified as	Lead	Sea ice	Sum	User's Accuracy (%)
Lead	41	45	86	47.7
Sea ice	1	152	152	99.3
Sum	42	197	239	
Producer's accuracy (%)	97.6	77.2		
Overall accuracy (%)			80.7	
Kappa coefficient (%)			53	

Fig. 2.7 shows the comparison of the SSHA and freeboard from the different lead detection methods. SSHA is a subtraction of LSSH from the mean SSH, representing the relative vertical location of leads. The proposed machine learning-based lead detection methods (Figs 2.7a and 2.7b) detected fewer leads than the existing methods (Figs. 2.7c and 2.7d) with few leads above the latitude of 87°N, where leads are rarely found in April. Almost all the leads detected by the proposed See5.0 and random forest approaches were also detected by the approaches from Laxon et al. (2013) and Rose (2013). SSHA was linearly interpolated and smoothed using a 3×3 (pixel) moving average filter. The freeboard, a derivation of surface height from the sum of SSHA and mean SSH, was smoothed by a 30×30 (pixel) moving average filter to remove signal noise. While the overall shape of the freeboard lines with latitudes looks similar,

the average freeboards by approach—See5.0, random forest, Rose (2013), and Laxon et al. (2013)—were 0.095 m, 0.092 m, 0.089 m, and 0.090 m, respectively. The average freeboards of Rose (2013) and Laxon et al. (2013) were relatively underestimated compared to the freeboards by See5.0 and random forest because of their over-identification of leads on the ice especially over higher latitudes ($> 85^{\circ}\text{N}$; Figs. 2.7c and 2.7d). Laxon et al. (2013) found lower SSHA (Fig. 2.7h) between $76\text{--}80^{\circ}\text{N}$ that appeared to be ocean. However, since the proposed machine learning-based lead detection approaches discriminates ocean from sea ice and leads, ocean was excluded in the SSHA.

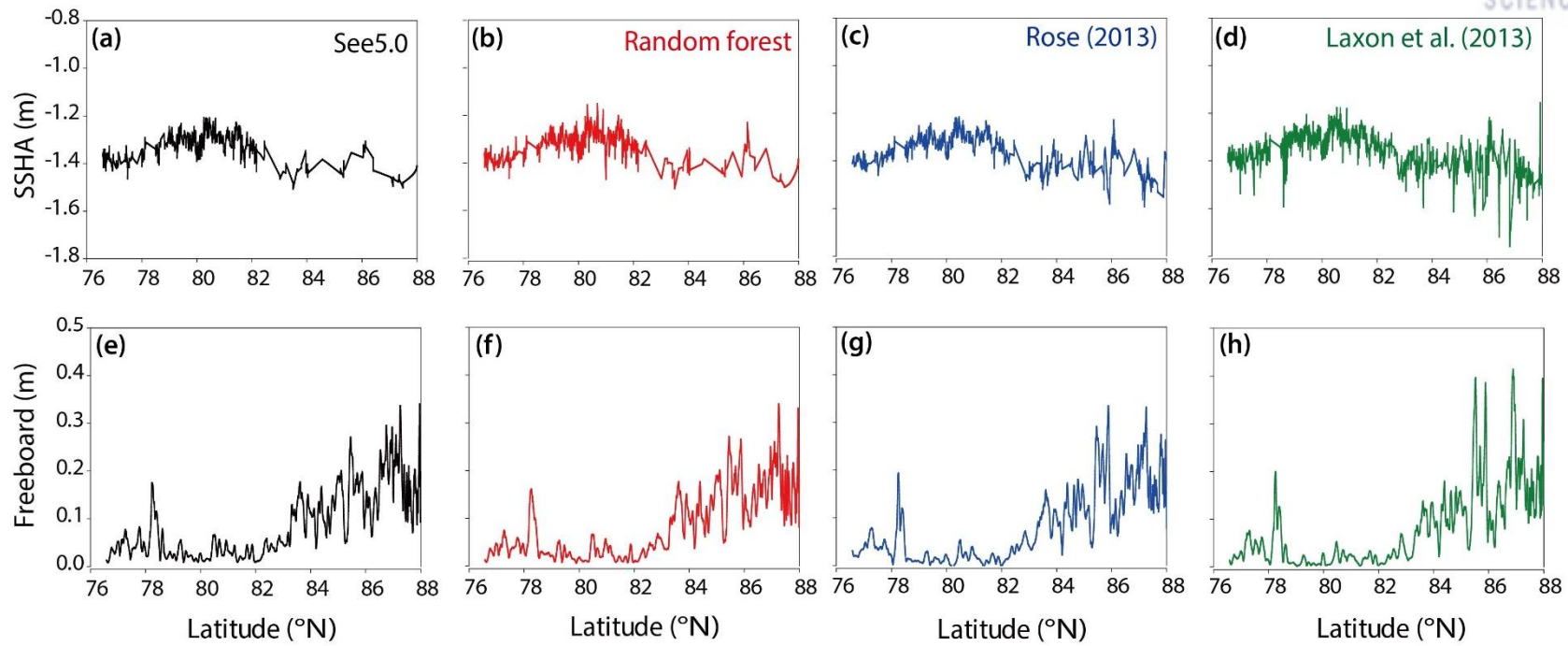


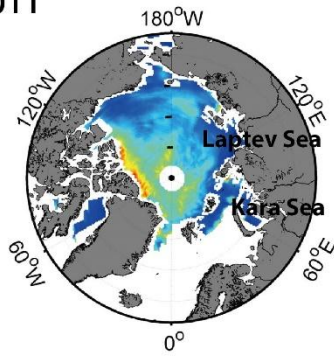
Figure 2. 7 SSHA and freeboard extracted by each method using CryoSat-2 data from UTC 03:47 to 03:57, 09 April 2012 based on IC: (a) – (d) are the interpolated and smoothed SSHA; (e) – (h) are the smoothed freeboard.

2.4.3 Spatial distribution of Arctic sea ice freeboard and thickness

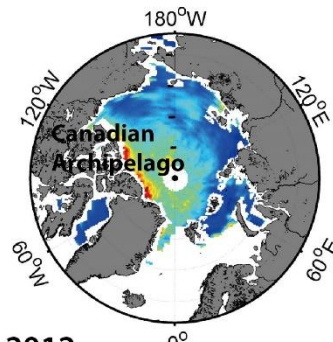
Figs. 2.8 and 2.9 present the IC ice freeboard and thickness maps, respectively, for March and April from 2011–2014 using a polar stereographic projection with $25 \times 25 \text{ km}^2$ grid. A typical MYI zone near the Canadian Archipelago and northwestern Greenland has relatively thick freeboard and thickness except for 2012. The retrieval of freeboard and thickness in these regions appears to show relatively poor LSSHA due to the very limited leads in the regions. On the other hand, sea ice freeboard and thickness around the Kara Sea and Laptev Sea were consistently stable and low for all cases during March and April from 2011–2014. Interestingly, unlike other years, sea ice thickness was relatively high in the central Arctic in 2012, while it was generally low in the typical MYI zone. Annual variability of sea ice thickness was high on the MYI zones, compared to the FYI zones. The amount of sea ice freeboard and thickness apparently diminished from 2011–2013.

Laxon et al. (2013) determined Arctic sea ice thickness from February to March 2012 using CryoSat-2 data. Although it was averaged for two months, the overall distribution of sea ice thickness over MYI zones was similar to the results of this study (not shown). Sea ice freeboard and thickness maps for March 2013 from this study were slightly different from the results in Ricker et al. (2014). This is possibly because the two studies used different smoothing approaches to waveform data, lead detection methods, and gridding approaches to CryoSat-2 track data. Farrell et al. (2009) showed two-month averaged sea ice freeboard maps from 2003–2008 using ICESat data. However, sea ice freeboard from ICESat will be different from the sea ice freeboard determined in this study because the height of the sea ice freeboard derived by laser altimetry (i.e., from ICESat) includes snow depth on the sea ice. Farrell et al. (2009) observed a slightly thicker sea ice freeboard between 2003 and 2008 (up to 0.75 m) than the 2011–2014 period in the present study. The major differences were found in the Canadian Archipelago, Northern Greenland, and the central Arctic where the freeboard was observed as being high in Farrell et al. (2009) while it decreased from 2011–2013 in this study.

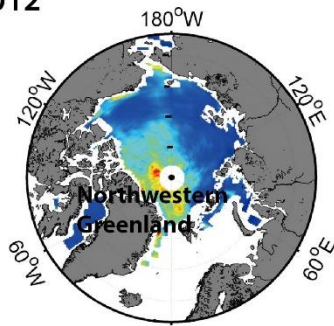
March 2011



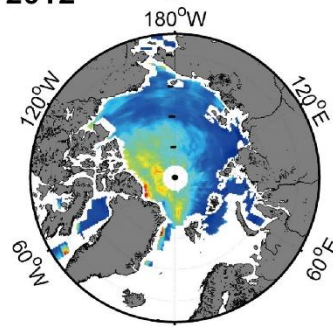
April 2011



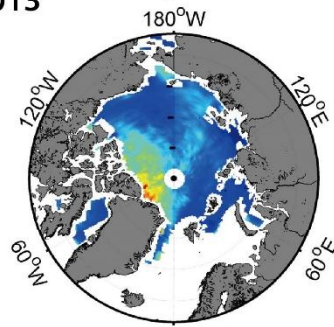
March 2012



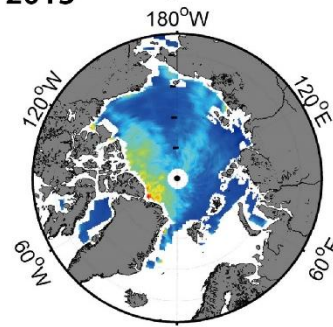
April 2012



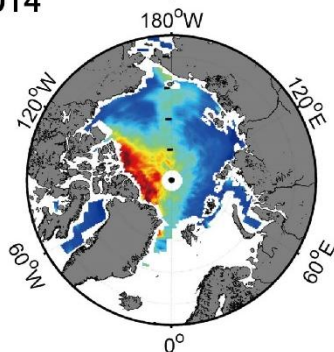
March 2013



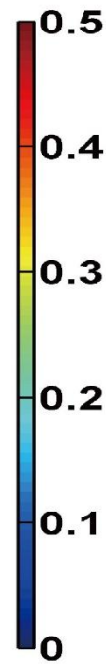
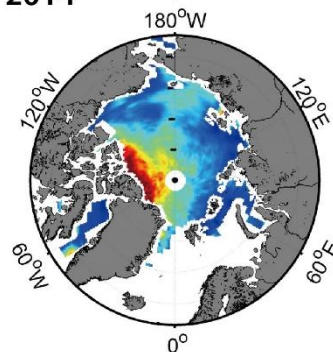
April 2013



March 2014



April 2014



Freeboard (m)

Figure 2. 8 Arctic sea ice freeboard from CryoSat-2 for March and April between 2011 and 2014 based on IC scheme. Non-sea ice areas were masked out using the EUMETSAT OSI SAF sea ice type data.

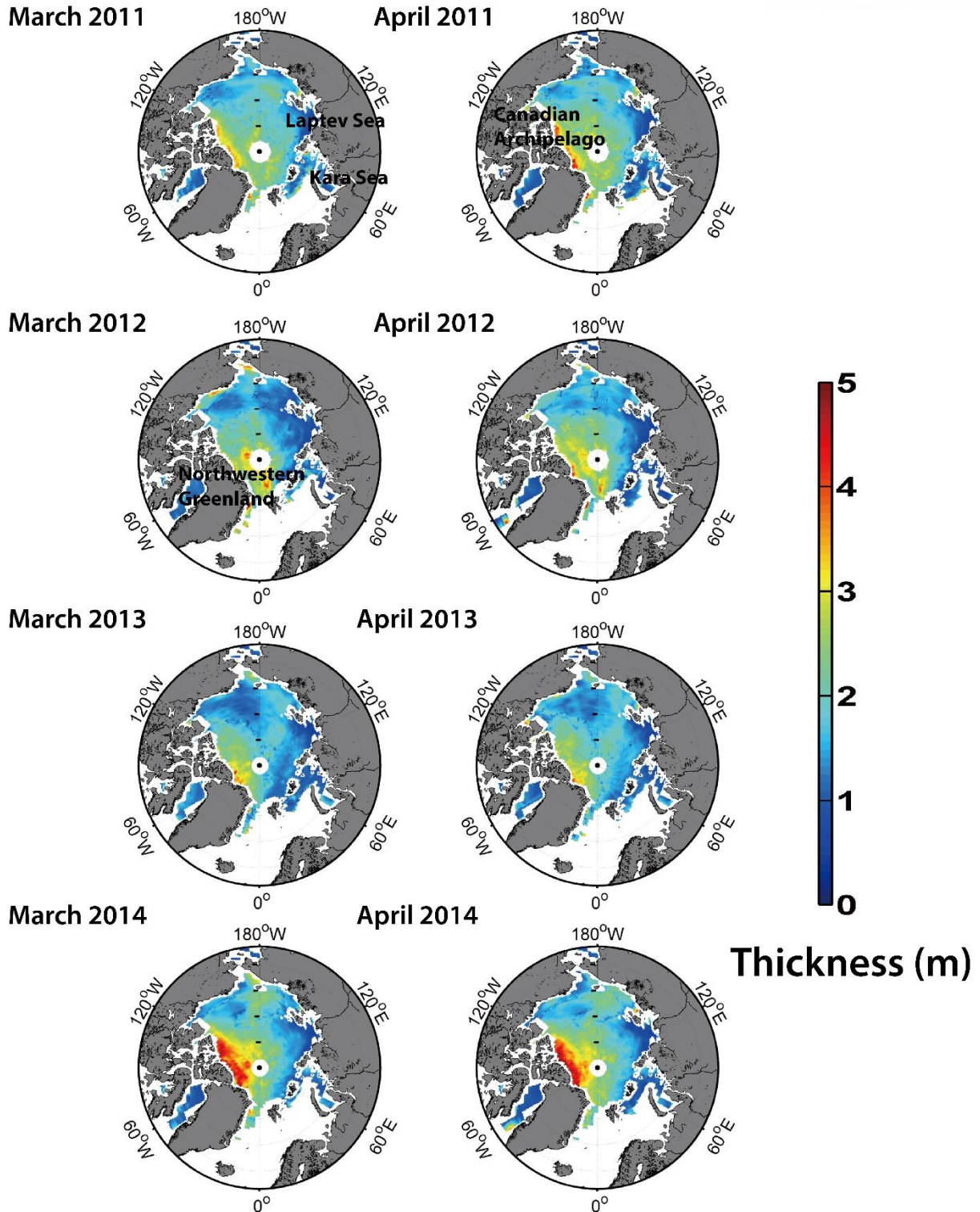


Figure 2. 9 Arctic sea ice thickness from CryoSat-2 for March and April between 2011 and 2014 based on the IC scheme. Non-sea ice areas were masked out using the EUMETSAT OSI SAF sea ice type data

2.4.5 Comparison with AEM-bird data

The monthly ice thickness that was averaged by grid using the novel machine learning-based lead detection approaches was compared to the averaged AEM-bird data collected 15 and 17 April 2011 during the CryoVex campaign as well as the thickness derived by the lead detection methods from Rose (2013) and Laxon et al. (2013). This comparison considered the three schemes and two lead detection methods (Fig. 10). The sea ice thickness determined using See5.0 with CA produced the best validation performance on both days with $r \sim 0.83$ and root mean square error (RMSE) ~ 0.29 m (Fig. 10c). (Connor et al., 2013)

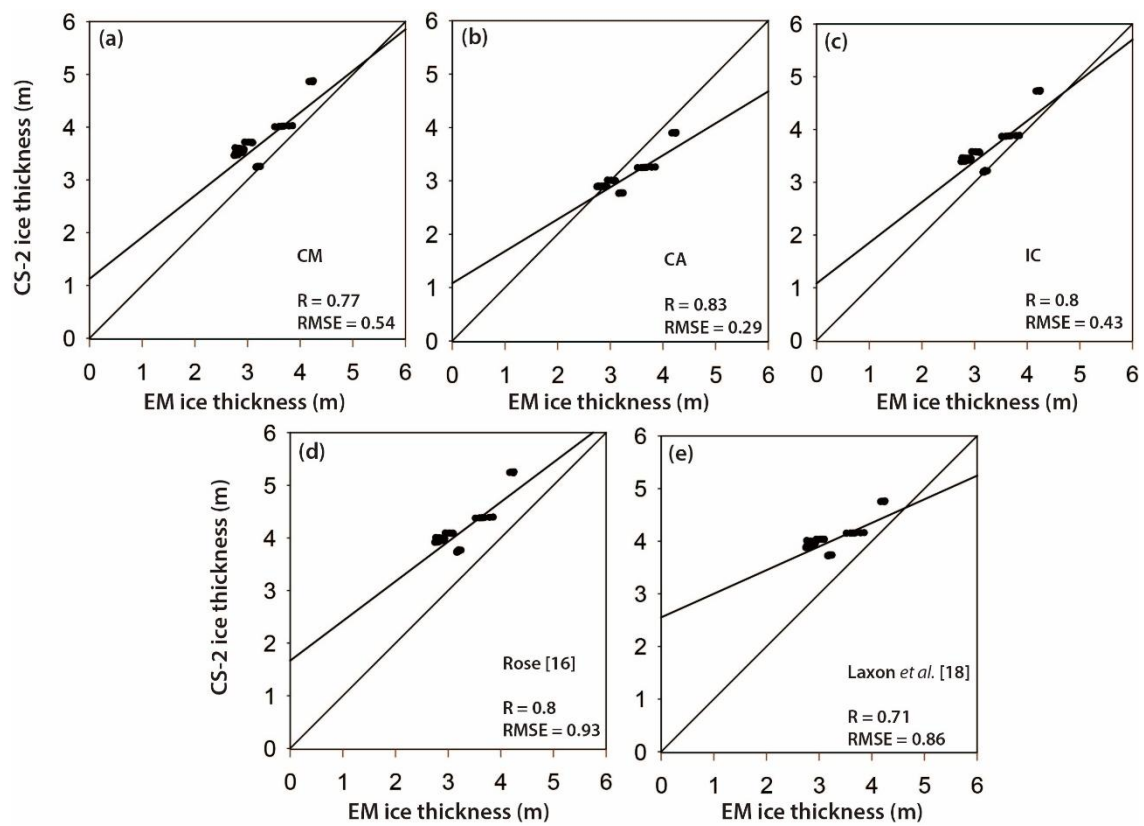


Figure 2. 10 Scatterplots between the Cryosat-2-derived sea ice thickness and the averaged AEM-bird ice thickness for validation.

While Rose (2013) and Laxon et al. (2013) produced similar performance, the sea ice thickness from See5.0 generally showed better performance than that derived using the existing methods. However, there are several uncertainty factors for sea ice thickness estimation using CryoSat-2 measurements (2014), including: 1) the error of range measurements from CryoSat-2, 2) the uncertainty of detection of leads, resulting in over- or under-estimation of SSHA, 3) the uncertainty of

means scattering horizon in the snow cover, and 4) the uncertainty of snow depth and the density of snow, ice, and sea water. Zygmuntowska et al. (2014) estimated the uncertainty of Arctic sea ice thickness and volume in terms of sea ice density and snow depth by using the Monte Carlo approach. They revealed that using snow loading (i.e., W99) produced higher uncertainty with respect to the estimation of sea ice thickness than using mean density. In the present study, we used the densities from Alexandrov et al. (2010) that do not have year-to-year variability. In order to more accurately estimate sea ice thickness, such changes should be carefully considered, which requires further examination. Ricker et al. (2014) analyzed random and systematic uncertainties of Arctic sea ice thickness from CryoSat-2 using the partial derivative of equation 1 based on the assumption of hydrostatic equilibrium. They showed that random uncertainty affects the estimation of sea ice thickness less than systematic uncertainty caused by the selection of a retracker threshold and the unknown penetration level of the signals on snow. To remove systematic uncertainty caused by the choice of a retracker threshold, Kurtz et al. (2014) used a waveform fitting approach to retrieve sea ice freeboard. Any of the above mentioned factors could result in uncertainty in this study. The lead detection models proposed in this study produced higher accuracy than the existing approaches for lead detection, which implies a possible reduction of the uncertainty caused by the second factor.

In order to examine the influence of snow penetration on the thickness estimation, we conducted a simple sensitivity analysis on snow penetration by testing different penetration ratios with the assumption that radar signals penetrate into the snow depth with the same rate over the entire Arctic region. The results showed that higher accuracy (i.e., lower RMSE) was achieved with increasing penetration depth ratios. Nevertheless, it is difficult to quantify how many centimeters of snow the K_u-band penetrates simply because the snow penetration depth highly depends on the spatiotemporal distribution of snow and whether it is dry or wet. In order to further enhance the sea ice freeboard and thickness produced in this study, snow penetration depth should be considered.

2.5 Conclusions

In this study, a novel machine learning-based lead detection approach was proposed to quantify Arctic sea ice freeboard and thickness from CryoSat-2 data. The estimated sea ice thickness was validated with AEM-bird data. Accurate lead detection is crucial in estimating LSSH, which is essential to retrieve the freeboard and thickness (Rose 2013; Farrell et al., 2009). The results showed that the proposed lead detection approach successfully estimated the sea ice thickness, compared to the existing methods. The overall accuracies by the proposed lead detection methods—decision trees

(See 5.0) and random forest—were 95.4% and 96.2%, respectively, which were higher than those produced using the existing methods.

A total of five parameters were used to detect leads, including SSD, stack skewness, PP, stack kurtosis, and backscatter sigma-0. Among the parameters, backscatter sigma-0, which prior methods had not considered, played a significant role in determining the threshold-based rules to distinguish leads from ice floes. The lead detection models developed by year or month (i.e., CM and CA) did not produce better performance than the combined model that used all samples for March and April from 2011–2014. This suggests that sea ice thickness in other months such as May or June could be retrieved when additional reference samples from the months were combined with the existing data. That way, a standard lead detection model can be proposed, which can be applied for any year and month. The results also showed that Arctic sea ice freeboard and thickness consistently decreased from 2011–2013, especially in the Canadian Archipelago region, but rebounded in 2014. Future research includes developing a machine learning-based lead detection model that can be applied to any year and month, and modeling snow depth penetration using CryoSat-2 data.

Chapter 3

3. Arctic lead detection using a waveform mixture algorithm from CryoSat-2 data

3.1 Introduction

Sea ice leads (hereafter referred to as “leads”), linearly elongated cracks in sea ice, are a common feature in the Arctic Ocean. Leads facilitate an amount of heat and moisture exchanges between the atmosphere and the ocean because of the temperature differences between them (Maykut, 1982; Perovich et al., 2011). Although leads occupy a small portion of the Arctic Ocean, there is much more heat transfer between the atmosphere and ocean through leads than sea ice (Maykut, 1978; Marcq and Weiss, 2012). Furthermore, Lüpkes et al. (2008) showed that a 1% change in sea ice concentration owing to an increase of lead fraction could increase near surface temperature up to a 3.5 K in the Arctic. Thus, the detection and monitoring of leads in the Arctic Ocean are crucial because they are closely related to the Arctic heat budget and the physical interaction between the atmospheric boundary layers and sea ice in the Arctic.

Satellite sensors have been the most efficient way to monitor leads in the entire Arctic region since the 1990s (Key et al., 1993; Lindsay and Rothrock, 1995; Miles and Barry, 1998). AVHRR and Defense Meteorological Satellite Program (DMSP) satellite visible and thermal images were used to detect leads in the early 1990s. Recently, MODIS IST product with 1km spatial resolution was used to detect leads to map pan-Arctic lead presence (Willmes and Heinemann, 2015; Willmes and Heinemann, 2016). They mitigated cloud interference using a fuzzy cloud artefact filter and investigated lead dynamics based on a comparison between pan-Arctic lead maps and the characteristics of the Arctic Ocean such as shear zones, bathymetry, and currents. While optical sensors have a finer spatial resolution, they are not pragmatic in the dark regions during polar nights (from December to February). In addition, leads are easily contaminated by clouds. Microwave instruments such as passive microwave sensors and altimeters have been used to detect leads and to produce lead fractions. Röhrs and Kaleschke (2012) utilized the polarization ratio of AMSR-E channels and retrieved daily thin ice concentration. With the help of the thin ice concentration, lead orientations and frequencies were derived using an image analysis technique (i.e., Hough transform) (Bröhan and Kaleschke, 2014). Air-borne and space-borne radar altimeters can detect leads as well. Zyguntowska et al. (2013) used Air-borne Synthetic Aperture and Interferometric Radar Altimeter System (ASIRAS), similar to CryoSat-2, to identify leads based on waveform characteristics and a Bayesian classifier. Zakharova et al. (2015) and Wernecke and Kaleschke (2015) utilized space-borne

altimeters such as Satellite with Argos and Altika (SARAL) and CryoSat-2 to identify leads, respectively. While Zakharova et al. (2015) applied simple thresholds to identify leads along with Satellite with Argos and Altika (SARAL/Altika) tracks and estimated regional lead fractions, Wernecke and Kaleschke (2015) optimized thresholds to detect leads and produced pan-Arctic lead fraction maps using CryoSat-2 with the analysis of lead width, and sea surface height.

Linear mixture analysis based on the assumption that the spectra measured by sensors for a pixel are a linear combination of the spectra for all components within the pixel (Keshava and Mustard, 2002) was first applied to the altimetry research field in the Polar Region by Chase and Hoyer (1990). They estimated sea ice type and concentration using linear mixture analysis based on Geosat waveforms. However, Geosat with a relatively small number of bins and coarser spatial resolution is not sufficient to detect small leads in the winter and spring seasons in the Arctic. In this study, we adopted the linear mixture analysis concept to waveforms from SARAL, CryoSat-2, to identify leads and produced monthly pan-Arctic lead fractions from January to May and October to December between 2011 and 2016. Waveform endmembers that are crucial to implement linear mixture analysis (Fig. 1). N-FINDR (N-finder) algorithm was used to select waveform endmembers from extracted waveforms by Decision tree (DT) from Lee et al. (2016), which can mitigate subjective selection of endmembers. The detected leads were visually evaluated with MODIS images (at 250 m resolution) and compared with other threshold based lead detection methods. The lead detection of waveform mixture analysis is not easily affected by the update of the CryoSat-2 baseline, which is novel and different from previous threshold based lead detection methods. The main objectives of this study are to 1) develop a novel lead detection method based on waveform mixture analysis, 2) identify recent pan-Arctic lead fractions.

3.2 Data

3.2.1 Sea ice edge data

EUMETSAT OSI SAF provides multiple sea ice products such as sea ice concentration, sea ice edge, sea ice type, sea ice emissivity, and sea ice drift. The sea ice edge product was developed using the polarization ratio of 19 GHz and 91 GHz, the spectral gradient ratio of 37 GHz and 19 GHz from SSMIS, and anisFMB from The Advanced Scatterometer (ASCAT) with Bayesian approach (Aaboe et al., 2016). In this study, monthly averaged sea ice edge data was used to mask out monthly lead fraction maps. The open ice cover in the sea ice edge product was regarded as an open ocean.

3.2.2 Monthly lead fraction maps

Lead fraction maps produced from previous studies (Röhrs and Kaleschke, 2012; Wernecke and Kaleschke, 2015; Willmes and Heinemann, 2016) were used to compare to the lead fraction maps generated using the proposed waveform mixture analysis in this study. Röhrs and Kaleschke (2012) produced daily thin ice concentration maps using AMSR-E data with a 6.25 km grid, which can detect leads that are wider (i.e., width) than 3 km. The daily thin ice concentration that was over 0.5 (i.e., 50%) was considered to be a lead and binary daily lead maps were averaged to properly compare other monthly lead fraction maps. A threshold optimization based lead detection method with the CryoSat-2 was used in Wernecke and Kaleschke (2015) and monthly lead fraction maps were calculated with the grids of 99.5 km. The thin ice concentration maps (Röhrs and Kaleschke, 2012) and the lead fraction maps using CryoSat-2 (Wernecke and Kaleschke, 2015) are available on their website (<http://icdc.cen.uni-hamburg.de/1/daten/cryosphere.html>). Willmes and Heinemann (2016) also produced daily lead maps over the entire Arctic Region, classifying land, cloud, sea ice, lead-artefact, and lead with the spatial resolution less than 2 km. The only lead class considers to make daily binary lead fraction maps and the sum of lead class is divided by days in a month (i.e., 28 or 30 or 31) to make monthly lead fractions maps. This data is available on their website (<http://dx.doi.org/10.1594/PANGAEA.854411>). In this study, we compared the monthly lead fraction maps from January to March 2011 as AMSR-E based lead fraction maps were only available until 2011.

3.3 Methods

3.3.1 Waveform mixture analysis

Spectral linear mixture analysis assumes that the spectra measured by sensors for a pixel is a linear combination of the spectra of all components within the pixel (Keshava and Mustard, 2002). This technique is widely used to resolve spectral mixture problems in hyperspectral image analysis (Foody and Cox, 1994; Dengsheng et al., 2003; Changshan, 2004; Iordache et al., 2011). Waveform mixture analysis is based on the concept of spectral linear mixture analysis. Since the waveform of altimetry within a footprint could be considered to be a mixture of leads and various types of sea ice, linear mixture analysis can be applied in this framework. In order to successfully implement waveform mixture analysis, the proper selection of an endmember is essential. The basic linear mixture model is defined as follows in equation 1.

$$Y_p = \sum_{k=1}^K a_{ik} E_k \quad (1)$$

where $Y_p = \{Y_1, Y_2, Y_3, \dots, Y_p\}$ represents waveform vectors and p means a bin in the waveform. a_{ik} is an abundance fraction, which provides proportions in terms of endmember. E_k is the endmember vectors. Equation 1 is constrained under $\sum_{k=1}^K a_{ik} = 1$ and $a_{ik} \geq 0$. In this study, we used MATLAB toolbox for linear unmixing with the interior point least square algorithm provided by Chouzenoux et al. (2014). This algorithm can handle huge data with inequality constraints, allowing reduced computational cost and high flexibility (Chouzenoux et al., 2014). While an endmember in remote sensing data represents a single pixel solely with a pure material, in this study, waveforms of CryoSat-2 L1b data were used as endmembers such as the waveform of pure lead and first-year ice (FYI) (Fig. 3.1). Chase and Holyer (1990) concerned by two problems with the application of linear mixture analysis to the waveform of altimeter data. First, the waveform within a footprint may not be linearly mixed between leads and sea ice. CryoSat-2 is more sensitive to the specular reflection of leads than the diffuse reflection of sea ice when both leads and sea ice exist within the same footprint, which implies the waveform may tend to be similar to the endmember of leads (Chase and Holyer, 1990). Since CryoSat-2 has large number of range bins, representing vertical resolution than the number of range bins from Geosat, could reduce the overestimation of leads. Secondly, the waveform of the altimeter (i.e., Geosat) is somewhat weighted on the centre of a footprint rather than representing an entire footprint. This could be an error source when applying linear mixture analysis to waveform data (Chase and Holyer, 1990). However, the CryoSat-2 L1b waveform is produced by averaging more than 200 weighted waveforms with various incidence angles, which can alleviate such a problem.

3.3.2 Endmember selection

The selection of endmembers is essential in the framework of waveform mixture analysis. We collected 48 CryoSat-2 files that traverse over the Arctic Ocean from January to May and from October to December 2011-2016 and extracted lead and ice waveforms by using the decision trees (DT) algorithm developed for lead detection by Lee et al. (2016). DT has proven to be very effective in various remote sensing classification tasks (Lu et al., 2014; Li et al., 2013; Kim et al., 2015; Torbick and Corbiere, 2015; Amani et al., 2017; Tadesse et al., 2017). The most representative waveforms (i.e., endmembers) is a key factor to implement waveform mixture analysis successfully. In order to prevent subjective selection of endmembers, a number of candidate endmembers were extracted DT algorithm and N-FINDR algorithm selected a pure lead and ice endmember. Therefore, the criterion of selection of endmembers is followed by DT and N-FINDR algorithm. Waveforms from March to April between 2011 and 2014 were compared to those from January to May, and October to December between 2011 and 2016 (not shown), resulting in little difference between them. This justified the use of the DT algorithm proposed by Lee et al. (2016) to extract waveform samples of leads and sea ice because the DT algorithm developed in March and April 2011-2014. The total number of sea ice and lead waveforms is 420,858 and 8,501, respectively. The N-FINDR uses an iterative simplex volume expansion by endmembers, assuming that the volume defined by a simplex with pure pixels is always greater than any other combination of pixels, and thus the algorithm has been widely used for automatically selecting representative endmembers (Winter, 1999; Zortea and Plaza, 2009; Erturk and plaza, 2015; Ji et al., 2015; Chi et al., 2016). The lead classification based on waveform mixture analysis was evaluated with 250 m MODIS images collected from March to May and in October. We used Earth view 250m reflective solar bands scaled integers in MOD02QKM product and adjust contrast to emphasize lead and sea ice in the images. It should be noted that since MODIS images with spatial resolution of 250 m were not available in January, February, November, and December due to polar nights, the evaluation with MODIS images and lead classification results based on CryoSat-2 could not be used. To secure the reliability of the comparison, the temporal difference between the MODIS images and CryoSat-2 data was always under 30 minutes.

The waveform mixture analysis model produces abundance data (i.e., lead and sea ice abundance) at along-track points with respect to each endmember of the leads and sea ice (Fig. 3.1). While the lead abundances are high on the leads, the ice abundances are low on the leads, vice versa (Fig. 3.1). Thresholds have to be determined to make a binary classification between leads and sea ice. Optimum thresholds to produce binary lead classification from lead and sea ice abundances were identified through an automated calibration. To implement the automated calibration, reference point data of leads and sea ice were determined by visual inspection of four MODIS images collected on 17 April 2014, 25 May 2015, 10 October 2015, and 27 March 2016. While the calibration was conducted using

half of the reference data randomly selected, the validation was performed using the remaining data. Threshold combinations from 0.2 to 0.9 with a step size of 0.01, for both lead and sea ice abundances, were tested and the one resulting in the highest accuracy was determined to be an optimum threshold combination.

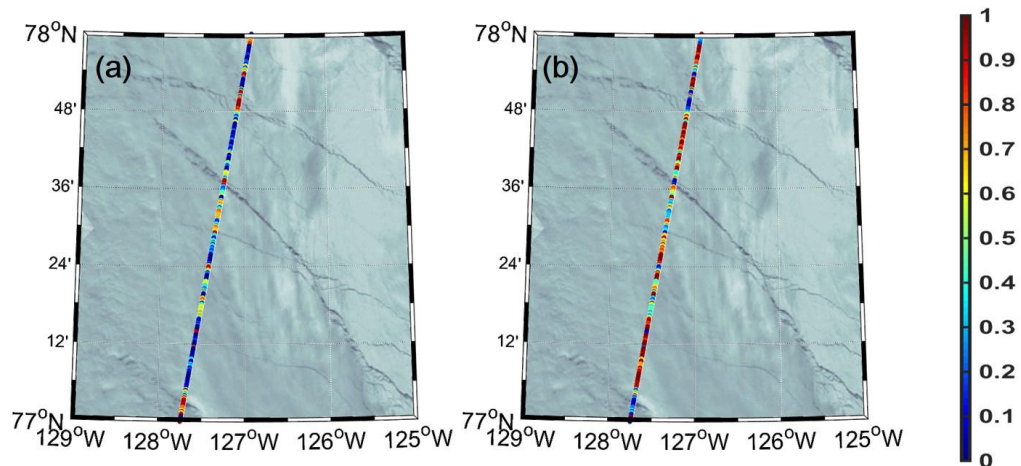


Figure 3. 1 Lead and ice abundance derived by waveform mixture analysis on 10 Oct. 2015. (a) Lead abundance, (b) Ice abundance. The colour bar expresses abundances from 0 to 1.

Lead detection results were evaluated using three accuracy metrics—producer’s accuracy, user’s accuracy, and overall accuracy (Tab. 3.1). Producer’s accuracy ($a/(a+c)$, lead classification accuracy), which is associated with omission errors, is calculated as the percentage of correctly classified pixels in terms of all reference samples for each class. User’s accuracy ($a/(a+b)$, lead classification accuracy), which is related to commission errors, is calculated as the fraction of correctly classified pixels with regards to the pixels classified to a class. Overall accuracy ($(a+d)/(a+b+c+d)$, lead classification) is calculated as the total number of correctly classified samples divided by the total number of validation sample data. The lead and ice references using MODIS is manually labelled along with CryoSat-2 tracks with naked eyes.

Table 3. 1 Error matrix for calculation of user’s, producer’s and overall accuracy in terms of lead and ice classification.

		MODIS references		
		Lead	Ice	Sum
CryoSat-2 based lead	Lead	a	b	(a+b)
	Ice	c	d	(c+d)
	Sum	(a+c)	(b+d)	(a+b+c+d)

A monthly lead fraction was derived by dividing the number of lead observations by the number of total observations within a 10 km grid in a month. We have compared lead fraction maps with the different spatial resolution (i.e., 10, 50, and 100 km) to decide proper spatial resolution. While 10 km lead fraction maps might be possible considering the number of CryoSat-2 observations in high latitudes, 10 km lead fractions in low latitudes may be insufficient to represent to lead fraction because the lead fraction is sensitive to change in the number of lead observations in the situation of the small number of CryoSat-2 observations. We divided into two sections in the Arctic Ocean, considering the number of CryoSat-2 observations. While spatial resolution of lead fraction is 10 km below 75°N, the spatial resolution of lead fraction is 50 km over 75°N since the number of CryoSat-2 observations rapidly decreased below 75°N. The partition of Arctic Ocean makes lower sensitivity in low latitudes. It is noted that while there are more than 30 CryoSat-2 observations in the 10 km grid around the centre of the Arctic, CryoSat-2 observations less than 5 are in the 10 km grid around the coast line of Arctic Ocean. This will be dealt with in the results section with more details.

3.3.3 Calculation of sensitivity in a 10x10 km grid

Since each grid has a different number of CryoSat-2 observations, a sensitivity analysis was conducted in terms of the number of observations by grid. Thirty (30) percent of the number of lead and ice observations in 10x10 km grids was repetitively permuted (i.e., the number of lead and ice observation in a grid randomly changed whenever iteration occurred) and the standard deviation of the resultant lead fractions through 50 iterations was calculated in grids. The higher the standard

deviation in a grid, the more sensitive the observed lead fraction is to the number of available observations. Since the number of CryoSat-2 observation around coast line is small (5-10), the thirty percent of the number of lead and ice observation is randomly changed, resulting in large variation of lead fraction in a grid. Meanwhile, the number of Cryosat-2 observation in high latitude is large (>30). The random change of the thirty percent of the number of lead and ice observation results in small variation of lead fraction in a grid. The sensitivities in terms of the calculation of monthly lead fraction maps depend on the number of CryoSat-2 observation. It should be noted that the standard deviation is zero when no lead observation is found, which means lead fraction is also zero. Sensitivities were calculated from January to April 2011 because these months were used to compare the lead fractions from the proposed waveform mixture analysis to those in the existing literature.

3.4 Results

3.4.1 Performance of lead classification

Exemplary results waveforms in the L1b SAR data are shown in Fig. 3.2. Such a waveform represents temporal distribution of reflected power when the radar pulses reach the surface, describing flat or rough surface. In this case, since the leading edge of each waveform starts from a different range bin, the beginning of the waveform was set at 1% of the maximum echo power (Figs. 3.2). For more detailed explanation about processes to develop L1b waveform data, refer to Salvatore (2013).

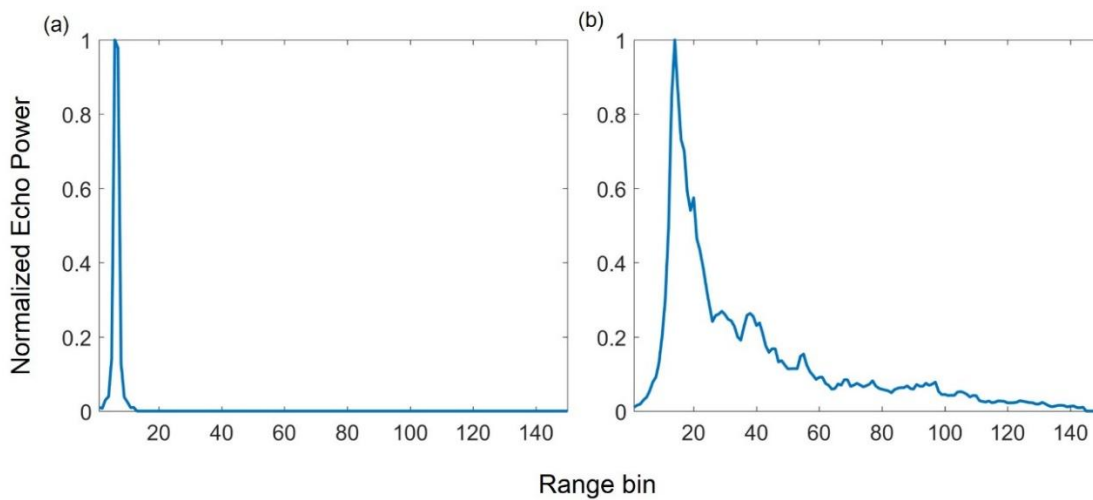


Figure 3. 2 Representative waveforms of (a) leads and (b) sea ice over the Arctic Ocean selected by N-FINDR algorithm during January to May and October to December between 2011 and 2016. Refer to the methods section for N-FINDR algorithm.

Fig. 3.2 shows representative waveforms of leads and sea ice extracted by the N-FINDR algorithm as endmembers. The waveform of leads is dominated by specular reflection, resulting in a narrow peak curve. The representative waveform of sea ice has a wider distribution due to its rough surface when compared to that of leads. Considering different types of sea ice such as young ice, FYI, and Multi-Year Ice (MYI), the representative waveform of sea ice is similar to that of FYI based on visual inspection (Zygmuntowska et al., 2013; Kurtz et al., 2014; Ricker et al., 2014; Wernecke and Kaleschke, 2015).

The optimum thresholds for the lead and sea ice abundances were determined to be 0.84 and 0.57 through the automated calibration, respectively. According to the thresholds, leads were identified with the conditions of lead abundance > 0.84 and sea ice abundance < 0.57 . Selected examples of lead detection results based on waveform mixture analysis are presented in Fig. 3.1 with threshold-based

lead detection results from the existing literature (Rose, 2013; Laxon et al., 2013; and Lee et al., 2016). Simple thresholding approaches based on two waveform parameters, PP and SSD were used in Rose (2013) and Laxon et al. (2013), respectively. It should be noted that since the existing methods were developed using parameters such as beam behaviour parameters and backscatter σ_0 extracted from baseline B data, rescaling was conducted on the parameters extracted from a newly updated baseline C data for reasonable comparison (Scagliola and Fornari, 2015).

Multiple lead classification methods based on CryoSat-2 data were evaluated by visual inspection with high resolution (250m) MODIS images. The waveform mixture analysis produced better results than previous lead detection methods using simple thresholding approaches such as Rose (2013) and Laxon et al. (2013) (Fig. 3.3). While the performance of waveform mixture analysis was comparable to the DT algorithm from Lee et al. (2016), waveform mixture analysis slightly over-estimated leads resulting in lower user's accuracy than user's accuracy for leads by DT (Fig. 3.4). This is inevitable result because waveforms used in waveform mixture analysis are basically extracted by DT from Lee et al. (2016).

Lead classification results should be assessed during all the months (i.e., January to May, and October to December) and years (i.e., 2011 to 2016) using MODIS images to thoroughly evaluate the proposed waveform-based algorithm for lead detection. However, lead classification results in January, February, November, and December were not assessed using MODIS images due to polar nights. Thus, the lead classification results in these months could possibly have uncertainties.

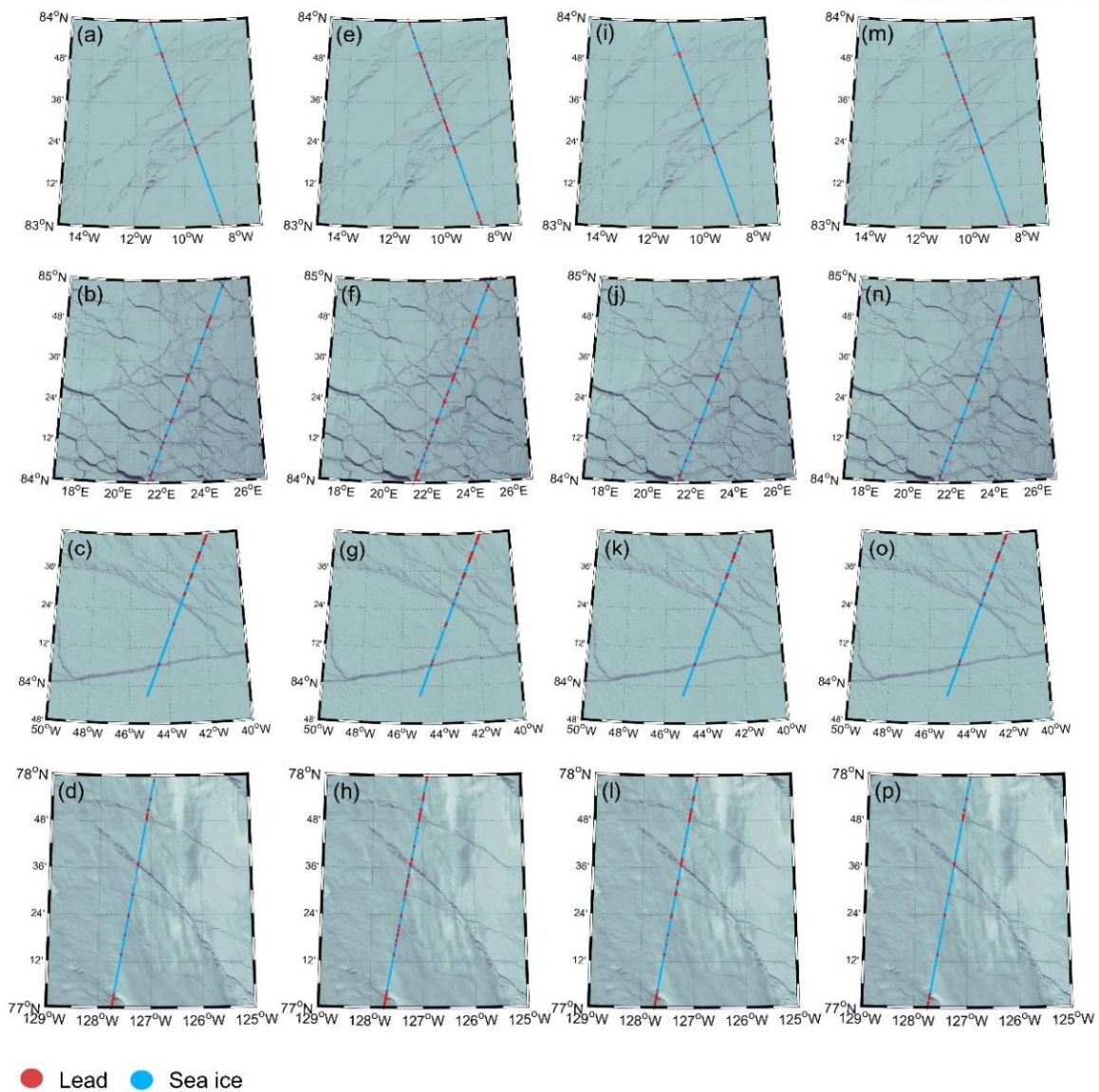


Figure 3. 3 Visual comparison of lead classifications: (a) – (d) lead classifications based on Rose (2013), (e) – (h) lead classifications based on Laxon et al. (2013), (i) – (l) lead classifications based on decision trees from Lee et al. (2016), and (m) – (p) lead classifications based on the proposed waveform mixture analysis. The MODIS data were collected in March (a, e, i, and m), April (b, f, j, and n), May (c, g, k, and o), and October (d, h, l, and p).

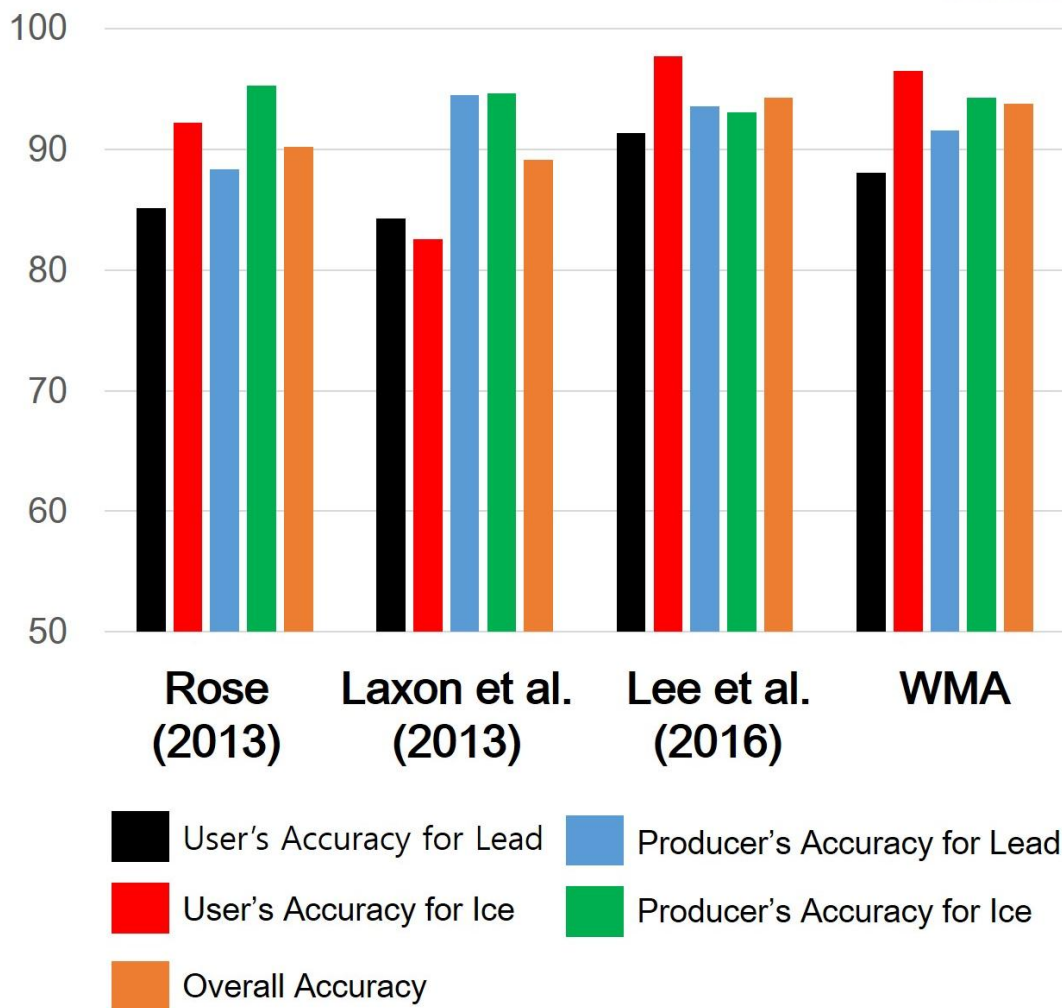


Figure 3. 4 Accuracy assessment results for lead detection by method—three existing methods and the proposed waveform mixture algorithm (WMA).

3.4.2 Spatiotemporal distribution of lead fraction maps

The monthly lead fraction maps in January to May, and October to December from 2011 to 2016 are shown in Figs. 3.5 and 3.6. The areas around the coast line of the Arctic Ocean clearly show higher lead fraction due to the shear zone (i.e., an area of deformed sea ice along the coast, Serreze and Barry, 2005) and outflow of sea ice. In particular, high lead fraction was found around Beaufort Sea during the spring season (MAM) because of the Beaufort Gyre, a wind-driven ocean current. It is widely known that the Chuckchi Sea is the main strait that warm Pacific water flows through into the Arctic (Woodgate et al., 2006; Woodgate et al., 2010). However, the lead fraction around the Chuckchi Sea was lower than the lead fraction around Beaufort Sea in January to April (i.e., winter season) 2011 and 2016, excluding 2015. While the lead fraction decreases from October to March (i.e., freezing season) with the minimum in March, the lead fraction starts to increase from April. This

indicates an increasing lead fraction, which corresponds to the seasonal cycle of sea ice thickness. However, the lead fraction around the Beaufort Sea decreases in March and April of 2013 and 2016 (Figs. 3.5 and 3.6). The lead fraction in the spring season in 2013 was particularly high possibly due to the sea ice extent minimum in September 2012, which required a relatively long period of time to freeze up in the spring of 2013 (Figs 3.5 and 3.6). December to January is usually considered as a freezing season. Nevertheless, the lead fraction around the central Arctic increased in January 2016. This result corresponds to the findings of Kim et al. (2017) and Ricker et al. (2017).

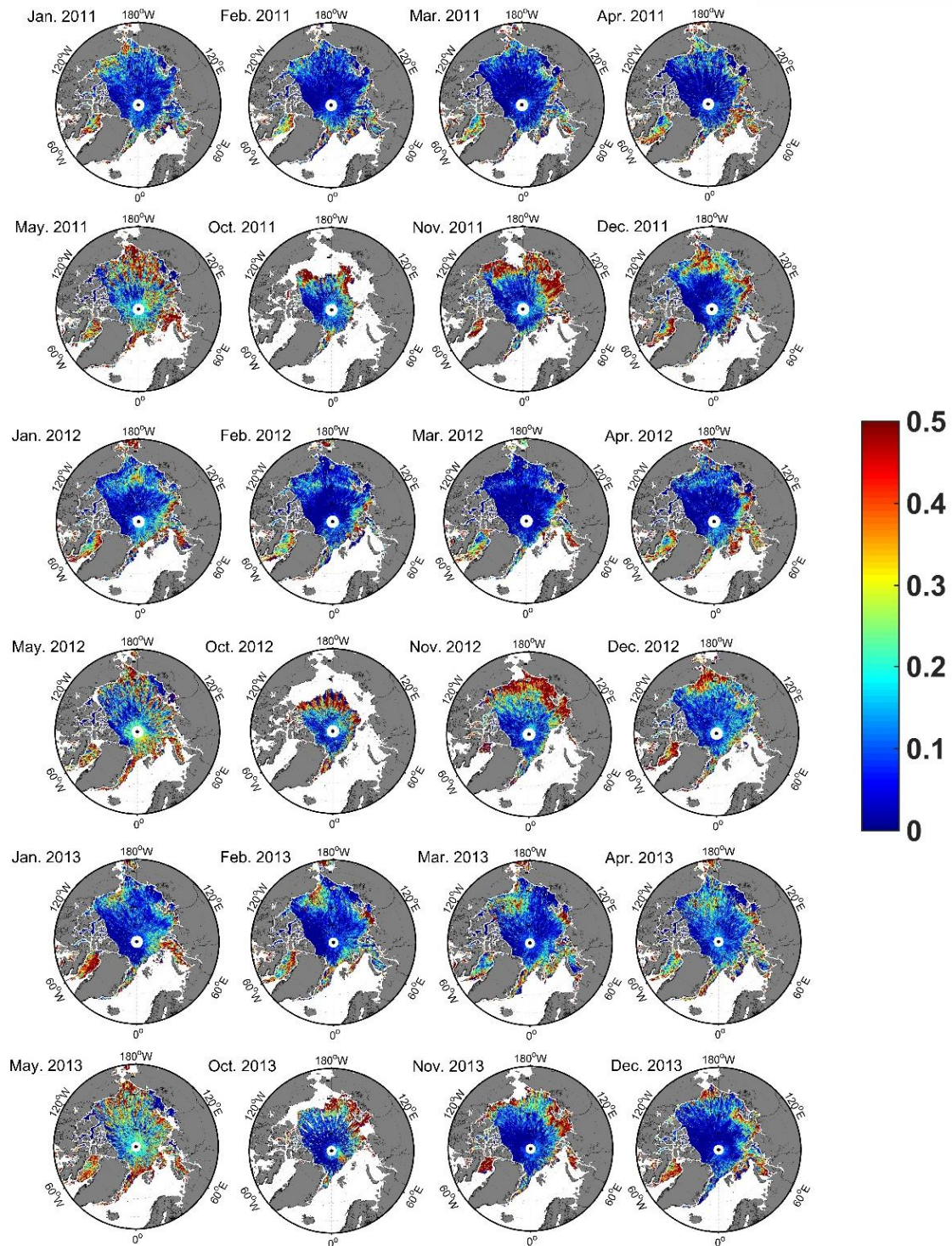


Figure 3. 5 Monthly lead fraction maps based on waveform mixture analysis in January to May, October to December between 2011 and 2013. The range of the colour bar was set from 0 to 0.5 to emphasize lower values.

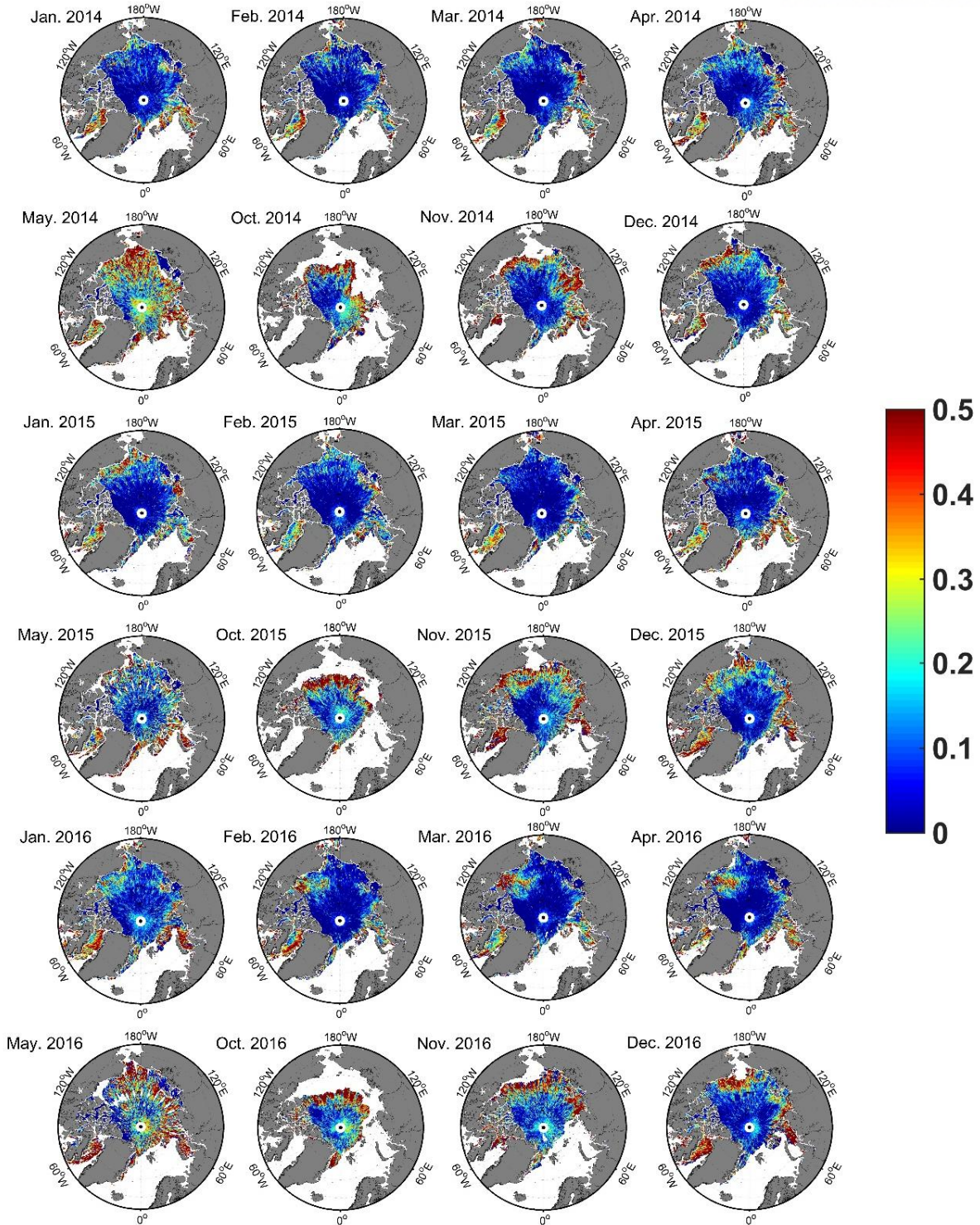
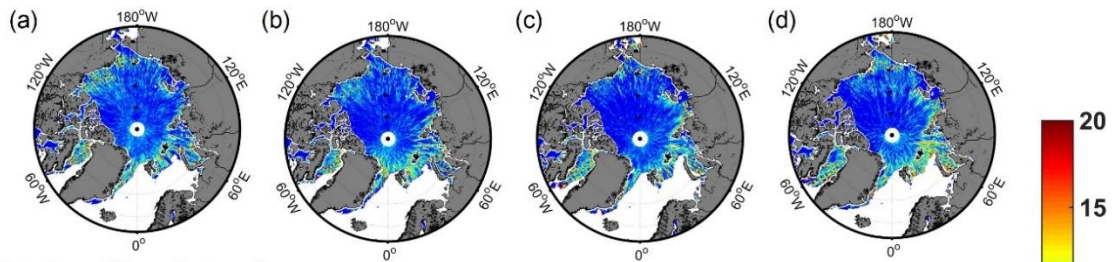


Figure 3. 6 Monthly lead fraction maps based on waveform mixture analysis in January to May, October to December between 2014 and 2016. The range of the colour bar was set from 0 to 0.5 to emphasize lower values.

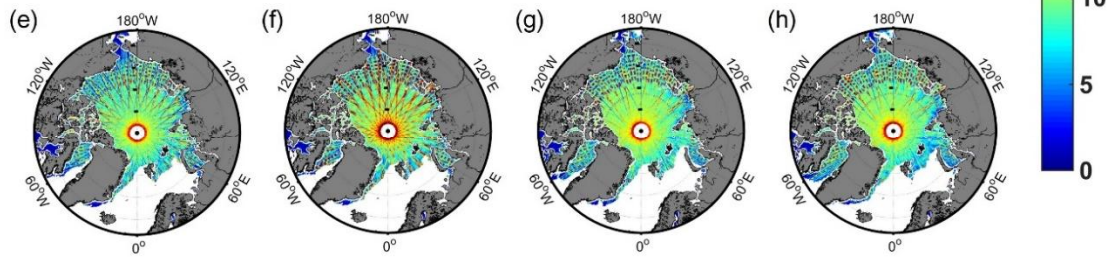
3.4.3 Grid sensitive analysis in 10x10 km

As mentioned in section 3.3.3, the number of CryoSat-2 observation decreases from the North Pole toward the coast line of Arctic Ocean. This results in an increase in sensitivities when calculating monthly lead fraction around the coast line of Arctic Ocean based on the small number of CryoSat-2 observations. The number of lead and ice observations is shown in Fig. 3.7a-h. While there are a few lead observations around coast line, a large number of ice observations was found in the central Arctic. The high standard deviation values around the coast line of the Arctic Ocean zone imply that the reliability of lead fractions was low, while the relatively large number of CryoSat-2 observations around the North Pole produced low standard deviation indicating less sensitivity (Fig. 3.7i-l). There was spatial difference of sensitivity by month (i.e., January to April) because of the different number of lead observations. Especially, since there was no lead observation in the East Siberian coast and Eastern Laptev Sea, the sensitivity (i.e., standard deviation) was also zero (Fig. 3.7c and d). It should be noted that the corresponding lead fraction might not represent actual lead fraction in a 10 x 10 km grid. This is a drawback when calculating monthly lead fraction maps with satellite altimeters.

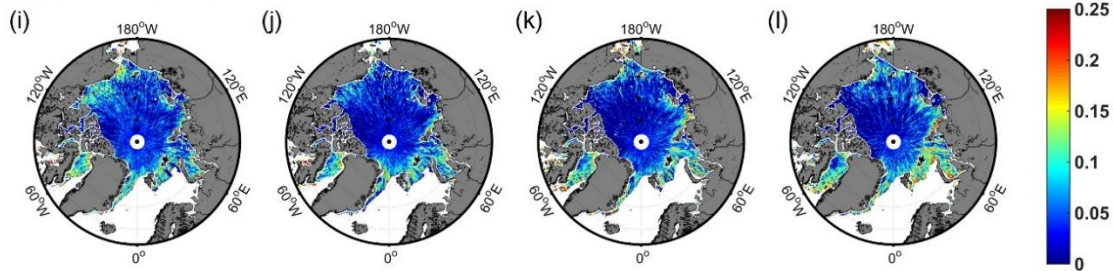
Number of lead observations



Number of ice observations



Standard deviation



January 2011

February 2011

March 2011

April 2011

Figure 3. 7 (a-d) the number of lead observations, (e-h) the number of ice observations, (i-l) the standard deviation of the results based on the sensitivity analysis of lead fraction from January to April 2011.

3.5 Discussion

3.5.1 Comparison of lead classification methods

While all classification methods produced high producer's accuracy for the ice class exceeding 93 %, the approaches from Lee et al. (2016) and Laxon et al. (2013) resulted in a bit higher producer's accuracy for leads than the other methods (Fig. 3.4). Although Laxon et al. (2013) produced the highest producer's accuracy for leads (i.e., 94.5 %), which means that this method robustly detected leads, the user's accuracy for ice was the lowest, suggesting a huge number of false alarms for leads on the ice. Overestimation of leads may increase sea surface height anomaly (SSHA), which will lead to the underestimation of sea ice freeboard (Lee et al., 2016).

Since the overall accuracy metrics of the proposed waveform mixture analysis approach was comparable to those of the existing methods, especially DT, the waveform-based method can be used for estimating SSHA. Threshold-based lead detection methods have to be re-scaled whenever baseline data are updated. For example, beam behaviour parameters and backscatter sigma-0 changed slightly between when baseline B and baseline C data were used. Thus, thresholds must also be updated in order to appropriately identify leads using the threshold-based methods. However, waveform mixture analysis is free from the change of baseline data because waveforms can still be used to detect leads using updated baseline data. This is the strong point of waveform mixture analysis when compared to the existing methods.

The use of waveform mixture analysis might not work well to detect leads in cases of refreezing leads. In Figs. 3c, g, k, and o, the dark area in the MODIS scenes around the latitude of 84.26°N and longitude of 43°W was determined to be a lead class with visual inspection of the images and waveforms. Rose (2013) classified this region as ice. Laxon et al. (2013) and waveform mixture analysis detected one lead in that region. In fact, since the leads were refrozen, the waveforms in that region were more similar to the typical FYI waveform. In the context of waveform mixture analysis, this region could be classified as ice. Additionally, rough lead by strong wind tends to be classified as ice. Therefore, in order to more accurately detect leads, a surface elevation anomaly is needed as well as beam behaviour parameters, backscatter sigma-0, and waveform mixture analysis because the surface elevation anomaly on refreezing leads would be low like other leads.

3.5.2 Comparison to other lead fraction maps

Four monthly lead fraction maps (Röhrs and Kaleschke, 2012; Wernecke and Kaleschke, 2015; Willmes and Heinemann, 2016) were compared to evaluate the pros and cons of each method used to produce the maps (Fig. 3.8). Basically, all four methods represent the spatiotemporal pattern of leads well for the freezing season from January to March. Scene-based lead fraction maps (i.e., AMSR-E in Figs. 3.9a, b and c, and MODIS in Figs. 3.8d, e, and f) and altimeter-based lead fraction maps (i.e.,

CryoSat-2 in Figs. 3.8g to l) have fundamentally different spatial characteristics as AMSR-E and MODIS are sensitive to different surface features. Scene-based lead fraction maps better represent the linear feature of leads and coastal polynya than altimeter-based lead fraction maps. Since the AMSR-E-based approach only detects relatively large (~ 3 km) leads, lead fractions are generally lower than in the fraction maps using the other approaches. While altimeter-based lead fractions in January 2011 (Figs. 3.8g and j) in the Chuckchi Sea were high, scene-based lead fractions (Figs. 3.8a to f) were low in January 2011. There are deformed and fragmented sea ices in the Chukchi Sea, which is different from the general lead shape. Altimeter-based lead detection methods identified leads between deformed and fragmented sea ices, generating a higher lead fraction in the Chukchi Sea in January 2011 (Figs. 3.8g and j). However, scene-based lead fraction methods did not detect leads in the Chukchi Sea well, resulting in a lower lead fraction. The MODIS-based lead detection method that used IST did not detect leads in the Chukchi Sea (Figs. 3.8d, e, and f). In the AMSR-E images, sea ice signals were dominant in the footprint around the Chukchi Sea and cracks between deformed and fragmented sea ices were identified as ice.

Altimeter-based monthly fraction maps might be insufficient to represent monthly lead fractions in the coast line of the Arctic Ocean due to the limited number of CryoSat-2 observations in a month. Nonetheless, altimeter-based lead fraction maps well documented the overall spatial distribution of leads, in particular, high lead fractions in the shear zone. Wernecke and Kaleschke (2015) used a random cross validation technique to derive optimum thresholds based on ground references (i.e., MODIS images). They identified leads conservatively to reduce false classifications. The classification results strongly depend on ground reference data. Since relatively high resolution (250m) MODIS images were used to construct reference data in this study, the waveform mixture analysis was able to identify small leads through the calibration process of the abundance data (Fig. 3.3). Although the proposed waveform mixture analysis produced lead fraction maps with a higher spatial resolution than those in Wernecke and Kaleschke (2015), the lead fractions around the coast line of the Arctic Ocean from Wernecke and Kaleschke (2015) appeared to have less uncertainty. This is because of the larger number of lead observations in a much coarser grid than that from our results. The grid sensitivity analysis should be considered when interpreting the lead fraction maps around the coast line of the Arctic Ocean derived by the proposed waveform mixture analysis.

The choice of monthly lead fraction maps depends on the user's interest. Scene-based lead fraction maps better represent coastal polynya and the intrinsic form of leads (Röhrs and Kaleschke, 2012; Willmes and Heinemann, 2016). CryoSat-2 based lead fraction maps might not represent the linear shape of typical leads well like cracks which includes deformed and fragmented sea ices that are not in linear form. This is also a way to exchange heat and momentum transfer between the atmosphere and ocean, which can be detected as leads.

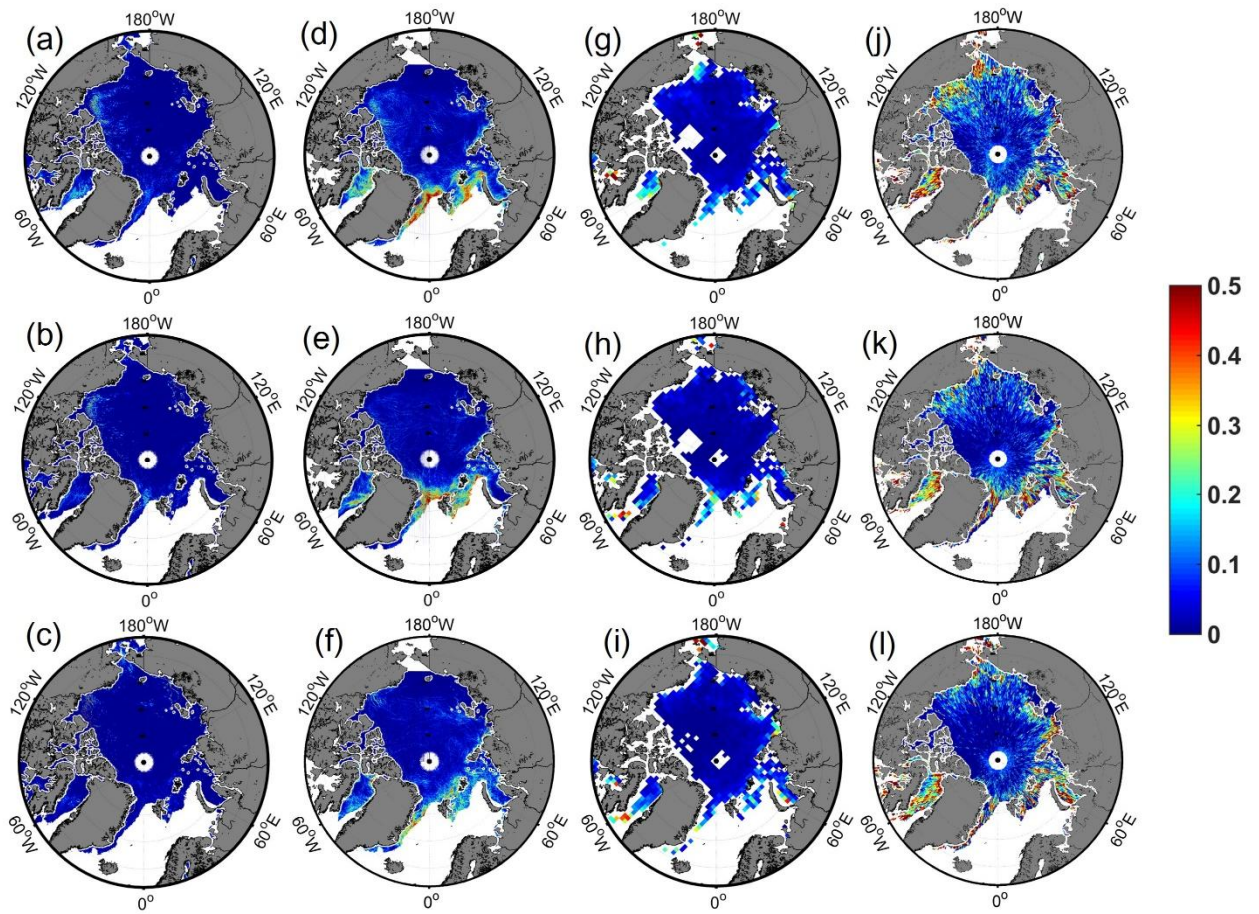


Figure 3. 8 Comparison to other lead fraction maps in January to March 2011. (a-c) Monthly mean thin ice concentration maps using AMSR-E from Röhrs and Kaleschke (2011). (d-f) Monthly mean lead fraction maps using MODIS from Willmes and Heinemann (2015). (g-i) Monthly lead fraction maps using CryoSat-2 from Wernecke and Kaleschke (2015). (j-l) Monthly lead fraction maps based on waveform mixture analysis using Cryosat-2 in this study.

3.5.3 Lead dynamics

The features of the Arctic sea ice dynamics are driven by wind and, to a lesser degree, ocean currents (Kwok and Untersteiner, 2011). The Arctic Ocean circulations have contributed to the change in the state of sea ice. The lead fraction in northwestern Greenland in Figs. 5 and 6 is low because of the convergence of sea ice by two major circulations, which was clearly shown in Kwok (2015). Kwok et al. (2013) revealed that the currents speed of Beaufort Gyre and Transpolar Drift increased from the years of 1982 to 2009 and this makes the fraction of multi-year ice decrease. However, the increasing lead fraction from the years of 2011 to 2016 in this study was not seen due to the high inter-annual variability of lead fraction, particularly in the spring season (Fig. 3.9). High uncertainties in the marginal sea ice zone might result in not catching the increasing trend of Arctic lead fraction shown in the literature. In order to properly compare the Arctic current circulations and lead fraction, long-term lead fraction data are needed.

The inter-annual variability of lead fraction is related to atmospheric anomalous phenomena. In a situation of large inter-annual variability of lead fraction in spring season from 2011 to 2016, the lead fraction in spring season decreased from 2013 to 2014, especially, around Beaufort Sea (Figs. 3.5, 3.6, and 3.9). The increase and decrease of lead fraction is linked to the change in sea ice thickness. The decrease of lead fraction in March and April from 2013 to 2014 corresponds to the increase of sea ice thickness in March and April from 2013 to 2014 (Tilling et al., 2015; Lee et al., 2016). Tilling et al. (2015) assessed the main cause of increase of sea ice thickness to be an anomalous cool summer in 2013. While November to March is considered to be the freezing season, the lead fraction increased in the central Arctic between December 2015 and January 2016 (Fig. 3.7). Kim et al. (2017) and Ricker et al. (2017) explained a plausible reason for the reduction in sea ice growth. Warm and moist air from the Atlantic Ocean strongly intruded into the Arctic, weakening sea ice growth. Furthermore, the high lead fraction in the Beaufort Sea in February to April 2016 was attributable to the high ice drift speed (Ricker et al., 2017).

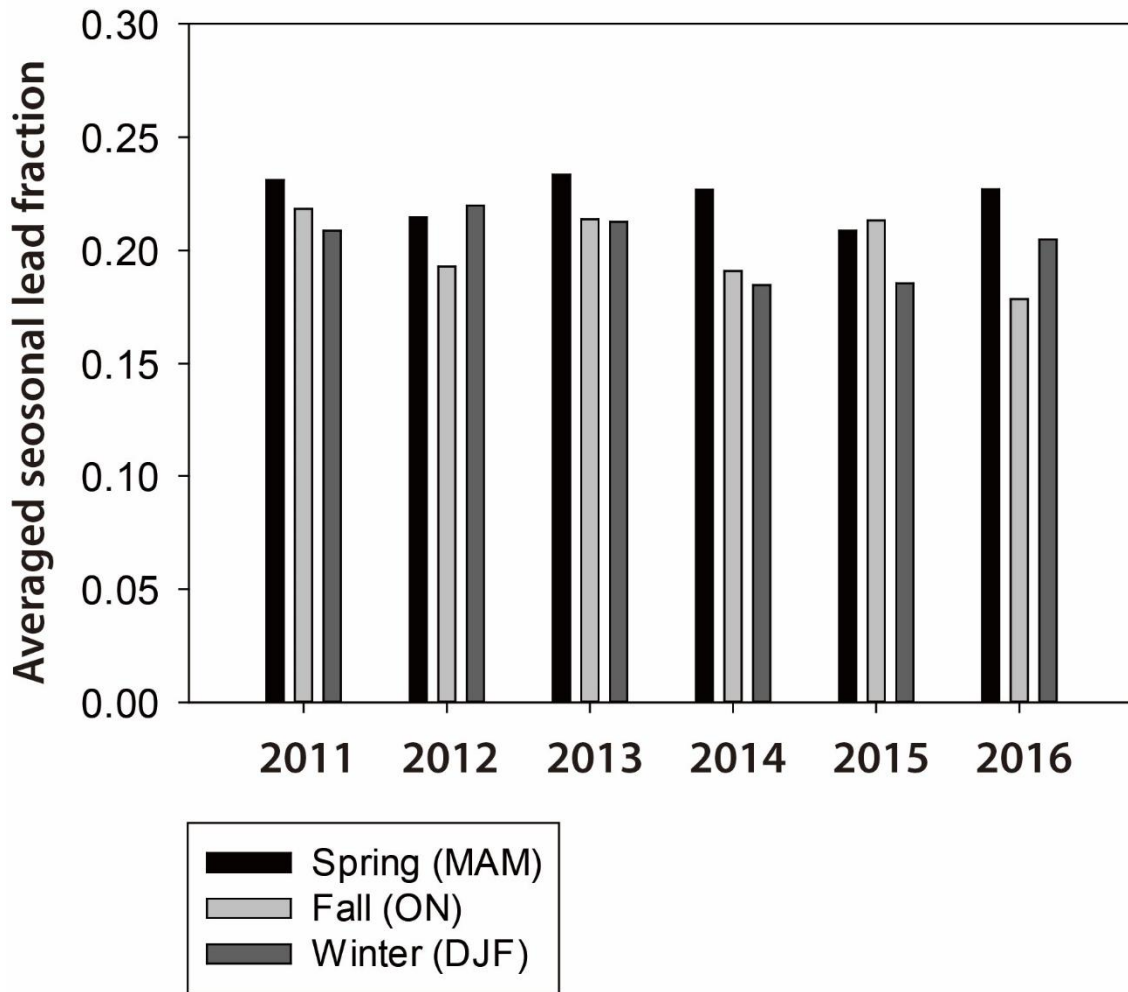


Figure 3. 9 Averaged seasonal lead fraction in spring (MAM), fall (ON), and winter (DJF) between 2011 and 2016. The lead fraction from June to September was not available because leads were hard to distinguish from melt ponds using CryoSat-2 in the summer season.

3.5.4 Novelty and limitations

In this study, we developed an alternative lead detection method (i.e., waveform mixture analysis) using CryoSat-2 L1b data, which can overcome the drawbacks of previous threshold based lead detection methods. Regardless of an update in CryoSat-2 baseline data, the proposed waveform mixture analysis can consistently identify leads without rescaling parameters such as beam behaviour parameters, pulse peakiness, and backscatter sigma-0. Such parameters must be rescaled to implement threshold based lead detection methods when using updated CryoSat-2 baseline data. In addition, the proposed waveform mixture analysis outperformed the existing simple thresholding-based methods (Rose, 2013; Laxon et al., 2013), and was comparable to the machine learning-based thresholding method (Lee et al., 2016). In addition, this study showed the high inter-annual variability of Pan-Arctic lead fractions in recent years (i.e., 2011-2016), which implies that recent sea ice state becomes more vulnerable to atmospheric and oceanic forcing.

On the other hand, the waveform mixture analysis depends on the quality of the endmembers. Although the use of the N-FINDR algorithm decreased the subjective selection of endmembers, waveform samples of leads and sea ice derived by DT algorithm from Lee et al. (2016) may introduce uncertainty because the algorithm was validated for March and April from 2011 to 2014. The spatial resolution of monthly lead fraction maps improved up to 10km, showing detailed spatial distribution of leads in the Arctic in high latitudes. For example, some regions have various lead fractions with 10 km spatial resolution but various lead fraction in some regions cannot be described with 100 km spatial resolution because lead fraction are averaged, resulting in blur spatial patterns.

3.6 Conclusions

The waveform mixture analysis was proposed to detect leads with CryoSat-2 L1b data. The lead and sea ice waveforms were considered as endmembers that are essential to implement waveform mixture analysis. The endmembers (i.e., representative waveforms of leads and sea ice) were extracted by the N-FINDR algorithm among numerous waveforms (i.e., 420,858 waveforms of sea ice and 8,501 waveforms of leads). The thresholds to make a binary classification were determined by calibrating lead and sea ice abundances with reference data extracted from high resolution (250m) MODIS images. The results show that the proposed approach robustly classified leads with better performance than previous simple thresholding approaches for lead detection (Rose 2013; Laxon et al., 2013). Furthermore, the lead detection of waveform mixture analysis was comparable to the decision tree based lead detection method (Lee et al., 2016), suggesting a sea ice freeboard can be retrieved with the robust lead detection method using waveform mixture analysis. Monthly lead fraction maps were produced using the proposed waveform mixture approach, showing clear inter-annual variability. Scene-based lead fraction maps have different characteristics from altimeter-based lead fraction maps due to different sensors, algorithms, and spatial resolutions but showed similar spatial distribution. The results of the lead fraction maps are consistent with the findings of recent studies (Tilling et al., 2015; Ricker et al., 2017; Kim et al., 2017). The lead dynamics based on monthly lead fraction maps were examined with the Arctic Atmospheric and oceanic circulations.

Unlike thresholds based lead detection methods, the waveform mixture analysis is free from the update of baseline version of CryoSat-2 data, which will be useful for future altimeter missions. The recent strong inter-annual variability of Arctic sea ice conditions was found. In this context, this waveform mixture analysis can be used to consistently produce monthly lead fraction maps during the extended CryoSat-2 mission for monitoring Arctic sea ice.

Chapter 4

4. Anomalous slow sea ice recovery in fall and winter 2016 by extreme warming event in mid-latitudes

4.1 Introduction

Polar amplification is a phenomenon in which the surface air temperatures in high latitudes more increase than averaged temperatures in the entire Earth in terms of in the perspective of climate change (Serreze et al., 2009; Park et al., 2015). Recently, the frequency of warming events in the Arctic is increasing based on buoy and reanalysis data (Graham et al., 2017). Satellite observations have revealed that Arctic sea ice extent is continuously diminished since end of 1970 as temperatures in the Arctic have increased (Cavalieri et al., 2003; Cavalieri and Parkinson, 2012). Arctic sea ice minimum anomaly phenomenon began to stand out from 2002. (Serreze et al., 2003). Since 2002, sea ice extent in September highlighted by breaking sea ice extent minimum record. Arctic sea ice extent in September 2002 was lowest since 1978 due to anomalous southerly warm winds and ice divergence by consistent low pressure and high temperatures (Serreze et al., 2003). The sea ice anomaly continue in 2007 and 2012 as well. The higher Sea surface temperature (SST) and the fraction of open water likely contributed to sea ice extent anomaly in September 2007 (Comiso et al., 2008; Parkinson and Comiso, 2013). A considerable attention focused on sea ice extent in September 2012 owing to the historical minimum extent, $3.4 \times 10^6 \text{ km}^2$ (Parkinson and Comiso, 2013). Preconditioned sea ice and a strong storm in the central Arctic in August 2012 were major role in declining sea ice (Parkinson and Comiso, 2013). The warming condition by southerly warm winds is a primary contributor to these sea ice anomalies rather than climate modes such as Arctic Oscillation (AO) and North Atlantic Oscillation (NAO).

Arctic sea ice in winter season has experienced anomaly phenomena as well. Strong winds bring humid and warm air from the Atlantic Ocean to the Arctic in January and February 2005, 2006 (Comiso, 2006; Sorteberg and Walsh, 2008). Especially, a strong cyclonic-storm contributed to ice anomaly around Barents, Kara Seas in winter 2015-2016 (Cullather et al., 2016; Boisvert et al., 2016; Kim et al., 2017). The sea ice anomaly in winter season considerably delay ice growth, accelerating melt following spring and summer season (Comiso et al., 2008). For example, sea ice extent in January, February and April 2017 also record minimum extent, which is apparently influenced by sea ice minimum anomaly in fall and winter 2016. The study of sea ice anomaly in fall and winter season needs to be focused to increase predictability of sea ice in spring season and to understand the nature of sea ice anomaly phenomenon in fall and winter season.

The objective of this study is to investigate Arctic sea ice anomaly in November 2016, which is strongly connected to extreme warming in mid-latitudes and atmospheric circulation from August to October 2016. Sea ice concentration and CryoSat-2-derived sea ice thickness are used to represent sea ice state. Atmospheric circulation is examined by Modern-Era Retrospective Analysis for Research Applications version 2 (MERRA-2) atmospheric reanalysis. SST data was also used to identify warming ocean in the Pacific and Atlantic.

4.2 Data and Methods

4.2.1 Sea ice concentration and thickness

EUMETSAT OSISAF provides sea ice concentration data in 10km spatial resolution. The brightness temperatures (T_b) of SSM/I 19V, 37V, and 37H were used to develop sea ice concentration as input data (Tonboe et al., 2016). The T_b was corrected due to wind roughening and air temperature over open water and water vapor in the atmosphere before calculating sea ice concentration. Sea ice concentration anomaly is calculated to represent the rapid change in sea ice in August to November 2016 for a base period of 2007-2016.

Sea ice thickness plays significant role in controlling heat and momentum exchanges between ocean and atmosphere, thermohaline circulation, and freshwater discharge in the Arctic environment (Toole et al., 2010; Nicolaus et al., 2012; Meier et al., 2014). The sea ice thickness better indicate the surface distribution, where sea ice concentration is higher than 90%, especially, in the center of Arctic. The retrieval algorithm for sea ice thickness in this study is same as Lee et al. (2016) but lead detection method is different. A new lead detection method proposed by Lee et al. (2017) was used, which is waveform mixture algorithm developed on the basis of baseline C data to minimize uncertainties. However, a correction of lower propagation speed in the snow pack proposed by Kwok et al. (2014) was not applied in Lee et al. (2016). The sea ice thickness from Lee et al. (2016) applied by lower propagation correction was used in this study. Furthermore, since lead detection methods from Lee et al. (2016) were developed based on baseline B data, the thresholds for lead detection by machine learning could introduce uncertainties for application to the baseline C data. It should be noted that sea ice thickness in melt season (i.e., May to September) is not available because it is difficult to distinguish leads from melt ponds on the sea ice. The sea ice thickness anomaly in November for a base period of 2011 – 2016 to describe surface variation particularly in the center of Arctic.

4.2.2 MERRA-2 reanalysis and SST data

MERRA-2 provides various atmospheric variables from 1980, which is improvement version of MERRA (Molod et al., 2015; Bosilovich et al., 2016). Although reanalysis data is vulnerable to the

discontinuities by changing observation systems, it is very useful to represent scarce and heterogeneous regions (Lindsay et al., 2014). I specifically used 2-m air temperature, sea level pressure, and 10-m wind, describing atmospheric spatial patterns in the Arctic. The anomaly is calculated based on the period from 1980 to 2016.

I used National Oceanic and Atmospheric Administration (NOAA) Optimum Interpolation (OI) monthly SST developed using in-situ and satellite data, identifying the intrusion of warm SST in Pacific and Atlantic sector with the anomaly period of 1982 to 2016.

4.3 Results

4.3.1 Anomalous warming event in mid-latitudes and Arctic

As with arctic amplification, average temperature in mid-latitudes gradually increased (Doscher et al., 2014). It is reported that extreme warming event occurred in 2016 (NOAA, 2017, Thirumalai et al., 2017). Fig. 4.1a shows record breaking warming in mid-latitudes between 40 - 70°N in August and September 2016, which is higher about 91.3 % and 64 % than global average, respectively. Meanwhile, the average temperature between 40 - 70°N did not rise sequentially but rather the average temperature dramatically decreased in August and September due to Eurasian cooling. It is revealed that the loss of sea ice is largely related to the Eurasian cold winter (Cohen et al., 2012; Mori et al., 2014; Tang et al., 2013). The highest average temperature in the Arctic region (i.e., 70 - 90°N) in October and November 2016 is recorded, which is higher about 92 % and 140 % than global average (Fig. 4.1b). The high temperature of mid-latitudes and Arctic in August to November promotes ice-albedo feedback in the Arctic, slowing the growth of sea ice in fall. The lowest sea ice extent in November 2016 is eventually recorded (Fig. 4.1c).

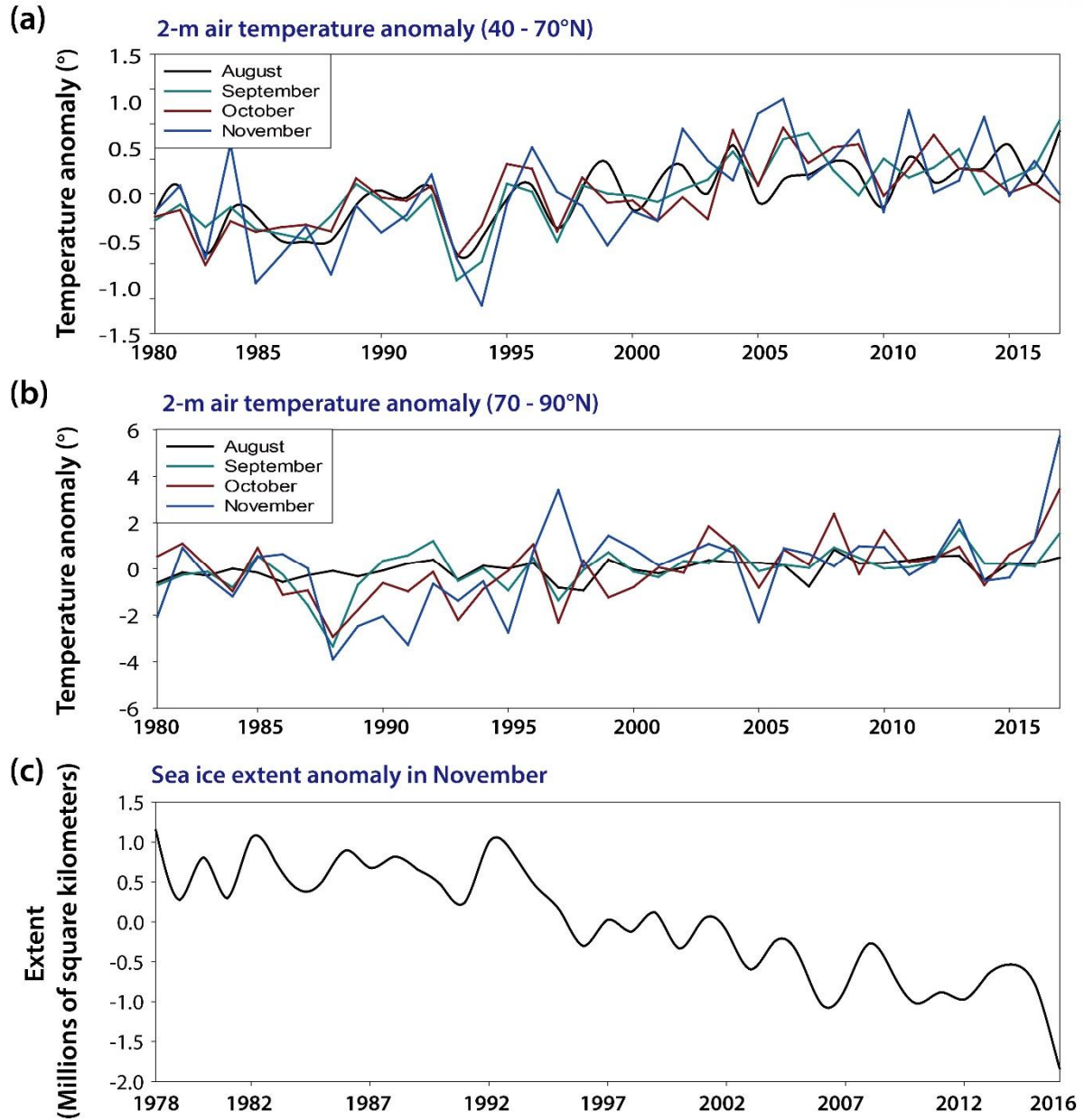


Figure 4. 1 2-m air temperature anomaly from 1980 to 2016 in August to November in different area: (a) mid-latitudes, (b) Arctic region. (c) Sea ice extent anomaly in November from 1979 to 2016.

4.3.2 Sea ice minimum extent in November 2016

There is a significant drop of sea ice extent in November 2016 (Fig. 4.1c), which is negative 16.8 % of whole November from 1978. In the spatial pattern of sea ice in November 2016, Kara, Barents, and East Siberia Sea showed a negative anomalies, which largely contributes to the minimum sea extent in November 2016 (Fig. 4.2d and h).

A strong low pressure (<996hPa) located on Central Arctic and high pressure around west Eurasia moved warm air to the Arctic with Southerly winds in August 2016 (Fig. 4.3a). The warm air is easier to be moved to the North due to the low fraction of sea ice in Kara and Barents Sea. In September 2016, the strong low pressure is moved to Beaufort Sea and the high pressure in Eurasia continental has grown (Fig. 4.3b). Due to such high and low pressure system position, warm air from sub-Arctic continuously moved to the Arctic. The southerly winds in August and September 2016 by high and low pressure system position might be the reason to make significant negative anomaly in the central Arctic in September 2016 (Fig. 4.2b, 4.3a and b). The substantial negative anomaly of sea ice in the central Arctic in September 2016 is more obvious than sea ice anomaly in September 2012 that is historically lower sea ice extent.

The constant southerly warm winds in August and September might greatly contribute to record high air temperature in the Arctic region (i.e., 70 - 90°N) in October 2016 (Fig 4.1b). While the negative anomalies in central Arctic is recovered, there still remains a negative anomaly in the central Arctic in October 2016 (Fig. 4.2c). The low pressure in the central Arctic in August and September moves toward to Pacific region with more intensity and the high pressure in Eurasian continent is further extended, promoting the inflow of warming air into the Arctic in October 2016 (Fig. 4.3a to c). Although the warm anomaly is dominant around Northeast of Greenland, the positive anomaly of sea ice concentration is observed, which is possibly connected to the convergence of sea ice by ice drift. Eurasian cooling begins in October 2016, dropping average temperature in mid-latitudes (Fig. 4.1a and Fig. 4.3c).

Eventually the average temperature in Arctic region reaches historical high temperature in November 2016 by the convergence of warm air to the Arctic, which is 140 % higher than global average (Fig. 4.1b). While the sea ice concentration anomaly is almost zero around central Arctic and Canadian Archipelago, the negative anomaly of sea ice concentration still exists in Kara, Barents, and East Siberia Sea (Fig. 4.2d). The preconditioned sea ice by southerly warm winds in August to October contributes considerable negative sea ice anomaly around Kara, Barents, and East Siberia Sea, which attributes sea ice minimum extent in November 2016 (Fig. 4.1c, 4.2d and h). Additionally, warm anomaly in North America is further moved to the Arctic due to southerly winds (Fig. 4.3d).

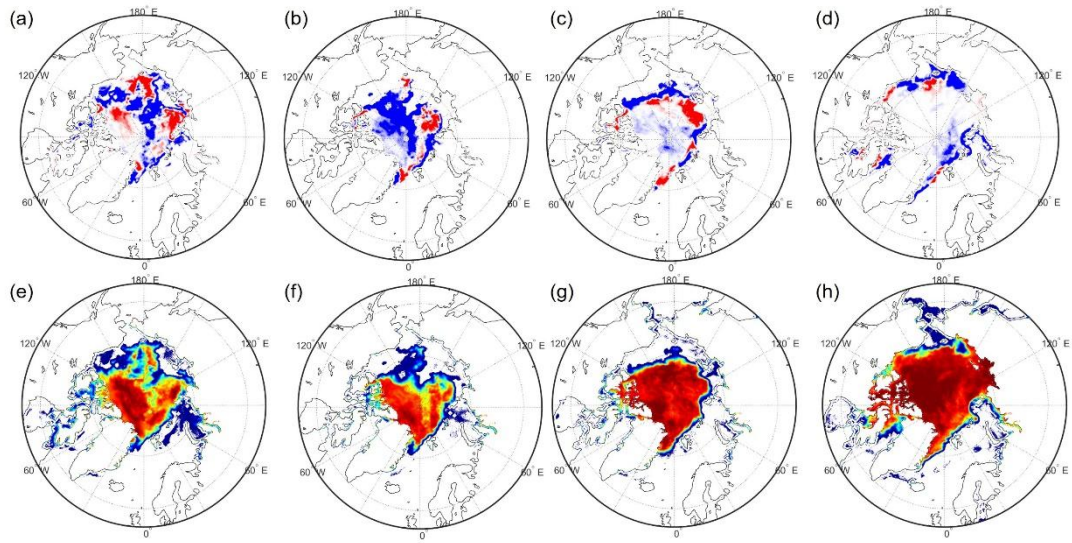


Figure 4. 2 (a-d) sea ice concentration anomaly in August to November from 2007 to 2016. (e-h) sea ice concentration in August to November 2016.

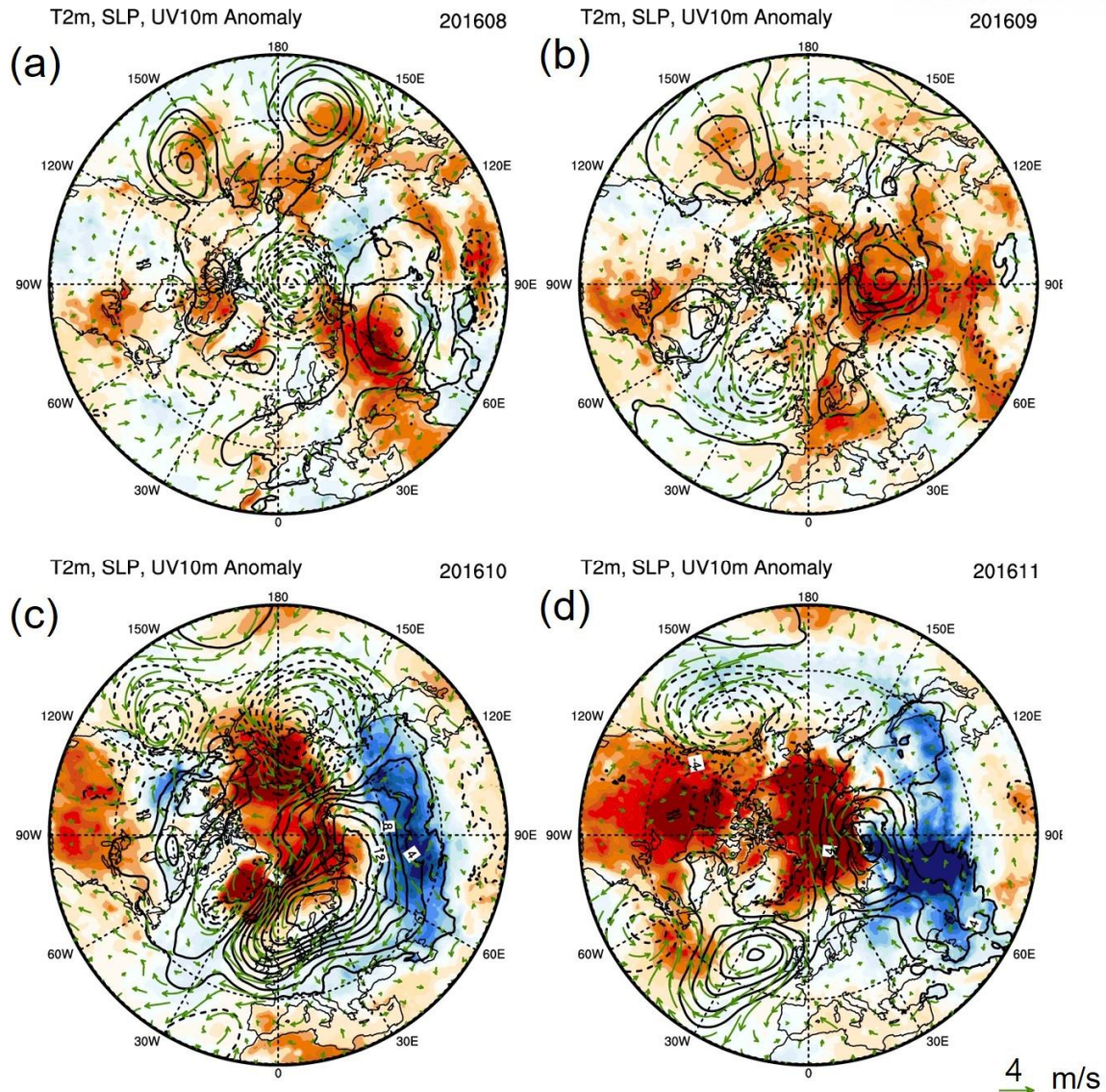


Figure 4. 3 (a-d) spatial distribution of 2-m air temperature, sea level pressure and 10-m wind anomaly in August to November from 1982 to 2016.

SST also might influence on unusual Arctic warming and the minimum sea ice extent in November 2016. Fig. 4.4 shows that strong positive anomalies are observed in Pacific and Atlantic sector. The temporal variability of SST in Pacific is higher than that of in Atlantic (Fig. 4.5). The SST anomaly in August and September 2016 shows comparable high temperature to SST in 2007 and 2012 (Fig. 4.5). However, the SST anomaly in November shows the highest temperature from 1982 in the both of Pacific and Atlantic region. This is the possible factor for negative sea ice anomaly in Kara, Barents, and East Siberia Sea. The historical sea ice extent minimum in November 2016 is possibly the results of couplet of high air temperature and SST.

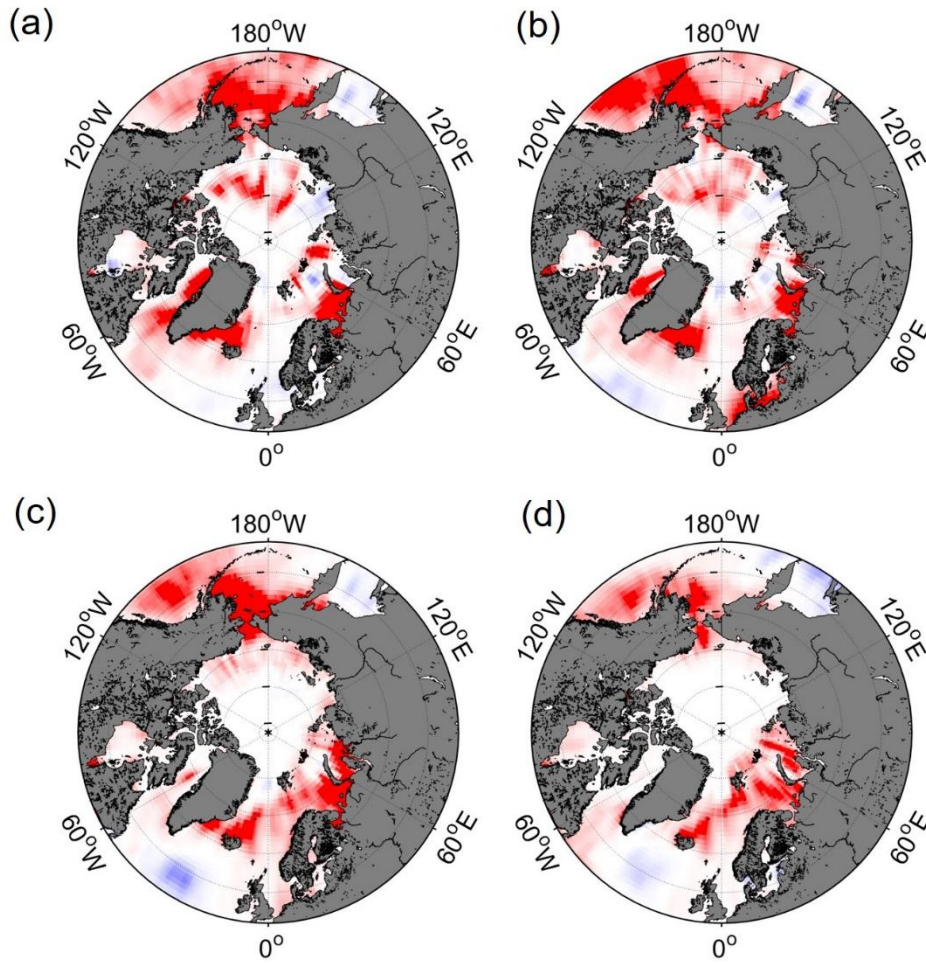


Figure 4. 4 Spatial distribution of SST anomaly (a) August, (b) September, (c) October, and (d) November 2016.

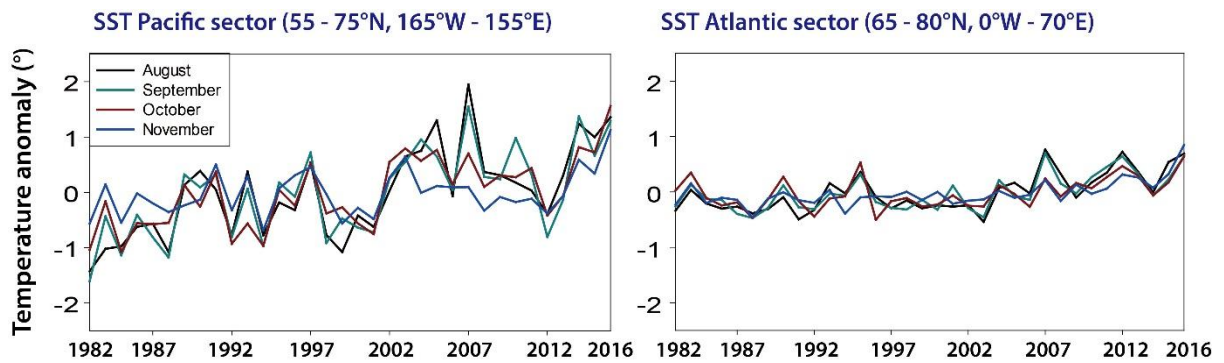


Figure 4. 5 SST anomaly in different sector in August to November 1982 – 2016.

4.4 Discussion

4.4.1 Comparison of previous anomaly phenomena

Arctic sea ice anomaly phenomena have been intensified since 2002, strengthening ice albedo feedback. The weakened sea ice could not easily restore previous state and the ice albedo feedback continues. Key factors behind the minimum record of sea ice extent in November 2016 are complicated rather than one factor. Implying influences on sea ice anomaly in November 2016 could be possible based on previous analysis from literatures. High SST and open water fraction in August and September is likely the cause of bottom melting, which was a major reason for the sea ice anomaly in September 2007 (Perovich et al., 2008; Stroeve et al., 2008). The continuous high SST in August to September 2016 probably contributes the bottom melting, explaining considerable the negative anomaly of sea ice around central Arctic in September 2016, which implies precondition for sea ice extent in November 2016.

It is not easy to conclude whether the frequency and magnitude of winter storm is increasing (Sorteberg and Walsh 2008; Simmonds et al., 2008; Bengtsson et al., 2006). The summer and winter storms in Arctic apparently have affected to the significant loss of sea ice (Zhang et al., 2013; Parkinson et al., 2013; Boisvert et al., 2016). A storm in August to October transverses the Arctic Ocean, taking heat and moisture from sub-Arctic, where is unusual warm to the Arctic. In this process, sea ice was probably sheared off, facilitating sea ice the exposure to water, which contributes precondition of sea ice for anomaly in November 2016.

The resilience of sea ice is continuously decreased by the precondition of sea ice and atmospheric and oceanic phenomena. The sea ice could easily be broken with even smaller Arctic storms before.

4.4.2 Sea ice thickness in November 2016

The region where the anomaly of sea ice concentration anomaly is almost zero explored with sea ice thickness anomaly for a base period of 2011 to 2016 (Fig. 4.6a and b). Although a base period for the sea ice thickness anomaly seems short and different from sea ice concentration, the spatial variation in the central Arctic can be identified. In the area where anomaly is almost zero, a negative anomaly is observed around Canadian Archipelago but a positive anomaly is observed around Laptev Sea. The sea ice thickness in November 2014 around Laptev Sea was under 1 m, which might be the major cause of the positive anomaly. The northwesterly Sea ice drift also likely contributes the positive anomaly around Laptev Sea, converging sea ice (Fig. 4.6d). A monthly sea ice emissivity in November 2016 derived by SSMIS 50GHz channel provides similar spatial characteristic to sea ice thickness regardless of the spatial distribution of air temperature (Fig. 4.6e).

Since the period of sea ice thickness is shorter than that of sea ice concentration, it is hard to directly compare sea ice thickness anomaly and sea ice concentration anomaly. Nonetheless, sea ice

variation in central Arctic, Canadian Archipelago, and Northwestern Greenland can be identified using sea ice thickness, where sea ice concentration anomaly is almost zero in fall and winter season. This implies the sole use of sea ice concentration for the analysis of sea ice anomaly phenomenon is inefficient. Especially, sea ice volume in November 2016 is not minimum in a based period of 2011 – 2016 even though sea ice extent in November 2016 is historical minimum (Fig. 4.7). It should be noted that volume uncertainty (± 0.4 -1.4) should be considered (Ricker et al., 2017). If satellite based sea ice thickness and volume are properly provided throughout the year, the aspect of sea ice minimum might be little different. The sea ice thickness and volume information with a long period could offer more valuable information of sea ice than sea ice concentration.

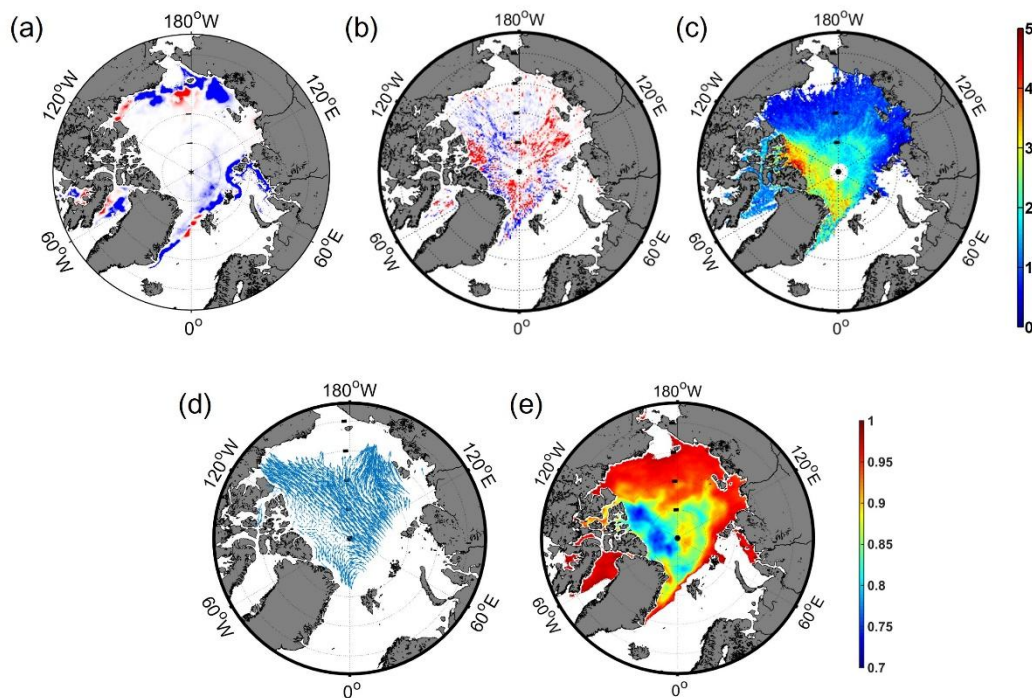


Figure 4. 6 (a) Sea ice concentration anomaly in November 2016 from 2007 and 2016. (b) Sea ice thickness derived by CryoSat-2 anomaly in November from 2011 – 2016. (c) Sea ice thickness in November 2016 derived by CryoSat-2. (d) Sea ice drift in November 2016. (e) Sea ice emissivity in November 2016.

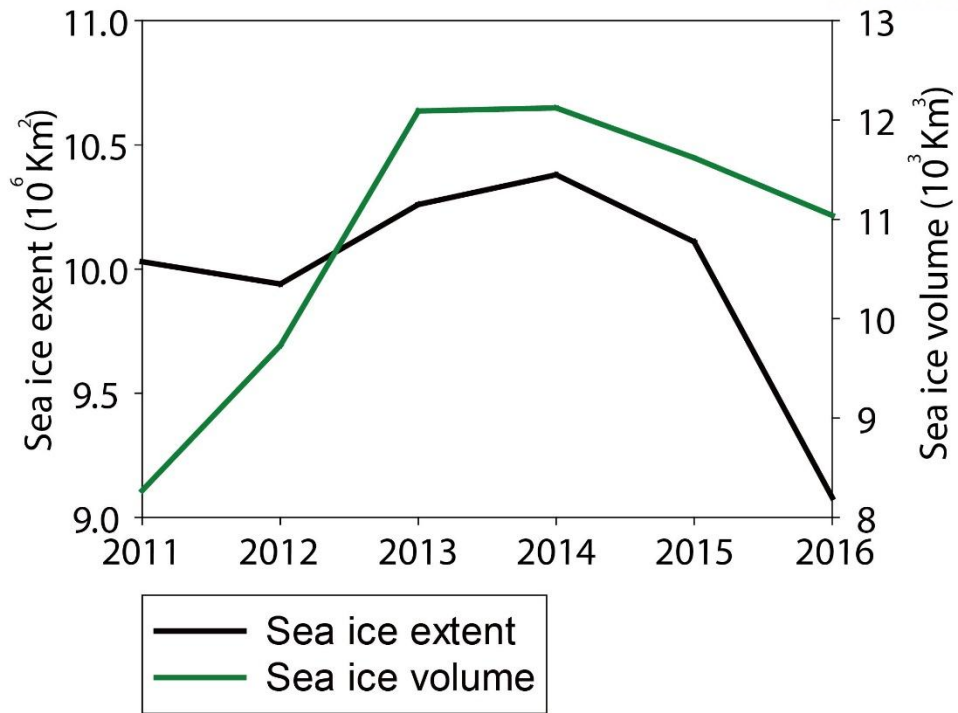


Figure 4. 7 Sea ice extent and volume in November from 2011 to 2016.

4.5 Conclusions

As global warming and Arctic amplification have been intensified, it is not surprise to renew the record of sea ice minimum extent. The significant drop of sea ice extent in November 2016 is occurred compared to previous November. There are four major reasons for sea ice minimum extent in November 2016: 1) preconditioned sea ice, 2) extreme warming in mid-latitudes, 3) warm southerly winds with strong cyclonic storm, and 4) high SST. Various factors influenced on sea ice anomaly in November 2016. An unusual warming event in August and September 2016 is happened in mid-latitudes, which is record breaking warming since 1980. The constant southerly winds by high and low pressure position induce unusual warming in the Arctic, moving warm air from mid-latitudes to the Arctic. A warm ocean also contributes sea ice anomaly phenomenon in the both of Pacific and Atlantic Ocean sector as well, which is almost highest SST ever in November 2016. Furthermore, sea ice volume likely represents sea ice state than sea ice extent.

Average temperature in mid-latitudes and Arctic is expected to rise further in summer. This affects sea ice cover in fall and winter season like the example in November 2016 and sea ice in following spring is also influenced. To understand sea ice condition in spring season, sea ice state in fall and winter needs to be further studied. The sea ice cover is apparently influenced by winds, surface air temperature, currents, and SST and they have a lag time relationship. Thus, the deep understanding of atmospheric and oceanic anomalies in mid-latitudes and Arctic will increase sea ice predictability.

Chapter 5

5. Conclusions

Sea ice thickness is a significant parameter in climate-related process. Climate scientists need accurate sea ice thickness for successful projection of future climate. Unfortunately, sea ice thickness is more difficult parameter to retrieve than other parameters such as sea ice concentration. A large scale sea ice thickness estimation using satellite began in 2003 (Laxon et al., 2003). CryoSat-2 is a current mission for monitoring changes in polar region, which can cover up to 88°N and °S.

The main objective this dissertation is to develop novel CryoSat-2 based lead detection methods using machine learning approaches and waveform mixture algorithm, which might improve accuracy for sea ice thickness as well as to use sea ice thickness and volume for the analysis of sea ice anomaly.

In the retrieval of Arctic sea ice thickness, accurate lead detection is essential to estimate sea ice freeboard and thickness. I applied machine learning approaches, including decision trees and random forest to lead detection, which is superior to previous simple threshold based lead detection methods. This study showed that the over estimation of leads on the ice could induce lower sea ice freeboard. Consequently, sea ice thickness also was more accurate than sea ice thickness derived by previous simple threshold based lead detection methods.

I proposed a new method to detect leads by using waveform mixture algorithm. The endmember is crucial to implement linear mixture algorithm and CryoSat-2 L1b waveforms were considered as endmembers extracted by N-FINDR algorithm. Compare to threshold based lead detection methods, waveform mixture analysis produced better results and comparable machine learning based lead detection. Monthly lead fraction maps derived by waveform mixture algorithm showed strong inter annual variability of recent lead fraction from 2011 to 2016. Additionally, unlike traditional lead detection methods using beam behavior parameters and backscatter sigma-0, the waveform mixture algorithm is less influenced by updating CryoSat-2 data.

The minimum of sea ice extent in November 2016 was happened compared to previous November from 1978. Four possible reasons to affect sea ice anomaly in November 2016 are considered: 1) preconditioned sea ice, 2) extreme warming in mid-latitudes, 3) warming southerly winds with strong cyclonic storm, and 4) high SST. However, unlike sea ice extent in November 2016, sea ice volume derived by thickness in November 2016 is unlikely minimum from 2011.

I tried to improve lead detection methods to increase the application of sea ice thickness data. The sea ice thickness was used to analyze sea ice anomaly in November 2016, which showed a new perspective for sea ice minimum. However, there are still uncertainties factors that prevents accurate retrieval of sea ice thickness and volume, especially, snow depth at a basin scale and densities.

Chapter 6

6. Outlook and Future works

It is found that sea ice cover is decreasing by satellite observation since late 1970 as well as its variability is becoming strong and unpredictable. Climate model simulation predicts ice-free ocean in the Arctic Ocean by the end of the 21 century (Boe et al., 2009). Furthermore, several model studies showed that the observation of the sea ice decline are faster than model simulation results (Stroeve et al., 2007; Wang and Overland, 2012). In this context, satellite observations with a high spatiotemporal resolution are essentially needed to observe polar region. Various studies have been conducted and more development is expected in the future.

Advanced modeling techniques such as machine learning have not been widely used with a satellite altimetry in a polar remote sensing society. I tried to use machine learning techniques to improve lead detection methods, which produce sea ice thickness with higher accuracy than previous threshold based lead detection methods. Additionally, linear mixture analysis that is generally used in the hyper-spectral image analysis was applied for lead detection using waveforms from CryoSat-2 L1b data. These methods produced better results than previous results and overcome the limitation of existing methods. I expect that various polar related parameters will be retrieved through the fusion between machine learning approaches that is a promising tool and satellite altimetry and passive microwave satellite for monitoring of polar region. It can be useful to analyze long-term trend and anomaly of sea ice using retrieved parameters. The use of extended CryoSat-2 mission to 2020 and ICESat-2 data will be launched in 2018 will be actively used for better understanding polar region.

For the future works, daily sea ice thickness will be considered by the use of combination of channels and Polarization Ratio (PR) and Gradient Ratio (GR) from Passive microwave satellites such as AMSR-E and 2. This study will allow the daily variability of sea ice thickness to be explored. The relationship between the change in sea ice thickness and surface heat flux in the Arctic has not much been studied yet. The impact of change in sea ice thickness on surface heat flux will be investigated, which could affect climate in Arctic and Northern hemisphere mid-latitudes.

7. References

- Alexandrov, V., Sandven, S., Wahlin, J., & Johannessen, O. M. (2010). The relation between sea ice thickness and freeboard in the Arctic. *The Cryosphere*, 4(3), 373-380. doi:10.5194/tc-4-373-2010
- Andersen, S., Tonboe, R., Kaleschke, L., Heygster, G., & Pedersen, L. T. (2007). Intercomparison of passive microwave sea ice concentration retrievals over the high-concentration Arctic sea ice. *Journal of Geophysical Research: Oceans*, 112(C8), n/a-n/a. doi:10.1029/2006JC003543
- Armitage, T. W. K., & Davidson, M. W. J. (2014). Using the Interferometric Capabilities of the ESA CryoSat-2 Mission to Improve the Accuracy of Sea Ice Freeboard Retrievals. *Geoscience and Remote Sensing, IEEE Transactions on*, 52(1), 529-536. doi:10.1109/TGRS.2013.2242082
- Barry, R. G., Serreze, M. C., Maslanik, J. A., & Preller, R. H. (1993). The Arctic Sea Ice-Climate System: Observations and modeling. *Reviews of Geophysics*, 31(4), 397-422. doi:10.1029/93RG01998
- Beaven, S. G., Lockhart, G. L., Gogineni, S. P., Hossetnmostafa, A. R., Jezek, K., Gow, A. J., . . . Tjuatja, S. (1995). Laboratory measurements of radar backscatter from bare and snow-covered saline ice sheets. *International Journal of Remote Sensing*, 16(5), 851-876. doi:10.1080/01431169508954448
- Bengtsson, L., Hodges, K. I., & Roeckner, E. (2006). Storm Tracks and Climate Change. *Journal of Climate*, 19(15), 3518-3543. doi:10.1175/jcli3815.1
- Blunden, J., Arndt, D. S., Sánchez-Lugo, A., Scambos, T. A., Schreck III, C. J., Stammerjohn, S., ... & Hurst, D. F. (2017). State of the Climate in 2016. *Bull. Amer. Meteor. Soc*, 98(8), S93-S128.
- Boe, J., Hall, A., & Qu, X. (2009). September sea-ice cover in the Arctic Ocean projected to vanish by 2100. *Nature Geosci*, 2(5), 341-343.
- Boisvert, L. N., Petty, A. A., & Stroeve, J. C. (2016). The Impact of the Extreme Winter 2015/16 Arctic Cyclone on the Barents–Kara Seas. *Monthly Weather Review*, 144(11), 4279-4287. doi:10.1175/mwr-d-16-0234.1
- Bröhan, D., & Kaleschke, L. (2014). A Nine-Year Climatology of Arctic Sea Ice Lead Orientation and Frequency from AMSR-E. *Remote Sensing*, 6(2), 1451.
- Brown, G. S. (1977). The average impulse response of a rough surface and its applications. *Antennas and Propagation, IEEE Transactions on*, 25(1), 67-74. doi:10.1109/TAP.1977.1141536
- Cavalieri, D. J., Cowan, A., Gloersen, P., Grenfell, T., Josberger, E. G., Knight, R. J., . . . Wilheit, T. T. (1983). MIZEX West: Bering Sea Marginal Ice Zone Experiment. *Eos, Transactions American Geophysical Union*, 64(40), 578-579. doi:10.1029/EO064i040p00578
- Cavalieri, D. J., Parkinson, C. L., & Vinnikov, K. Y. (2003). 30-Year satellite record reveals contrasting Arctic and Antarctic decadal sea ice variability. *Geophysical Research Letters*, 30(18), n/a-n/a. doi:10.1029/2003GL018031

- Chase, J. R., & Holyer, R. J. (1990). Estimation of sea ice type and concentration by linear unmixing of Geosat altimeter waveforms. *Journal of Geophysical Research: Oceans*, 95(C10), 18015-18025. doi:10.1029/JC095iC10p18015
- Chi, J., Kim, H.-C., & Kang, S.-H. (2016). Machine learning-based temporal mixture analysis of hypertemporal Antarctic sea ice data. *Remote Sensing Letters*, 7(2), 190-199. doi:10.1080/2150704X.2015.1121300
- Chouzenoux, E., Legendre, M., Moussaoui, S., & Idier, J. (2014). Fast Constrained Least Squares Spectral Unmixing Using Primal-Dual Interior-Point Optimization. *IEEE Journal of Selected Topics in Applied Earth Observations and Remote Sensing*, 7(1), 59-69. doi:10.1109/JSTARS.2013.2266732
- Comiso, J. C. (2006). Abrupt decline in the Arctic winter sea ice cover. *Geophysical Research Letters*, 33(18), n/a-n/a. doi:10.1029/2006GL027341
- Comiso, J. C., Parkinson, C. L., Gersten, R., & Stock, L. (2008). Accelerated decline in the Arctic sea ice cover. *Geophysical Research Letters*, 35(1), n/a-n/a. doi:10.1029/2007GL031972
- Connor, L. N., Farrell, S. L., McAdoo, D. C., Krabill, W. B., & Manizade, S. (2013). Validating ICESat Over Thick Sea Ice in the Northern Canada Basin. *Geoscience and Remote Sensing, IEEE Transactions on*, 51(4), 2188-2200. doi:10.1109/TGRS.2012.2211603
- Cullather, R. I., Lim, Y.-K., Boisvert, L. N., Brucker, L., Lee, J. N., & Nowicki, S. M. J. (2016). Analysis of the warmest Arctic winter, 2015–2016. *Geophysical Research Letters*, 43(20), 10,808-810,816. doi:10.1002/2016GL071228
- Curry, J. A., Schramm, J. L., & Ebert, E. E. (1995). Sea Ice-Albedo Climate Feedback Mechanism. *Journal of Climate*, 8(2), 240-247. doi:10.1175/1520-0442(1995)008<0240:siacfm>2.0.co;2
- Döscher, R., Vihma, T., & Maksimovich, E. (2014). Recent advances in understanding the Arctic climate system state and change from a sea ice perspective: a review. *Atmos. Chem. Phys.*, 14(24), 13571-13600. doi:10.5194/acp-14-13571-2014
- Davis, C. H. (1997). A robust threshold retracking algorithm for measuring ice-sheet surface elevation change from satellite radar altimeters. *Geoscience and Remote Sensing, IEEE Transactions on*, 35(4), 974-979. doi:10.1109/36.602540
- Eicken, H., Tucker, W. B., & Perovich, D. K. (2001). Indirect measurements of the mass balance of summer Arctic sea ice with an electromagnetic induction technique. *Annals of Glaciology*, 33(1), 194-200. doi:10.3189/172756401781818356
- Ertürk, A., & Plaza, A. (2015). Informative Change Detection by Unmixing for Hyperspectral Images. *IEEE Geoscience and Remote Sensing Letters*, 12(6), 1252-1256. doi:10.1109/LGRS.2015.2390973
- Farrell, S. L., Laxon, S. W., McAdoo, D. C., Yi, D., & Zwally, H. J. (2009). Five years of Arctic sea ice freeboard measurements from the Ice, Cloud and land Elevation Satellite. *Journal of*

Geophysical Research: Oceans, 114(C4), C04008. doi:10.1029/2008JC005074

- Flanner, M. G., Shell, K. M., Barlage, M., Perovich, D. K., & Tschudi, M. A. (2011). Radiative forcing and albedo feedback from the Northern Hemisphere cryosphere between 1979 and 2008. *Nature Geosci*, 4(3), 151-155. doi:<http://www.nature.com/ngeo/journal/v4/n3/abs/ngeo1062.html#supplementary-information>
- Forsström, S., Gerland, S., & Pedersen, C. A. (2011). Thickness and density of snow-covered sea ice and hydrostatic equilibrium assumption from in situ measurements in Fram Strait, the Barents Sea and the Svalbard coast. *Annals of Glaciology*, 52(57), 261-270.
- Francis, J. A., & Hunter, E. (2006). New insight into the disappearing Arctic sea ice. *Eos, Transactions American Geophysical Union*, 87(46), 509-511. doi:10.1029/2006EO460001
- Gelaro, R., McCarty, W., Suárez, M. J., Todling, R., Molod, A., Takacs, L., . . . Zhao, B. (2017). The Modern-Era Retrospective Analysis for Research and Applications, Version 2 (MERRA-2). *Journal of Climate*, 30(14), 5419-5454. doi:10.1175/jcli-d-16-0758.1
- Graham, R. M., Cohen, L., Petty, A. A., Boisvert, L. N., Rinke, A., Hudson, S. R., . . . Granskog, M. A. (2017). Increasing frequency and duration of Arctic winter warming events. *Geophysical Research Letters*, 44(13), 6974-6983. doi:10.1002/2017GL073395
- Haas, C., Hendricks, S., & Doble, M. (2006). Comparison of the sea-ice thickness distribution in the Lincoln Sea and adjacent Arctic Ocean in 2004 and 2005. *Annals of Glaciology*, 44(1), 247-252. doi:10.3189/172756406781811781
- Haas, C., Hendricks, S., Eicken, H., & Herber, A. (2010). Synoptic airborne thickness surveys reveal state of Arctic sea ice cover. *Geophysical Research Letters*, 37(9), L09501. doi:10.1029/2010GL042652
- Haas, C., Lobach, J., Hendricks, S., Rabenstein, L., & Pfaffling, A. (2009). Helicopter-borne measurements of sea ice thickness, using a small and lightweight, digital EM system. *Journal of Applied Geophysics*, 67(3), 234-241. doi:<http://dx.doi.org/10.1016/j.jappgeo.2008.05.005>
- Hall, D. K., Key, J. R., Casey, K. A., Riggs, G. A., & Cavalieri, D. J. (2004). Sea ice surface temperature product from MODIS. *IEEE Transactions on Geoscience and Remote Sensing*, 42(5), 1076-1087. doi:10.1109/TGRS.2004.825587
- Hallikainen, M. T., & Jolma, P. A. (1992). Comparison of algorithms for retrieval of snow water equivalent from Nimbus-7 SMMR data in Finland. *Geoscience and Remote Sensing, IEEE Transactions on*, 30(1), 124-131. doi:10.1109/36.124222
- Helm, V., Humbert, A., & Miller, H. (2014). Elevation and elevation change of Greenland and Antarctica derived from CryoSat-2. *The Cryosphere*, 8(4), 1539-1559. doi:10.5194/tc-8-1539-2014
- Im, J., & Jensen, J. R. (2005). A change detection model based on neighborhood correlation image

- analysis and decision tree classification. *Remote Sensing of Environment*, 99(3), 326-340.
doi:<http://dx.doi.org/10.1016/j.rse.2005.09.008>
- Im, J., Jensen, J. R., & Hodgson, M. E. (2008). Object-Based Land Cover Classification Using High-Posting-Density LiDAR Data. *GIScience & Remote Sensing*, 45(2), 209-228.
doi:10.2747/1548-1603.45.2.209
- Im, J., Jensen, J. R., & Tullis, J. A. (2008). Object-based change detection using correlation image analysis and image segmentation. *International Journal of Remote Sensing*, 29(2), 399-423.
doi:10.1080/01431160601075582
- Iordache, M. D., Bioucas-Dias, J. M., & Plaza, A. (2011). Sparse Unmixing of Hyperspectral Data. *IEEE Transactions on Geoscience and Remote Sensing*, 49(6), 2014-2039.
doi:10.1109/TGRS.2010.2098413
- Ivanova, N., Johannessen, O. M., Pedersen, L. T., & Tonboe, R. T. (2014). Retrieval of Arctic Sea Ice Parameters by Satellite Passive Microwave Sensors: A Comparison of Eleven Sea Ice Concentration Algorithms. *IEEE Transactions on Geoscience and Remote Sensing*, 52(11), 7233-7246. doi:10.1109/TGRS.2014.2310136
- Janout, M. A., Aksenov, Y., Hölemann, J. A., Rabe, B., Schauer, U., Polyakov, I. V., . . . Timokhov, L. (2015). Kara Sea freshwater transport through Vilkitsky Strait: Variability, forcing, and further pathways toward the western Arctic Ocean from a model and observations. *Journal of Geophysical Research: Oceans*, 120(7), 4925-4944. doi:10.1002/2014JC010635
- Ji, L., Geng, X., Sun, K., Zhao, Y., & Gong, P. (2015). Modified N-FINDR endmember extraction algorithm for remote-sensing imagery. *International Journal of Remote Sensing*, 36(8), 2148-2162. doi:10.1080/01431161.2015.1034895
- Judah, L. C., Jason, C. F., Mathew, A. B., Vladimir, A. A., & Jessica, E. C. (2012). Arctic warming, increasing snow cover and widespread boreal winter cooling. *Environmental Research Letters*, 7(1), 014007.
- Kashiwase, H., Ohshima, K. I., Nihashi, S., & Eicken, H. (2017). Evidence for ice-ocean albedo feedback in the Arctic Ocean shifting to a seasonal ice zone. *Scientific Reports*, 7(1), 8170. doi:10.1038/s41598-017-08467-z
- Keshava, N., & Mustard, J. F. (2002). Spectral unmixing. *IEEE Signal Processing Magazine*, 19(1), 44-57. doi:10.1109/79.974727
- Key, J., Stone, R., Maslanik, J., & Ellefsen, E. (1993). The detectability of sea-ice leads in satellite data as a function of atmospheric conditions and measurement scale. *Annals of Glaciology*, 17(1), 227-232. doi:10.3198/1993AoG17-1-227-232
- Kildegaard Rose, S., Forsberg, R., & Toudal Pedersen, L. *Measurements of sea ice by satellite and airborne altimetry*. DMIDMI.
- Kim, B.-M., Hong, J.-Y., Jun, S.-Y., Zhang, X., Kwon, H., Kim, S.-J., . . . Kim, H.-K. (2017a). Major

cause of unprecedented Arctic warming in January 2016: Critical role of an Atlantic windstorm. *Scientific Reports*, 7, 40051. doi:10.1038/srep40051

<https://www.nature.com/articles/srep40051#supplementary-information>

Kim, B.-M., Hong, J.-Y., Jun, S.-Y., Zhang, X., Kwon, H., Kim, S.-J., . . . Kim, H.-K. (2017b). Major cause of unprecedented Arctic warming in January 2016: Critical role of an Atlantic windstorm. 7, 40051. doi:10.1038/srep40051

<https://www.nature.com/articles/srep40051#supplementary-information>

Kim, Y. H., Im, J., Ha, H. K., Choi, J.-K., & Ha, S. (2014). Machine learning approaches to coastal water quality monitoring using GOCI satellite data. *GIScience & Remote Sensing*, 51(2), 158-174. doi:10.1080/15481603.2014.900983

Kurtz, N. T., & Farrell, S. L. (2011). Large-scale surveys of snow depth on Arctic sea ice from Operation IceBridge. *Geophysical Research Letters*, 38(20), L20505. doi:10.1029/2011GL049216

Kurtz, N. T., Galin, N., & Studinger, M. (2014). An improved CryoSat-2 sea ice freeboard retrieval algorithm through the use of waveform fitting. *The Cryosphere*, 8(4), 1217-1237. doi:10.5194/tc-8-1217-2014

Kwok, R. (2014). Simulated effects of a snow layer on retrieval of CryoSat-2 sea ice freeboard. *Geophysical Research Letters*, 41(14), 5014-5020. doi:10.1002/2014GL060993

Kwok, R. (2015). Sea ice convergence along the Arctic coasts of Greenland and the Canadian Arctic Archipelago: Variability and extremes (1992–2014). *Geophysical Research Letters*, 42(18), 7598-7605. doi:10.1002/2015GL065462

Kwok, R., & Cunningham, G. F. (2008). ICESat over Arctic sea ice: Estimation of snow depth and ice thickness. *Journal of Geophysical Research: Oceans*, 113(C8), C08010. doi:10.1029/2008JC004753

Kwok, R., Cunningham, G. F., Zwally, H. J., & Yi, D. (2007). Ice, Cloud, and land Elevation Satellite (ICESat) over Arctic sea ice: Retrieval of freeboard. *Journal of Geophysical Research: Oceans*, 112(C12), C12013. doi:10.1029/2006JC003978

Kwok, R., Spreen, G., & Pang, S. (2013). Arctic sea ice circulation and drift speed: Decadal trends and ocean currents. *Journal of Geophysical Research: Oceans*, 118(5), 2408-2425. doi:10.1002/jgrc.20191

Lüpkes, C., Vihma, T., Birnbaum, G., & Wacker, U. (2008). Influence of leads in sea ice on the temperature of the atmospheric boundary layer during polar night. *Geophysical Research Letters*, 35(3), n/a-n/a. doi:10.1029/2007GL032461

Laine, V. (2004). Arctic sea ice regional albedo variability and trends, 1982–1998. *Journal of Geophysical Research: Oceans*, 109(C6), C06027. doi:10.1029/2003JC001818

- Laxon, S., Peacock, N., & Smith, D. (2003). High interannual variability of sea ice thickness in the Arctic region. *Nature*, 425(6961), 947-950.
- Laxon, S. W., Giles, K. A., Ridout, A. L., Wingham, D. J., Willatt, R., Cullen, R., . . . Davidson, M. (2013). CryoSat-2 estimates of Arctic sea ice thickness and volume. *Geophysical Research Letters*, 40(4), 732-737. doi:10.1002/grl.50193
- Lee, S., Im, J., Kim, J., Kim, M., Shin, M., Kim, H.-c., & Quackenbush, L. (2016). Arctic Sea Ice Thickness Estimation from CryoSat-2 Satellite Data Using Machine Learning-Based Lead Detection. *Remote Sensing*, 8(9), 698.
- Lee, S., Kim, H. C., & Im, J. (2017). Arctic lead detection using a waveform mixture algorithm from CryoSat-2 data. *The Cryosphere Discussion*.
- Li, M., Im, J., & Beier, C. (2013). Machine learning approaches for forest classification and change analysis using multi-temporal Landsat TM images over Huntington Wildlife Forest. *GIScience & Remote Sensing*, 50(4), 361-384. doi:10.1080/15481603.2013.819161
- Lindsay, R., Wensnahan, M., Schweiger, A., & Zhang, J. (2014). Evaluation of Seven Different Atmospheric Reanalysis Products in the Arctic. *Journal of Climate*, 27(7), 2588-2606. doi:10.1175/jcli-d-13-00014.1
- Lindsay, R. W. (2001). Arctic sea-ice albedo derived from RGPS-based ice-thickness estimates. *Annals of Glaciology*, 33(1), 225-229. doi:10.3189/172756401781818103
- Lindsay, R. W., & Rothrock, D. A. (1994). Arctic Sea Ice Albedo from AVHRR. *Journal of Climate*, 7(11), 1737-1749. doi:10.1175/1520-0442(1994)007<1737:asiafa>2.0.co;2
- Lindsay, R. W., & Rothrock, D. A. (1995). Arctic sea ice leads from advanced very high resolution radiometer images. *Journal of Geophysical Research: Oceans*, 100(C3), 4533-4544. doi:10.1029/94JC02393
- Long, J. A., Lawrence, R. L., Greenwood, M. C., Marshall, L., & Miller, P. R. (2013). Object-oriented crop classification using multitemporal ETM+ SLC-off imagery and random forest. *GIScience & Remote Sensing*, 50(4), 418-436. doi:10.1080/15481603.2013.817150
- Lu, Z., Im, J., Rhee, J., & Hodgson, M. (2014). Building type classification using spatial and landscape attributes derived from LiDAR remote sensing data. *Landscape and Urban Planning*, 130(0), 134-148. doi:<http://dx.doi.org/10.1016/j.landurbplan.2014.07.005>
- Manabe, S., & Wetherald, R. T. (1975). The Effects of Doubling the CO₂ Concentration on the climate of a General Circulation Model. *Journal of the Atmospheric Sciences*, 32(1), 3-15. doi:10.1175/1520-0469(1975)032<0003:teodtc>2.0.co;2
- Marcq, S., & Weiss, J. (2012). Influence of sea ice lead-width distribution on turbulent heat transfer between the ocean and the atmosphere. *The Cryosphere*, 6(1), 143-156. doi:10.5194/tc-6-143-2012
- Martin, T. V., Zwally, H. J., Brenner, A. C., & Bindshadler, R. A. (1983). Analysis and retracking of

- continental ice sheet radar altimeter waveforms. *Journal of Geophysical Research: Oceans*, 88(C3), 1608-1616. doi:10.1029/JC088iC03p01608
- Maslanik, J., Stroeve, J., Fowler, C., & Emery, W. (2011). Distribution and trends in Arctic sea ice age through spring 2011. *Geophysical Research Letters*, 38(13), n/a-n/a. doi:10.1029/2011GL047735
- Mauritzen, C., & Häkkinen, S. (1997). Influence of sea ice on the thermohaline circulation in the Arctic-North Atlantic Ocean. *Geophysical Research Letters*, 24(24), 3257-3260. doi:10.1029/97GL03192
- Maxwell, A. E., Strager, M. P., Warner, T. A., Zégre, N. P., & Yuill, C. B. (2014). Comparison of NAIP orthophotography and RapidEye satellite imagery for mapping of mining and mine reclamation. *GIScience & Remote Sensing*, 51(3), 301-320. doi:10.1080/15481603.2014.912874
- Maykut, G. A. (1978). Energy exchange over young sea ice in the central Arctic. *Journal of Geophysical Research: Oceans*, 83(C7), 3646-3658. doi:10.1029/JC083iC07p03646
- Maykut, G. A. (1982). Large-scale heat exchange and ice production in the central Arctic. *Journal of Geophysical Research: Oceans*, 87(C10), 7971-7984. doi:10.1029/JC087iC10p07971
- Maykut, G. A., & Untersteiner, N. (1971). Some results from a time-dependent thermodynamic model of sea ice. *Journal of Geophysical Research*, 76(6), 1550-1575. doi:10.1029/JC076i006p01550
- McPhee, M. G., Proshutinsky, A., Morison, J. H., Steele, M., & Alkire, M. B. (2009). Rapid change in freshwater content of the Arctic Ocean. *Geophysical Research Letters*, 36(10), n/a-n/a. doi:10.1029/2009GL037525
- Meier, W. N., Hovelsrud, G. K., van Oort, B. E. H., Key, J. R., Kovacs, K. M., Michel, C., . . . Reist, J. D. (2014). Arctic sea ice in transformation: A review of recent observed changes and impacts on biology and human activity. *Reviews of Geophysics*, 52(3), 185-217. doi:10.1002/2013RG000431
- Mori, M., Watanabe, M., Shiogama, H., Inoue, J., & Kimoto, M. (2014). Robust Arctic sea-ice influence on the frequent Eurasian cold winters in past decades. *Nature Geoscience*, 7, 869. doi:10.1038/ngeo2277
- <https://www.nature.com/articles/ngeo2277#supplementary-information>
- Nicolaus, M., Katlein, C., Maslanik, J., & Hendricks, S. (2012). Changes in Arctic sea ice result in increasing light transmittance and absorption. *Geophysical Research Letters*, 39(24), n/a-n/a. doi:10.1029/2012GL053738
- Onana, V., Kurtz, N. T., Farrell, S. L., Koenig, L. S., Studinger, M., & Harbeck, J. P. (2013). A Sea-Ice Lead Detection Algorithm for Use With High-Resolution Airborne Visible Imagery. *Geoscience and Remote Sensing, IEEE Transactions on*, 51(1), 38-56.

doi:10.1109/TGRS.2012.2202666

- Overland, J. E., Francis, J. A., Hanna, E., & Wang, M. (2012). The recent shift in early summer Arctic atmospheric circulation. *Geophysical Research Letters*, 39(19), n/a-n/a. doi:10.1029/2012GL053268
- Park, H.-S., Lee, S., Son, S.-W., Feldstein, S. B., & Kosaka, Y. (2015). The Impact of Poleward Moisture and Sensible Heat Flux on Arctic Winter Sea Ice Variability. *Journal of Climate*, 28(13), 5030-5040. doi:10.1175/jcli-d-15-0074.1
- Parkinson, C. L., & Cavalieri, D. J. (2008). Arctic sea ice variability and trends, 1979–2006. *Journal of Geophysical Research: Oceans*, 113(C7), C07003. doi:10.1029/2007JC004558
- Parkinson, C. L., & Comiso, J. C. (2013). On the 2012 record low Arctic sea ice cover: Combined impact of preconditioning and an August storm. *Geophysical Research Letters*, 40(7), 1356-1361. doi:10.1002/grl.50349
- Peacock, N. R., & Laxon, S. W. (2004). Sea surface height determination in the Arctic Ocean from ERS altimetry. *Journal of Geophysical Research: Oceans*, 109(C7), C07001. doi:10.1029/2001JC001026
- Perovich, D. K., Grenfell, T. C., Light, B., & Hobbs, P. V. (2002). Seasonal evolution of the albedo of multiyear Arctic sea ice. *Journal of Geophysical Research: Oceans*, 107(C10), SHE 20-21-SHE 20-13. doi:10.1029/2000JC000438
- Perovich, D. K., Jones, K. F., Light, B., Eicken, H., Markus, T., Stroeve, J., & Lindsay, R. (2011). Solar partitioning in a changing Arctic sea-ice cover. *Annals of Glaciology*, 52(57), 192-196. doi:10.3189/172756411795931543
- Polyakov, I., Akasofu, S.-I., Bhatt, U., Colony, R., Ikeda, M., Makshtas, A., . . . Walsh, J. (2002). Trends and variations in Arctic Climate System. *Eos, Transactions American Geophysical Union*, 83(47), 547-548. doi:10.1029/2002EO000379
- Polyakov, I. V., Alekseev, G. V., Bekryaev, R. V., Bhatt, U., Colony, R. L., Johnson, M. A., . . . Yulin, A. V. (2002). Observationally based assessment of polar amplification of global warming. *Geophysical Research Letters*, 29(18), 25-21-25-24. doi:10.1029/2001GL011111
- Pringle, D. J., Eicken, H., Trodahl, H. J., & Backstrom, L. G. E. (2007). Thermal conductivity of landfast Antarctic and Arctic sea ice. *Journal of Geophysical Research: Oceans*, 112(C4), C04017. doi:10.1029/2006JC003641
- Pringle, D. J., Trodahl, H. J., & Haskell, T. G. (2006). Direct measurement of sea ice thermal conductivity: No surface reduction. *Journal of Geophysical Research: Oceans*, 111(C5), C05020. doi:10.1029/2005JC002990
- Qiuhong, T., Xuejun, Z., Xiaohua, Y., & Jennifer, A. F. (2013). Cold winter extremes in northern continents linked to Arctic sea ice loss. *Environmental Research Letters*, 8(1), 014036.
- Röhrs, J., & Kaleschke, L. (2012). An algorithm to detect sea ice leads by using AMSR-E passive

- microwave imagery. *The Cryosphere*, 6(2), 343-352. doi:10.5194/tc-6-343-2012
- Rhee, J., Im, J., Carbone, G. J., & Jensen, J. R. (2008). Delineation of climate regions using in-situ and remotely-sensed data for the Carolinas. *Remote Sensing of Environment*, 112(6), 3099-3111. doi:<http://dx.doi.org/10.1016/j.rse.2008.03.001>
- Rhee, J., Park, S., & Lu, Z. (2014). Relationship between land cover patterns and surface temperature in urban areas. *GIScience & Remote Sensing*, 51(5), 521-536. doi:10.1080/15481603.2014.964455
- Richter-Menge, J. A., Perovich, D. K., Elder, B. C., Claffey, K., Rigor, I., & Ortmeier, M. (2017). Ice mass-balance buoys: a tool for measuring and attributing changes in the thickness of the Arctic sea-ice cover. *Annals of Glaciology*, 44, 205-210. doi:10.3189/172756406781811727
- Ricker, R., Hendricks, S., Girard-Arduin, F., Kaleschke, L., Lique, C., Tian-Kunze, X., . . . Krumpfen, T. (2017a). Satellite-observed drop of Arctic sea ice growth in winter 2015–2016. *Geophysical Research Letters*, n/a-n/a. doi:10.1002/2016GL072244
- Ricker, R., Hendricks, S., Girard-Arduin, F., Kaleschke, L., Lique, C., Tian-Kunze, X., . . . Krumpfen, T. (2017b). Satellite-observed drop of Arctic sea ice growth in winter 2015–2016. *Geophysical Research Letters*, 44(7), 3236-3245. doi:10.1002/2016GL072244
- Ricker, R., Hendricks, S., Helm, V., Skourup, H., & Davidson, M. (2014). Sensitivity of CryoSat-2 Arctic sea-ice freeboard and thickness on radar-waveform interpretation. *The Cryosphere*, 8(4), 1607-1622. doi:10.5194/tc-8-1607-2014
- Rothrock, D. A., Yu, Y., & Maykut, G. A. (1999). Thinning of the Arctic sea-ice cover. *Geophysical Research Letters*, 26(23), 3469-3472. doi:10.1029/1999GL010863
- Screen, J. A., & Simmonds, I. (2010a). The central role of diminishing sea ice in recent Arctic temperature amplification. *Nature*, 464, 1334. doi:10.1038/nature09051
- <https://www.nature.com/articles/nature09051#supplementary-information>
- Screen, J. A., & Simmonds, I. (2010b). The central role of diminishing sea ice in recent Arctic temperature amplification. *Nature*, 464(7293), 1334-1337. doi:http://www.nature.com/nature/journal/v464/n7293/supinfo/nature09051_S1.html
- Serreze, M. C., Barrett, A. P., Stroeve, J. C., Kindig, D. N., & Holland, M. M. (2009). The emergence of surface-based Arctic amplification. *The Cryosphere*, 3(1), 11-19. doi:10.5194/tc-3-11-2009
- Serreze, M. C., & Barry, R. G. (2011). Processes and impacts of Arctic amplification: A research synthesis. *Global and Planetary Change*, 77(1), 85-96. doi:<https://doi.org/10.1016/j.gloplacha.2011.03.004>
- Serreze, M. C., Maslanik, J. A., Scambos, T. A., Fetterer, F., Stroeve, J., Knowles, K., . . . Haran, T. M. (2003). A record minimum arctic sea ice extent and area in 2002. *Geophysical Research Letters*, 30(3), n/a-n/a. doi:10.1029/2002GL016406
- Shokr, M., & Sinha, N. (2015). *Sea ice: physics and remote sensing*. John Wiley & Sons.

- Simmonds, I., Burke, C., & Keay, K. (2008). Arctic Climate Change as Manifest in Cyclone Behavior. *Journal of Climate*, 21(22), 5777-5796. doi:10.1175/2008jcli2366.1
- Sorteberg, A., & Walsh, J. E. (2008). Seasonal cyclone variability at 70°N and its impact on moisture transport into the Arctic. *Tellus A*, 60(3), 570-586. doi:10.1111/j.1600-0870.2008.00314.x
- Spall, M. A. (2007). Circulation and water mass transformation in a model of the Chukchi Sea. *Journal of Geophysical Research: Oceans*, 112(C5), n/a-n/a. doi:10.1029/2005JC003364
- Stroeve, J., Holland, M. M., Meier, W., Scambos, T., & Serreze, M. (2007). Arctic sea ice decline: Faster than forecast. *Geophysical Research Letters*, 34(9), L09501. doi:10.1029/2007GL029703
- Stroeve, J., Serreze, M., Drobot, S., Gearheard, S., Holland, M., Maslanik, J., . . . Scambos, T. (2008). Arctic Sea Ice Extent Plummet in 2007. *Eos, Transactions American Geophysical Union*, 89(2), 13-14. doi:10.1029/2008EO020001
- Taylor, P. C., Cai, M., Hu, A., Meehl, J., Washington, W., & Zhang, G. J. (2013). A Decomposition of Feedback Contributions to Polar Warming Amplification. *Journal of Climate*, 26(18), 7023-7043. doi:10.1175/jcli-d-12-00696.1
- Thirumalai, K., DiNezio, P. N., Okumura, Y., & Deser, C. (2017). Extreme temperatures in Southeast Asia caused by El Niño and worsened by global warming. *Nature Communications*, 8, 15531. doi:10.1038/ncomms15531
- <https://www.nature.com/articles/ncomms15531#supplementary-information>
- Tilling, R. L., Ridout, A., Shepherd, A., & Wingham, D. J. (2015). Increased Arctic sea ice volume after anomalously low melting in 2013. *Nature Geosci*, 8(8), 643-646. doi:10.1038/ngeo2489
- Tonboe, R., Eastwood, S., Lavergne, T., & Pedersen, L. T. (2011). EUMETSAT OSI SAF global sea ice concentration reprocessing data. *Nimbus-7 SMMR and DMSP SSM/I-SSMIS Passive Microwave Data*. National Snow and Ice Data Center, Boulder.
- Toole, J. M., Timmermans, M. L., Perovich, D. K., Krishfield, R. A., Proshutinsky, A., & Richter-Menge, J. A. (2010). Influences of the ocean surface mixed layer and thermohaline stratification on Arctic Sea ice in the central Canada Basin. *Journal of Geophysical Research: Oceans*, 115(C10), n/a-n/a. doi:10.1029/2009JC005660
- Wadhams, P. (1992). Sea ice thickness distribution in the Greenland Sea and Eurasian Basin, May 1987. *Journal of Geophysical Research: Oceans*, 97(C4), 5331-5348. doi:10.1029/91JC03137
- Wadhams, P. (1997). Ice thickness in the Arctic Ocean: The statistical reliability of experimental data. *Journal of Geophysical Research: Oceans*, 102(C13), 27951-27959. doi:10.1029/97JC02503
- Wang, M., & Overland, J. E. (2012). A sea ice free summer Arctic within 30 years: An update from CMIP5 models. *Geophysical Research Letters*, 39(18), L18501. doi:10.1029/2012GL052868
- Warren, S. G., Rigor, I. G., Untersteiner, N., Radionov, V. F., Bryazgin, N. N., Aleksandrov, Y. I., &

- Colony, R. (1999). Snow Depth on Arctic Sea Ice. *Journal of Climate*, 12(6), 1814-1829. doi:10.1175/1520-0442(1999)012<1814:SDOASI>2.0.CO;2
- Weingartner, T., Aagaard, K., Woodgate, R., Danielson, S., Sasaki, Y., & Cavalieri, D. (2005). Circulation on the north central Chukchi Sea shelf. *Deep Sea Research Part II: Topical Studies in Oceanography*, 52(24–26), 3150-3174. doi:<http://doi.org/10.1016/j.dsr2.2005.10.015>
- Wernecke, A., & Kaleschke, L. (2015). Lead detection in Arctic sea ice from CryoSat-2: quality assessment, lead area fraction and width distribution. *The Cryosphere*, 9(5), 1955-1968. doi:10.5194/tc-9-1955-2015
- Willatt, R., Laxon, S., Giles, K., Cullen, R., Haas, C., & Helm, V. (2011). Ku-band radar penetration into snow cover on Arctic sea ice using airborne data. *Annals of Glaciology*, 52(57), 197-205.
- Willmes, S., & Heinemann, G. (2015). Pan-Arctic lead detection from MODIS thermal infrared imagery. *Annals of Glaciology*, 56(69), 29-37. doi:10.3189/2015AoG69A615
- Willmes, S., & Heinemann, G. (2016). Sea-Ice Wintertime Lead Frequencies and Regional Characteristics in the Arctic, 2003–2015. *Remote Sensing*, 8(1), 4.
- Wingham, D., Rapley, C., & Griffiths, H. (1986). *New techniques in satellite altimeter tracking systems*. Paper presented at the ESA Proceedings of the 1986 International Geoscience and Remote Sensing Symposium(IGARSS'86) on Remote Sensing: Today's Solutions for Tomorrow's Information Needs.
- Wingham, D. J., Francis, C. R., Baker, S., Bouzinac, C., Brockley, D., Cullen, R., . . . Wallis, D. W. (2006). CryoSat: A mission to determine the fluctuations in Earth's land and marine ice fields. *Advances in Space Research*, 37(4), 841-871. doi:<http://dx.doi.org/10.1016/j.asr.2005.07.027>
- Winter, M. E. (1999). *N-FINDR: an algorithm for fast autonomous spectral end-member determination in hyperspectral data*.
- Winton, M. (2013). Sea Ice–Albedo Feedback and Nonlinear Arctic Climate Change *Arctic Sea Ice Decline: Observations, Projections, Mechanisms, and Implications* (pp. 111-131): American Geophysical Union.
- Woodgate, R. A., Aagaard, K., & Weingartner, T. J. (2006). Interannual changes in the Bering Strait fluxes of volume, heat and freshwater between 1991 and 2004. *Geophysical Research Letters*, 33(15), n/a-n/a. doi:10.1029/2006GL026931
- Woodgate, R. A., Weingartner, T., & Lindsay, R. (2010). The 2007 Bering Strait oceanic heat flux and anomalous Arctic sea-ice retreat. *Geophysical Research Letters*, 37(1), n/a-n/a. doi:10.1029/2009GL041621
- Yu, Y., Rothrock, D. A., & Lindsay, R. W. (1995). Accuracy of sea ice temperature derived from the advanced very high resolution radiometer. *Journal of Geophysical Research: Oceans*, 100(C3), 4525-4532. doi:10.1029/94JC02244

- Zakharova, E. A., Fleury, S., Guerreiro, K., Willmes, S., Rémy, F., Kouraev, A. V., & Heinemann, G. (2015). Sea Ice Leads Detection Using SARAL/AltiKa Altimeter. *Marine Geodesy*, 38(sup1), 522-533. doi:10.1080/01490419.2015.1019655
- Zhang, J., Lindsay, R., Schweiger, A., & Steele, M. (2013). The impact of an intense summer cyclone on 2012 Arctic sea ice retreat. *Geophysical Research Letters*, 40(4), 720-726. doi:10.1002/grl.50190
- Zhang, J., & Rothrock, D. A. (2003). Modeling Global Sea Ice with a Thickness and Enthalpy Distribution Model in Generalized Curvilinear Coordinates. *Monthly Weather Review*, 131(5), 845-861. doi:10.1175/1520-0493(2003)131<0845:MGSIIWA>2.0.CO;2
- Zortea, M., & Plaza, A. (2009). A Quantitative and Comparative Analysis of Different Implementations of N-FINDR: A Fast Endmember Extraction Algorithm. *IEEE Geoscience and Remote Sensing Letters*, 6(4), 787-791. doi:10.1109/LGRS.2009.2025520
- Zwally, H. J., Yi, D., Kwok, R., & Zhao, Y. (2008). ICESat measurements of sea ice freeboard and estimates of sea ice thickness in the Weddell Sea. *Journal of Geophysical Research: Oceans*, 113(C2), C02S15. doi:10.1029/2007JC004284
- Zygmuntowska, M., Khvorostovsky, K., Helm, V., & Sandven, S. (2013). Waveform classification of airborne synthetic aperture radar altimeter over Arctic sea ice. *The Cryosphere*, 7(4), 1315-1324. doi:10.5194/tc-7-1315-2013
- Zygmuntowska, M., Rampal, P., Ivanova, N., & Smedsrud, L. H. (2014). Uncertainties in Arctic sea ice thickness and volume: new estimates and implications for trends. *The Cryosphere*, 8(2), 705-720. doi:10.5194/tc-8-705-2014

감사의 글 (Acknowledgement)

처음 공부를 시작하기 전에는 5-6 년이면 길다고 생각했지만 하나의 학문 중에서 작은 분야를 익히기에도 턱없이 짧은 시간이었습니다. 아직 배워야 할 것들이 많지만 학위 과정 동안 배운 것을 바탕으로 앞으로 잘해나갈 수 있을 것이라는 확신이 생겼습니다. 그 과정 동안 저를 응원해주고 격려해주신 분들께 감사의 글을 전합니다.

먼저 실력뿐만 아니라 인성도 최고인 저의 지도교수님 임정호 교수님께 감사하다는 말을 전하고 싶습니다. 부족했던 저에게 끊임없는 영감과 용기를 주셨기 때문에 지금까지의 제가 있을 수 있었습니다. 교수님께서 보여주신 연구에 대한 열정, 인생에 대한 철학은 제가 살아가는데 있어 귀감이 됩니다. 따라가기 쉽진 않겠지만 교수님께서 저의 Role model 이십니다! 바쁘신 와중에도 저의 박사 학위 심사위원장을 기꺼이 맡아주신 이명인 교수님 그리고 심사위원인 조경화 교수님 극지연구소 김현철 박사님, 한향선 박사님께도 감사의 말씀을 전합니다. 심사위원분들께서 해주신 말씀들은 앞으로 더 좋은 연구자가 되는데 있어 많은 도움이 될 것 같습니다.

마치 pants 랩장처럼 크게 한 것이 없지만 저희 IRIS 연구실 식구들 잘 해줘서 고마웠고 앞으로 다 잘 될 것이라 믿어 의심치 않습니다. 그리고 말 안 해도 나를 너무 잘 이해해주는 여자친구이자 같은 연구실원인 미애에게도 특별히 고맙다는 말을 하고 싶습니다. 쉽지 않은 대학원생활 중에서 미애와 함께하며 많은 힘과 위로가 되었고 제가 학위를 끝까지 할 수 있었던 숨은 공로자라 생각합니다.

지금은 없는 이명인 교수님에 연구실 김성윤, 미국에서 만나자. 축구의 재미를 알려준 은교, 대현에게도 고맙다는 말을 전합니다. 나의 미친 고등학교 친구들 간디, 대핸느, 슴모, 오리 가끔씩 오래 보자 돌아아들아. 그리고 알무리 힘내라 내가 있다.

언제나 나의 편인 가족들 나의 작은 의견에도 항상 귀를 기울이고 용기의 말을 주시는 어머니, 말은 많이 없지만 마음으로 항상 아버지의 사랑을 느낍니다. 스스로 뭐든

잘하는 3 살 터울 여동생에게 정말 고맙고 사랑한다는 말을 전합니다. 하늘에서
흐뭇해하실 할아버지와 외할머니 그리고 친척분들에게 감사하다는 말씀을 드립니다.

마지막으로 스스로에게 연구도 중요하지만 인생에서 중요하고 가치 있는 것들
놓치며 살지 않기를 바란다.

